



Contents lists available at ScienceDirect

Journal of Quantitative Spectroscopy & Radiative Transfer

journal homepage: www.elsevier.com/locate/jqsrt

Review

Radiative transfer through terrestrial atmosphere and ocean: Software package SCIATRAN



V.V. Rozanov, A.V. Rozanov*, A.A. Kokhanovsky, J.P. Burrows

Institute of Environmental Physics, University of Bremen, Otto Hahn Allee 1, D-28334 Bremen, Germany

ARTICLE INFO

Article history:

Received 18 February 2013

Received in revised form

4 July 2013

Accepted 5 July 2013

Available online 13 July 2013

Keywords:

Radiative transfer

Discrete-ordinates

Thermal emission

Polarization

Ocean–atmosphere coupling

ABSTRACT

SCIATRAN is a comprehensive software package for the modeling of radiative transfer processes in the terrestrial atmosphere and ocean in the spectral range from the ultraviolet to the thermal infrared (0.18–40 μm) including multiple scattering processes, polarization, thermal emission and ocean–atmosphere coupling. The software is capable of modeling spectral and angular distributions of the intensity or the Stokes vector of the transmitted, scattered, reflected, and emitted radiation assuming either a plane-parallel or a spherical atmosphere. Simulations are done either in the scalar or in the vector mode (i. e. accounting for the polarization) for observations by space-, air-, ship- and balloon-borne, ground-based, and underwater instruments in various viewing geometries (nadir, off-nadir, limb, occultation, zenith-sky, off-axis). All significant radiative transfer processes are accounted for. These are, e.g. the Rayleigh scattering, scattering by aerosol and cloud particles, absorption by gaseous components, and bidirectional reflection by an underlying surface including Fresnel reflection from a flat or roughened ocean surface. The software package contains several radiative transfer solvers including finite difference and discrete-ordinate techniques, an extensive database, and a specific module for solving inverse problems. In contrast to many other radiative transfer codes, SCIATRAN incorporates an efficient approach to calculate the so-called Jacobians, i.e. derivatives of the intensity with respect to various atmospheric and surface parameters.

In this paper we discuss numerical methods used in SCIATRAN to solve the scalar and vector radiative transfer equation, describe databases of atmospheric, oceanic, and surface parameters incorporated in SCIATRAN, and demonstrate how to solve some selected radiative transfer problems using the SCIATRAN package. During the last decades, a lot of studies have been published demonstrating that SCIATRAN is a valuable tool for a wide range of remote sensing applications. Here, we present some selected comparisons of SCIATRAN simulations to published benchmark results, independent radiative transfer models, and various measurements from satellite, ground-based, and ship instruments.

Methods for solving inverse problems related to remote sensing of the Earth's atmosphere using the SCIATRAN software are outside the scope of this study and will be discussed in a follow-up paper. The SCIATRAN software package along with a detailed User's Guide is freely available for non-commercial use via the webpage of the Institute of Environmental Physics (IUP), University of Bremen: <http://www.iup.physik.uni-bremen.de/sciattran>.

© 2013 Published by Elsevier Ltd.

* Corresponding author. Tel.: + 49 42121862084.

E-mail address: Alexei.Rozanov@iup.physik.uni-bremen.de (A.V. Rozanov).

Contents

1.	Introduction	15
2.	Features and capabilities of SCIATRAN	16
3.	Development history	17
4.	Basic assumptions and definitions	17
4.1.	Basic boundary value problem	18
4.2.	Boundary value problem for diffuse radiation	19
4.2.1.	Atmosphere	20
4.2.2.	Ocean	20
4.2.3.	Coupled ocean–atmosphere system	21
5.	Solving the vector radiative transfer equation	21
5.1.	Formal solution of VRTE	21
5.2.	Angular discretization of VRTE	22
5.3.	Discrete-ordinates method	23
5.4.	Conservative scattering	23
5.5.	Phase function truncation technique	24
5.6.	Truncation of the Fourier series	25
5.7.	Internal thermal emission	25
5.8.	Pseudo-spherical approximation	27
5.9.	Approximative spherical mode	28
5.10.	Coupled ocean–atmosphere RT model	29
6.	Atmosphere	30
6.1.	Gaseous absorbers, pressure, and temperature	31
6.2.	Rayleigh scattering	31
6.2.1.	Modified Bates approximation	33
6.2.2.	Bucholtz approximation	34
6.2.3.	Bodhaine approximation	35
6.2.4.	User-defined mode	35
6.3.	Atmospheric aerosol	35
6.4.	Clouds	37
6.4.1.	Water cloud database	37
6.4.2.	Ice cloud database	37
6.4.3.	Vertical inhomogeneity of cloud optical characteristics	38
7.	Surface reflection	38
7.1.	Land surface	39
7.2.	Snow surface	40
7.3.	Ocean surface	41
7.3.1.	Fresnel reflection	41
7.3.2.	Water leaving radiation and sea foam	43
8.	Inherent optical properties of natural waters	43
8.1.	Spectral absorption coefficient	43
8.2.	Spectral scattering coefficient	43
9.	Sources of radiation	44
10.	Output radiometric quantities	45
11.	Comparisons to other radiative transfer models: scalar mode	46
11.1.	Plane-parallel atmosphere	46
11.1.1.	Rayleigh scattering	47
11.1.2.	Mie scattering and thermal emission	47
11.2.	Spherical atmosphere	48
11.3.	Ocean overlayed by a black atmosphere	48
11.4.	Coupled ocean–atmosphere system	49
12.	Comparisons to other radiative transfer models: vector mode	49
12.1.	Plane-parallel medium underlain by a Lambertian surface	49
12.2.	Reflection by snow and ocean surfaces	50
12.3.	Spherical atmosphere	51
13.	Selected comparisons with experimental data	52
13.1.	Space-borne measurements of the spectral reflectance over the ocean by MERIS and AATSR instruments	53
13.2.	Space-borne measurements of the spectral reflectance over a land surface by the SCIAMACHY instrument	54
13.3.	Ground-based measurements of the snow reflectance	54
13.4.	Space-borne observations in limb viewing geometry performed by the SCIAMACHY instrument	55
13.5.	Ship-borne measurements of the seawater reflectance	56
13.6.	Underwater in situ measurements	57
14.	Conclusions	58
	Acknowledgments	59
	Appendix A General solution of VRTE	59

A.1. Elementary solutions and separation constants	59
A.2. General solution of the homogeneous equation	61
A.3. Particular solution of the inhomogeneous equation	61
A.4. Analytical expressions for the particular solution coefficients	62
Appendix B Multilayered medium	64
B.1. Bidirectional reflection	65
B.2. Lambertian surface	65
B.3. Black surface	66
References	66

1. Introduction

The integral form of the radiative transfer (RT) equation was formulated for the first time at the end of the 19th century in the independent works of Lommel [1] and Chwolson [2]. During further development of the RT theory, a variety of radiative transfer problems have been solved, in particular, the radiative transfer through stellar ([3,4] and references therein) and planetary [5–9] atmospheres, diffusion of neutrons in nuclear reactors [10,11], and radiative heat transfer [12,13]. In this paper we restrict our consideration to the transfer of solar and thermal radiation through the Earth's atmosphere and ocean as it is handled by the software package SCIATRAN.

An extensive development of approaches for radiative transfer modeling began in the middle of the last century. Since then, various techniques to solve the radiative transfer equation accounting for polarization and multiple scattering processes have been established. The most important methods are listed below:

- The so-called successive order of scattering method [8,14–16] employs the Neumann series solution [17]. This method is implemented, e.g. in the 6S, 6SV1 [18,19], and OS [20] radiative transfer codes.
- The adding-doubling method [21,14,9,8] uses the interaction principle. The method is implemented, e.g. in the PolRadTran [22] and DAK [23] codes.
- The matrix operator method [24,25] is based on the same principle as the adding-doubling method and is implemented, e.g. in the MOMO [26], RTMOM [27], and PSTAR [28] codes.
- The method of spherical harmonics, also known as P_L approximation, [29–31] uses the Fourier series expansion for the intensity. Each Fourier term is expanded then in a series of associated Legendre polynomials. This method is implemented, e.g. in the SHARM code [32,33].
- The discrete-ordinates method [6,34–36] employs first, similar to the spherical harmonic approach, the Fourier series expansion for the intensity. Each Fourier term is discretized then with respect to the polar angle coordinate. The general solution of the resulting linear system of differential equations is found as a combination of homogeneous solutions and a particular solution. This method is implemented, e.g. in the DISORT [34], VDISORT [37,38], COART [39], SBDART [40], LIDORT, VLI-DORT [41], and SCIAPOL [42] codes.
- The finite element method [43] is somewhat similar to the discrete-ordinates method but uses an integration

over a certain range of the polar angle coordinate instead of the discrete representation. This method has been applied to solve radiative transfer problems in the atmosphere and ocean, e.g. by Bulgarelli et al. [44] and Kisselev et al. [45].

- The finite difference method solves a system of linear equations obtained by discretizing the intensity with respect to the geometrical path variable [46]. This method is implemented, e.g. in the GOMETRAN [47] and CDIPI [48] codes.
- The Monte Carlo technique [49,50] is based on the statistical treatment of the radiative transfer processes. Depending on the direction of the photon path tracing one differentiates between the forward (from the Sun to the instrument) and backward (from the instrument to the Sun) Monte Carlo methods. This kind of technique is implemented, e.g. in the MYSTIC [51,52], 3DMCPOL [53], MCC++ [54], and SIRO [55] codes.

A comprehensive description of these and many other methods along with an extensive list of references is provided in a collective book edited by Lenoble [56]. Since then, many numerical codes based on the described methods have been developed. The codes currently used by the remote sensing community are discussed in detail in the literature survey performed in the framework of the ESAS-Light project by Emde et al. [57]. Some of the radiative transfer codes, solvers, and software packages are freely available to users. It should be noted that RT models (e.g. SCIATRAN, SHARM) usually contain databases allowing the user to input physical quantities of interest while the so-called RT solvers (e.g. DISORT) take only optical properties as input. Although not claiming to be complete, an extensive list of radiative transfer models and the information on their availability is presented on the ESAS-Light website [58].

The main objective of the present paper is to comprehensively describe capabilities of the software package SCIATRAN. Primarily designed to solve numerous forward and inverse problems related to the radiative transfer through the terrestrial atmosphere and ocean, SCIATRAN can also be extended to other radiative transfer problems (e.g. atmospheres of other planets) by adding corresponding databases. This study is restricted to the radiative transfer modeling with SCIATRAN while solving inverse problems is a subject of a follow-up publication. The SCIATRAN software package is freely available for non-commercial use via the webpage of the Institute of Environmental Physics (IUP), University of Bremen [59].

We start our discussion in [Section 2](#) with a short overview of the main features of SCIATRAN and a brief comparison of its main capabilities with other up-to-date radiative transfer models. Subsequently, in [Section 3](#), we briefly describe the history of the SCIATRAN development. A general formulation of the radiative transfer problem is presented in [Section 4](#). [Section 5](#) describes solution techniques employed in the SCIATRAN radiative transfer model. The optical characteristics of the atmosphere available in SCIATRAN such as Rayleigh scattering, extinction and scattering by aerosols and clouds as well as gaseous absorption are discussed in [Section 6](#). [Section 7](#) describes reflection properties of underlying surfaces including reflection by the vegetation, snow, and ocean. Inherent optical properties of natural waters needed to perform radiative transfer calculations below the ocean surface are discussed in [Section 8](#). [Section 9](#) discusses the radiation sources, especially the extra-terrestrial solar flux, which can be used as input information for the radiative transfer calculations with SCIATRAN. [Section 10](#) lists all available standard output quantities of the radiative transfer model SCIATRAN. Numerous comparisons of SCIATRAN simulations with acknowledged benchmark results as well as with results from other radiative transfer codes are presented in [Sections 11](#) and [12](#). Comparisons of SCIATRAN simulations to space-borne, ground-based, ship-borne, and underwater measurements are given in [Section 13](#).

2. Features and capabilities of SCIATRAN

In this section we shortly discuss main features of the SCIATRAN radiative transfer model, as presented in [Table 1](#), and compare briefly its main capabilities with other recent radiative transfer models. A detailed discussion of the user interface as well as some technical aspects on the implementation and platform compatibility can be found in the

SCIATRAN User's Guide available at <http://www.iup.physik.uni-bremen.de/sciattran>.

Spectral range: In general, radiative transfer calculations can be performed from 175.44 nm to 40 μm . In the ultra-violet (UV) spectral range, the O_2 Schumann–Runge bands and Herzberg continuum are implemented, which are very important for calculations of photolysis frequencies.

Spectral information: Spectral resolution of absorption cross sections included in the SCIATRAN database ranges from 0.24 to 0.54 nm depending on the spectral range. The ESFT (exponential-sum fitting of transmissions) database is binned as follows: 0.05 nm (394–1070 nm); 0.2 nm (1070–1800 nm); 0.025 nm (1920–2060 nm); 100 nm (> 3500 nm).

Model geometry: SCIATRAN model can be run in a plane-parallel, pseudo-spherical, approximative spherical, and fully spherical modes allowing for a wide range of illumination and observation conditions.

Atmosphere: Databases of optical characteristics of water (spherical droplets) and ice (fractal particles, hexagonal crystals) clouds are provided. Several databases of aerosol optical characteristics including the widely used LOWTRAN 7 parameterization [60] are available.

Surface reflection: Bidirectional reflectance distribution function (BRDF) for a land surface is implemented according to the RPV model [61], the kernel-based linear Ross–Li model [62,63], and its modification [64,65]. For a coupled ocean–atmosphere system, SCIATRAN can be run assuming either an absolutely flat or wind-roughed air–water interface. Although several coupled ocean–atmosphere RT models have recently been developed [66,39,28,67], most of them are publicly unavailable. The COART model [39] can be run online by specifying a set of input parameters via a web interface (<http://www.snowdog.larc.nasa.gov/jin/rtnote.html>) but its source code is unavailable. According to our knowledge, SCIATRAN is presently the only freely available software

Table 1
Main features of the SCIATRAN software package.

Model features	Description	Comments
Spectral range	Ultraviolet, visible, near infrared, thermal infrared	Thermal emission is included
Spectral information	Correlated-k, line-by-line, cross-sections	Boxcar, Gaussian, or user defined shapes of the slit function can be used to convolve simulated spectra
Model geometry	1-D, plane-parallel, pseudo-spherical, approximative spherical, fully spherical	The fully spherical solution is implemented only for the scalar mode
Atmosphere	Absorption by atmospheric trace gases, Rayleigh scattering, aerosols, clouds	The scattering matrix within an ice cloud is independent of the altitude
Surface	Lambertian reflection, BRDF, coupled ocean–atmosphere system	Fresnel reflection, sea foam, water leaving radiance for ocean surface
Jacobians	Derivatives of the intensity with respect to atmospheric and surface parameters	Under implementation in the vector mode and for a coupled ocean–atmosphere system
Polarization	Vector radiative transfer is implemented for most of the program modes	Still under development for a coupled ocean–atmosphere system
Refraction	Implemented for both solar beam and line-of-sight	The refractive index of the air is assumed to be independent of the wavelength
Raman scattering	First order approximation (in the frequency domain) for the rotational Raman scattering	Not implemented in the vector mode and for a coupled ocean–atmosphere system
Availability	Freely available for a scientific use, no commercial use is permitted, registration is required	http://www.iup.physik.uni-bremen.de/sciattran

capable of modeling radiative transfer through a coupled ocean–atmosphere system.

Jacobians: In addition to the intensities, SCIATRAN can calculate their derivatives (Jacobians) with respect to various atmospheric and surface parameters within the same code run. Providing a linear relationship between the variation of the intensity and variations of corresponding atmospheric and surface parameters, the Jacobians (also known as weighting functions) are very important for performing sensitivity studies, analyzing error budgets, and solving inverse problems. In the SCIATRAN model weighting functions are calculated employing a very efficient forward–adjoint technique, which is based on the joint solution of the linearized forward and adjoint radiative transfer equations (see [68,69] and references therein). Theoretical aspects of this technique are discussed in detail in [70–72,68]. The forward–adjoint technique has also been employed in GOMETRAN [47] (scalar), Gauss–Seidel [73] (scalar), and LIRA [74] (vector) radiative transfer models. Another approach based on the analytical differentiation of the discrete-ordinates equations has been implemented in the LIDORT (scalar) and VLIDORT (vector) codes [41].

Raman scattering: Rotational Raman scattering is an example of inelastic scattering processes in the Earth's atmosphere. It gives rise to filling-in of solar Fraunhofer lines and absorption signatures of trace gases in measured spectra of scattered solar radiation. At present, there are several RT codes capable of simulating the Raman scattering [75–79]. Recently, the freely available libRadtran radiative transfer package [80] has also been extended by a rotational Raman scattering capability. To our knowledge, the SCIATRAN and libRadtran models are presently the only freely available software codes capable of modeling rotational Raman scattering in a surface–atmosphere system.

Among the existing 1-D radiative transfer models, SCIATRAN offers the most extensive variety of options to solve RT problems related to the Earth's atmosphere and ocean. Extensive database and default modes (e.g. default settings for the Rayleigh and aerosol scattering, as well as for the accuracy control) facilitate the usage of SCIATRAN by less experienced users. On the other hand, the variety of user-defined modes implemented in SCIATRAN offers a high flexibility for experienced users.

3. Development history

The development of a precursor model referred to as GOMETRAN has been initiated in 1994. The first version described by Rozanov et al. [47] used the finite difference method to solve the scalar radiative transfer equation [46]. The model was capable of simulating spectral intensities and fluxes either in a plane-parallel or in a pseudo-spherical approximation. The database contained characteristics of the atmosphere and underlying surface in the spectral range 240–790 nm needed for the interpretation of measurements from the satellite instrument GOME (Global Ozone Monitoring Experiment) [81], which gave its name to the model. Thermal radiation and polarization effects were not considered. Later, the database was extended to 175.44 nm and the model was further

developed to calculate the actinic fluxes. A modified version of the code named PHOTOGT [82] was optimized for solving problems of atmospheric chemistry by adding a capability of computing photolysis frequencies in the stratosphere and troposphere.

The SCIATRAN family of codes launched in 2000 was aimed at the interpretation of measurements from the SCIAMACHY (SCanning Imaging Absorption spectroMeter for Atmospheric CHartography) instrument onboard ENVISAT [83,84]. Compared to previous model versions, the database of SCIATRAN was extended to 2400 nm to cover the entire spectral range of SCIAMACHY (240–2400 nm). The model was capable of operating in both line-by-line and correlated-k distribution scheme modes. A detailed description of the first generation of SCIATRAN models (version 1.2) was presented by Rozanov et al. [85].

A successor version of the code (SCIATRAN 2.0) described by Rozanov et al. [86] featured, in addition, an approximative spherical and a fully spherical mode [48]. This enabled the computation of radiances and air mass factors for limb and solar/lunar occultation geometries. By using approximate solutions of the radiative transfer equation, fast simulations could be made both inside and outside gaseous absorption bands. SCIATRAN 2.0 was capable of computing weighting functions (Jacobians) of atmospheric parameters by solving a linearized radiative transfer equation. The software featured also a retrieval block which employed either the Optimal Estimation Method [87] or the Information Operator Technique [88,89] for solving inverse problems.

From version 2.2 onwards, the SCIATRAN features a new discrete-ordinates solver intended to replace the obsolete finite difference method. Version 3.0 of SCIATRAN was extended by a capability of solving the vector radiative transfer equation (i.e. including polarization) [42]. The most recent version of the SCIATRAN model (version 3.1), which is discussed in detail below, accounts, in addition, for thermal emission and is capable of modeling the radiative transfer through a coupled ocean–atmosphere system.

4. Basic assumptions and definitions

In this section we describe basic principles of a radiative transfer model aimed at simulating the radiation field in the atmosphere and ocean accounting for the polarization, thermal emission and bidirectional surface reflection. Here, the same restrictions as formulated by Hovenier et al. [9] are imposed:

- independent scattering by molecules and small particles (aerosols and cloud particles in the atmosphere and hydrosols in water);
- scattering without changing the wavelength (elastic scattering) with exception of the rotational Raman scattering in the atmosphere;
- extinction of light is independent of the polarization state of the incident light (e.g. radiative transfer within a cloud containing oriented crystals is not considered);
- the medium is locally plane-parallel;

- the medium is macroscopically isotropic and mirror symmetric, see [9,90] for details;
- top of the medium is illuminated by a monodirectional unpolarized beam of light with an infinite extension in space;
- both medium and light source are assumed to be time-independent, and any nonlinear effects are neglected;
- thermal emission is the only internal source of the energy in the medium;
- the medium is in a local thermodynamic equilibrium.

Some additional assumptions needed to solve the radiative transfer equation (RTE) for various observation geometries (e.g. to account for the sphericity of the atmosphere) or to obtain the solution for a coupled ocean–atmosphere system will be formulated below.

The diffuse radiation emerging from the atmosphere, in particular its intensity and polarization state, can be fully characterized by four Stokes parameters. For a plane electromagnetic wave, the Stokes parameters are defined with respect to a reference plane. The latter is usually selected to contain the propagation direction of the wave. When considering multiple scattering processes in the atmosphere, it is convenient to select the meridional plane as the reference. This plane is drawn through the propagation direction of the wave and the z -axis of a local right-handed Cartesian coordinate system. The coordinate system and the reference plane (grey) are shown in Fig. 1.

In the far-field zone, i.e. in the zone where an object can be treated as a point source of the scattered radiation, the electric field vector is orthogonal to the propagation direction of the wave. Thus, at the observation point, it can be represented following Mishchenko et al. [91] as

$$\mathbf{E} = \mathbf{E}_\theta + \mathbf{E}_\varphi, \quad (1)$$

where \mathbf{E}_θ and \mathbf{E}_φ are the parallel and perpendicular components of the electric field vector lying in the plane normal to the reference plane, respectively. Let us introduce unit vectors $\hat{\mathbf{e}}_\theta$ and $\hat{\mathbf{e}}_\varphi$ such that $\mathbf{n} = \hat{\mathbf{e}}_\theta \times \hat{\mathbf{e}}_\varphi$, where \mathbf{n} is the propagation direction of the electromagnetic wave.

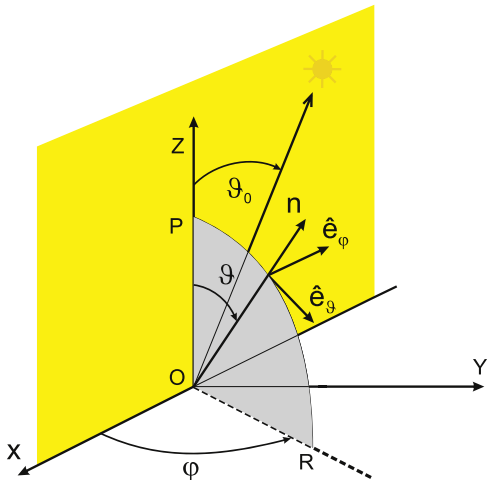


Fig. 1. Basic Cartesian coordinate system. The reference plane is shown in grey.

The latter is defined by the angle pair $\{\theta, \varphi\}$, where the polar (zenith) angle, $\theta \in [0, \pi]$, is measured from the positive z -axis and the azimuthal angle, $\varphi \in [0, 2\pi]$, is measured from the positive x -axis towards the positive y -axis (see Fig. 1). Now, the components of the electric field vector can be written as

$$\mathbf{E}_\theta = E_\theta \hat{\mathbf{e}}_\theta, \quad \mathbf{E}_\varphi = E_\varphi \hat{\mathbf{e}}_\varphi. \quad (2)$$

The components of the Stokes vector, $\mathbf{I} = [I, Q, U, V]^T$ (superscript T denotes the transpose operation), can be defined then as follows (see e.g. [90,91]):

$$\begin{aligned} I &= \overline{E_\theta E_\theta^*} + \overline{E_\varphi E_\varphi^*}, \\ Q &= \overline{E_\theta E_\theta^*} - \overline{E_\varphi E_\varphi^*}, \\ U &= -[\overline{E_\theta E_\varphi^*} + \overline{E_\varphi E_\theta^*}] = -2 \operatorname{Re}[\overline{E_\theta E_\varphi^*}], \\ V &= i[\overline{E_\theta E_\varphi^*} - \overline{E_\varphi E_\theta^*}] = 2 \operatorname{Im}[\overline{E_\theta E_\varphi^*}]. \end{aligned} \quad (3)$$

Here, the asterisk denotes the complex conjugation, the bar represents an average over a large number of electric vector oscillations, and the normalization factor is neglected.

The definition of the Stokes vector according to Eq. (3) is implemented in the SCIATRAN model and will be further used in the course of this paper. Our comparisons show that this definition coincides with the one used by Hovenier et al. [9] if the unit vectors perpendicular and parallel to the reference plane (\mathbf{r} and \mathbf{l} , respectively) are selected as

$$\mathbf{r} = -\hat{\mathbf{e}}_\varphi, \quad \mathbf{l} = \hat{\mathbf{e}}_\theta. \quad (4)$$

There are also other definitions presented among others by Chandrasekhar [6], van de Hulst [92,8], Hansen and Travis [14], Hovenier and Van der Mee [93], and Lenoble [94]. A detailed discussion of different representations for the Stokes vector and their relation is, however, outside the scope of this study.

4.1. Basic boundary value problem

The vector radiative transfer equation (VRTE) for the total Stokes vector (sum of the direct and diffuse parts) in a scattering, absorbing, and emitting plane-parallel medium can be derived by applying the energy conservation law to an elementary volume. Under assumptions discussed at the beginning of Section 4, this results in

$$\mu \frac{\partial}{\partial \tau} \mathbf{I}_{\text{tot}}(\tau, \Omega) = -\mathbf{I}_{\text{tot}}(\tau, \Omega) + \mathbf{J}_{\text{tot}}(\tau, \Omega) + \mathbf{J}_e(\tau, \Omega). \quad (5)$$

Details on how to derive this equation can be found among others in [6,9,95]. In Eq. (5), $\mathbf{J}_{\text{tot}}(\tau, \Omega)$ and $\mathbf{J}_e(\tau, \Omega)$ denote the scattering and internal emission source functions, respectively, $\tau \in [0, \tau_0]$ is the optical depth changing from $\tau = 0$ at the top to $\tau = \tau_0$ at the bottom of the medium, and the variable $\Omega = \{\mu, \varphi\}$ represents a pair of angle variables, $\mu \in [-1, 1]$ and $\varphi \in [0, 2\pi]$. Here, μ is the cosine of the polar angle, θ , measured from the positive z -axis and φ is the azimuthal angle measured from the positive x -axis in the clockwise direction when looking in the direction of the positive z -axis (see Fig. 1). The scattering source function is

given by

$$\mathbf{J}_{\text{tot}}(\tau, \Omega) = \frac{\omega(\tau)}{4\pi} \int_{4\pi} \mathbf{Z}(\tau, \Omega, \Omega') \mathbf{I}_{\text{tot}}(\tau, \Omega') d\Omega', \quad (6)$$

where $\omega(\tau)$ is the single scattering albedo (scattering coefficient divided by the extinction coefficient) and $\mathbf{Z}(\tau, \Omega, \Omega')$ is the phase matrix describing the scattering properties of the medium. In a local thermodynamic equilibrium (one of the requirements formulated above), the internal emission source function $\mathbf{J}_e(\tau, \Omega)$ is represented as

$$\mathbf{J}_e(\tau, \Omega) = [1 - \omega(\tau)] B[T(\tau)] \mathbf{I}_1, \quad (7)$$

where $B[T(\tau)]$ is the Planck function (see e.g. [94,96] for details), $T(\tau)$ is the kinetic temperature of the medium, and the vector $\mathbf{I}_1 = [1, 0, 0, 0]^T$ indicates that the thermal emission is unpolarized.

The phase matrix $\mathbf{Z}(\tau, \Omega, \Omega')$ is closely related to the scattering matrix $\mathbf{F}(\tau, \gamma)$ that describes a transformation of the Stokes vector as a result of scattering by a volume element. For a mirror symmetric and macroscopically isotropic medium (see restrictions above) the scattering matrix can be written as

$$\mathbf{F}(\tau, \gamma) = \begin{bmatrix} F_{11}(\tau, \gamma) & F_{12}(\tau, \gamma) & 0 & 0 \\ F_{12}(\tau, \gamma) & F_{22}(\tau, \gamma) & 0 & 0 \\ 0 & 0 & F_{33}(\tau, \gamma) & F_{34}(\tau, \gamma) \\ 0 & 0 & -F_{34}(\tau, \gamma) & F_{44}(\tau, \gamma) \end{bmatrix}, \quad (8)$$

see [9,93] for further details. Here, γ is the scattering angle, i.e. the angle between the propagation directions of the incident and scattered waves. The element $F_{11}(\tau, \gamma)$ of the scattering matrix is normalized as follows:

$$\frac{1}{2} \int_0^\pi F_{11}(\tau, \gamma) \sin \gamma d\gamma = 1. \quad (9)$$

In the scalar radiative transfer theory, $F_{11}(\tau, \gamma)$ is referred to as the phase function. The term $F_{11}(\tau, \gamma) d\Omega/4\pi$ describes the probability that the light is scattered within a solid angle $d\Omega$ around the direction which has the angle γ with respect to the incident direction. As discussed among others by Mishchenko et al. [90], the scattering matrix can be obtained considering the scattering of electromagnetic waves on a given particle or collection of particles. For spherical particles, the elements of the scattering matrix can be calculated using the Mie theory [97]. In particular, it follows that $F_{11} = F_{22}$ and $F_{33} = F_{44}$.

The scattering matrix $\mathbf{F}(\tau, \gamma)$ relates the incident and scattered wave Stokes vectors that are defined with respect to the scattering plane. The latter is drawn through the propagation directions of the incident and scattering waves. However, as discussed above, the Stokes vector is usually defined with respect to the meridional plane which does not need to coincide with the scattering plane. Therefore, a rotation of the reference plane of both the incident wave before the scattering process and the scattered wave thereafter is needed to apply the scattering matrix. The entire transformation is described by the phase matrix, $\mathbf{Z}(\tau, \Omega, \Omega')$, that, according to Chandrasekhar

[6], is related to the scattering matrix as follows:

$$\mathbf{Z}(\tau, \Omega, \Omega') = \mathbf{L}(\pi - \chi_2) \mathbf{F}(\tau, \gamma) \mathbf{L}(\pi - \chi_1). \quad (10)$$

Here, χ_1 and χ_2 are the rotation angles between the local meridional plane and the scattering plane for the incident and scattered waves, respectively. Following Mishchenko et al. [90] a positive rotation is clockwise when looking in the direction of the wave propagation. Before the scattering event, matrix $\mathbf{L}(\chi)$ rotates the meridional plane of the incident wave by angle $\pi - \chi_1$ to match the local scattering plane (we assume that $0 < \varphi - \varphi' < \pi$). After the scattering event the matrix rotates the local scattering plane by angle $\pi - \chi_2$ to match the meridional plane of the scattered wave.

The boundary conditions for VRTE given by Eq. (5) are formulated as follows. At the top of the atmosphere, the incident solar radiation is assumed to be a monodirectional unpolarized light beam with an infinite extension in space. The solar zenith angle, θ_0 in Fig. 1, is defined as an angle between the positive direction of the z-axis and the direction to the Sun. The x-axis of the basic coordinate system is chosen to point away from the Sun. This means that the azimuthal angle of the solar beam is equal to zero ($\varphi_0 = 0^\circ$). The Stokes vector of the direct solar light is written as $F_0 \delta(\mu - \mu_0) \delta(\varphi - \varphi_0) \mathbf{I}_1$, where $\delta(\mu - \mu_0)$ and $\delta(\varphi - \varphi_0)$ are the Dirac delta functions [98], μ_0 is the cosine of the solar zenith angle, and F_0 is the solar irradiance. Throughout this study we assume F_0 to be equal to π . The upper boundary condition is formulated then as

$$\mathbf{I}_{\text{tot}}(0, \mu, \varphi) = \pi \delta(\mu - \mu_0) \delta(\varphi - \varphi_0) \mathbf{I}_1. \quad (11)$$

At the lower boundary of the considered plane-parallel medium, we assume a bidirectional reflecting surface. The lower boundary condition is written then as follows:

$$\mathbf{I}_{\text{tot}}(\tau_0, \Omega) = \mathcal{R} \mathbf{I}_{\text{tot}}(\tau_0, \Omega') + \epsilon B(T_s) \mathbf{I}_1, \quad \mu < 0, \quad (12)$$

where ϵ is the surface emissivity, $B(T_s)$ is the Planck function at the surface temperature, T_s , and \mathcal{R} is a linear integral operator defined by

$$\mathcal{R} = \frac{1}{\pi} \int_0^{2\pi} d\varphi' \int_0^1 d\mu' \mu' \mathbf{R}(\Omega, \Omega') \otimes. \quad (13)$$

Here, $\mathbf{R}(\Omega, \Omega')$ is a 4×4 matrix determining the angular reflection properties of the boundary surface. The symbol \otimes is used to highlight the fact that \mathcal{R} is an integral operator rather than a finite integral.

The VRTE according to Eq. (5) along with the boundary conditions given by Eqs. (11) and (12) will be further referred to as the standard boundary value problem (BVP).

4.2. Boundary value problem for diffuse radiation

As discussed in the previous section, the boundary value problem for the total Stokes vector contains Dirac δ -functions in the upper boundary condition, see Eq. (11). It is well known that the solution of such a problem contains generalized functions, which are difficult to treat numerically. A common approach to eliminate generalized functions in the solution of BVP is to split the total Stokes vector into the direct, $\mathbf{D}(\tau, \Omega)$, and diffuse, $\mathbf{I}(\tau, \Omega)$, components, see e.g. [6]:

$$\mathbf{I}_{\text{tot}}(\tau, \Omega) = \mathbf{I}(\tau, \Omega) + \mathbf{D}(\tau, \Omega). \quad (14)$$

The boundary value problem is formulated then for the diffuse component only. To this end let us substitute $\mathbf{I}_{\text{tot}}(\tau, \Omega)$ given by Eq. (14) into the VRTE for the total Stokes vector, Eq. (5), and introduce the multiple and the single scattering source functions as follows:

$$\mathbf{J}_m(\tau, \Omega) = \frac{\omega(\tau)}{4\pi} \int_{4\pi} \mathbf{Z}(\tau, \Omega, \Omega') \mathbf{I}(\tau, \Omega') d\Omega', \quad (15)$$

$$\mathbf{J}_s(\tau, \Omega) = \frac{\omega(\tau)}{4\pi} \int_{4\pi} \mathbf{Z}(\tau, \Omega, \Omega') \mathbf{D}(\tau, \Omega') d\Omega'. \quad (16)$$

This results in the following BVP for the diffuse component of the total Stokes vector:

$$\mu \frac{\partial}{\partial \tau} \mathbf{I}(\tau, \Omega) = -\mathbf{I}(\tau, \Omega) + \mathbf{J}_m(\tau, \Omega) + \mathbf{J}_s(\tau, \Omega) + \mathbf{J}_e(\tau, \Omega), \quad (17)$$

$$\mathbf{I}(0, \Omega) = \mathbf{0}, \quad \mu > 0, \quad (18)$$

$$\mathbf{I}(\tau_0, \Omega) = \mathcal{R}\mathbf{D}(\tau_0, \Omega') + \mathcal{R}\mathbf{I}(\tau_0, \Omega') + \epsilon B(T_s) \mathbf{I}_1, \quad \mu < 0, \quad (19)$$

where the integral operator \mathcal{R} is given by Eq. (13).

In the following subsections we discuss how to select appropriate boundary conditions and an expression for the direct component of the total Stokes vector, $\mathbf{D}(\tau, \Omega)$, to model the radiative transfer through an atmosphere, ocean, or a coupled atmosphere-ocean system.

4.2.1. Atmosphere

According to Eqs. (16) and (19), both the single scattering source function and the lower boundary condition of the above discussed BVP contain the direct component of the Stokes vector $\mathbf{D}(\tau, \Omega)$. Thus, an explicit expression for this component needs to be formulated in order to solve the BVP. Most commonly, the radiation reflected from the surface does not contain a specular component, which leads to the following expression for $\mathbf{D}(\tau, \Omega)$:

$$\mathbf{D}_a(\tau, \Omega) = \pi \delta(\mu - \mu_0) \delta(\varphi - \varphi_0) \mathbf{I}_1 e^{-\tau/\mu}. \quad (20)$$

This equation describes the attenuation of the direct solar radiation while it travels from the top of the atmosphere to the optical depth τ . In contrast, the Fresnel reflection of the direct solar light from a flat water surface results in an upward traveling direct solar radiation. Thus, in this case, both downward and upward traveling direct solar radiation is present:

$$\mathbf{D}_{\text{flat}}(\tau, \Omega) = \pi \delta(\mu - \mu_0) \delta(\varphi - \varphi_0) \mathbf{I}_1 e^{-\tau/\mu_0} + \pi \delta(\mu + \mu_0) \delta(\varphi - \varphi_0) \mathbf{R}_F(\mu_0) \mathbf{I}_1 e^{-(2\tau_a - \tau)/\mu_0}. \quad (21)$$

Here, $\mathbf{R}_F(\mu_0)$ is the Fresnel reflection matrix (see below) of the water surface and τ_a is the total optical thickness of the atmosphere. The second term in this equation describes the attenuation by the atmosphere of the direct solar radiation which is reflected by the water surface and travels then from the surface to the optical depth τ . In this case, both terms contain generalized functions. Thus, the single scattering source function and the lower boundary condition are different for a flat and for a rough water surface.

For a *land or wind-roughed water surface*, expressions for the single scattering source function and the lower boundary condition are obtained substituting Eq. (20) into

Eqs. (16) and (19):

$$\mathbf{J}_s(\tau, \Omega) = \frac{\omega(\tau)}{4} \mathbf{Z}(\tau, \Omega, \Omega_0) \mathbf{I}_1 e^{-\tau/\mu_0}, \quad (22)$$

$$\mathbf{I}(\tau_0, \Omega) = \mathbf{R}(\Omega, \Omega_0) \mathbf{I}_1 \mu_0 e^{-\tau_0/\mu_0} + \mathcal{R}\mathbf{I}(\tau_0, \Omega') + \epsilon B(T_s) \mathbf{I}_1. \quad (23)$$

In this case, the single scattering source function describes the direct solar radiation scattered once only, into the direction Ω . The first term in the lower boundary condition denotes the reflection of the direct solar beam by the surface. After the reflection it is considered as the diffuse radiation.

For a *flat water surface*, the corresponding equations are obtained substituting Eq. (21) into Eqs. (16) and (19):

$$\mathbf{J}_s(\tau, \Omega) = \frac{\omega(\tau)}{4} \mathbf{Z}(\tau, \Omega, \Omega_0) \mathbf{I}_1 e^{-\tau/\mu_0} + \frac{\omega(\tau)}{4} \mathbf{Z}(\tau, \Omega; -\mu_0, \varphi_0) \mathbf{R}_F(\mu_0) \mathbf{I}_1 e^{-(2\tau_a - \tau)/\mu_0}, \quad (24)$$

$$\mathbf{I}(\tau_0, \Omega) = \mathcal{R}\mathbf{I}(\tau_0, \Omega') + \epsilon B(T_s) \mathbf{I}_1. \quad (25)$$

Compared to Eq. (22), the single scattering source function contains now an additional term that describes the radiation specularly reflected from the air–water interface and then scattered once only, into the direction Ω . The lower boundary condition does not contain any contribution from the reflection of the direct light because it is already included in the single scattering source function.

4.2.2. Ocean

The radiative transfer through the ocean is considered in the framework of an uncoupled RT model assuming a fully transparent non-scattering atmosphere, i.e. the optical thickness of the atmosphere is assumed to be zero. In this case, the direct solar radiation reaching an optical depth τ within the ocean is given by

$$\mathbf{D}_o(\tau, \Omega) = \pi \delta(\mu - \mu'_0) \delta(\varphi - \varphi_0) \frac{\mu_0}{\mu'_0} \mathbf{T}_F(\mu_0) \mathbf{I}_1 e^{-\tau/\mu}. \quad (26)$$

Here, $\mathbf{T}_F(\mu_0)$ is the Fresnel transmission matrix of the air–water interface (see below), τ is the optical depth within the ocean, and μ'_0 is the cosine of the solar angle within the ocean given by Snell's law [99] as $\mu'_0 = \sqrt{1 - (1 - \mu_0^2)/n^2}$, where n is the real part of the water refractive index. Throughout this study, we assume the refractive index of the air to be equal to 1. The multiplier μ_0/μ'_0 is introduced in Eq. (26) to ensure the energy conservation of the direct solar radiation when crossing the air–water interface.

Substituting Eq. (26) into Eqs. (16) and (19), we obtain the single scattering source function and lower boundary condition for the ocean:

$$\mathbf{J}_s(\tau, \Omega) = \frac{\omega(\tau)}{4} \frac{\mu_0}{\mu'_0} \mathbf{Z}(\tau, \Omega; \mu'_0, \varphi_0) \mathbf{T}_F(\mu_0) \mathbf{I}_1 e^{-\tau/\mu'_0}, \quad (27)$$

$$\mathbf{I}(\tau_0, \Omega) = \mathbf{R}(\Omega, \mu'_0, \varphi_0) \mathbf{I}_1 \mu'_0 e^{-\tau_0/\mu'_0} + \mathcal{R}\mathbf{I}(\tau_0, \Omega') + \epsilon B(T_s) \mathbf{I}_1, \quad (28)$$

where \mathbf{Z} is the phase matrix of the ocean water and $\mathbf{R}(\Omega, \mu'_0, \varphi_0)$ describes the reflection properties of the ocean bottom. The single scattering source function describes the direct solar radiation transmitted through the air–water interface and scattered once only, into the direction Ω . In

SCIATRAN, the transfer of the direct solar radiation through the ocean is modeled neglecting the water roughness, i.e. the ocean–atmosphere interface is assumed to be flat. Furthermore, a specular reflection from the ocean bottom is not considered.

Unlike the atmosphere, the upper boundary condition for the ocean has to account for a discontinuity of the refractive index in the ocean–atmosphere interface. This discontinuity results in the Fresnel reflection of the upwelling radiation at the top of the ocean, i.e. a part of the energy is reflected back into the ocean. For a wind-roughened ocean surface, the following expression for the upper boundary condition is appropriate:

$$\mathbf{I}(0, \Omega) = \mathcal{R}_w \mathbf{I}(0, \Omega'), \quad \mu > 0, \quad (29)$$

where $\mathcal{R}_w = (1/\pi) \int_0^{2\pi} d\varphi' \int_{-1}^0 d\mu' \mu' \mathbf{R}_w(\Omega, \Omega') \otimes$ is a linear integral operator, $\mathbf{R}_w(\Omega, \Omega')$ is a 4×4 matrix determining angular reflection properties of the upper ocean boundary, and $\mathbf{I}(0, \Omega)$ denotes the Stokes vector of the radiation reflected from the ocean–atmosphere interface back to the ocean. For a flat ocean surface, the linear integral operator \mathcal{R}_w has to be replaced by the Fresnel reflection matrix $\mathbf{R}_F(\mu')$.

4.2.3. Coupled ocean–atmosphere system

For a coupled ocean–atmosphere system, the upper boundary condition in the atmosphere and the lower boundary condition in the ocean remain the same as for uncoupled systems, see Eqs. (18) and (28), respectively. In contrast, the lower boundary condition in the atmosphere and the upper boundary condition in the ocean need to be modified to account for the interaction between the atmosphere and ocean. In particular, at the lower boundary of the atmosphere, a part of the energy is transmitted through the air–water interface from the ocean to the atmosphere. For a wind-roughened ocean surface, this results in the following boundary condition in place of Eq. (23):

$$\mathbf{I}_a(\tau_0, \Omega) = \mathbf{R}(\Omega, \Omega_0) \mathbf{I}_1 \mu_0 e^{-\tau_0/\mu_0} + \mathcal{R} \mathbf{I}_a(\tau_0, \Omega') + \epsilon B(T_s) \mathbf{I}_1 + \mathcal{T}_{wa} \mathbf{I}_w(0, \Omega'), \quad \mu < 0, \quad (30)$$

where $\mathbf{I}_w(0, \Omega')$ is the Stokes vector of the radiation field just below the ocean–atmosphere interface, $\mathcal{T}_{wa} = \int_0^{2\pi} d\varphi' \int_{-1}^0 d\mu' \mathbf{T}_{wa}(\Omega, \Omega') \otimes$ is the transmission operator, and $\mathbf{T}_{wa}(\Omega, \Omega')$ is a 4×4 matrix determining the angular transmission properties of the air–water interface illuminated from below. The last term in Eq. (30) is referred to as the water leaving radiation. The subscripts “a” and “w” are used to distinguish between the parameters of the radiation field within the atmosphere (a) and within the ocean (w).

In contrast to the uncoupled ocean model, an absorbing and scattering atmosphere in the coupled system affects the incident radiation at the top of the ocean. First of all, accounting for the attenuation by the atmosphere, Eq. (26) for the direct solar radiation reaching an optical depth τ within the ocean needs to be rewritten as

$$\mathbf{D}_0(\tau, \Omega) = \pi \delta(\mu - \mu'_0) \delta(\varphi - \varphi_0) \frac{\mu_0}{\mu'_0} \mathbf{T}_F(\mu_0) \mathbf{I}_1 e^{-\tau_a/\mu_0} e^{-\tau/\mu}, \quad (31)$$

where τ_a is the total optical thickness of the atmosphere. Consequently, the single scattering source function is

given by the following expression in place of Eq. (27):

$$\mathbf{J}_s(\tau, \Omega) = \frac{\omega(\tau) \mu_0}{4 \mu'_0} \mathbf{Z}(\tau, \Omega; \mu'_0, \varphi_0) \mathbf{T}_F(\mu_0) \mathbf{I}_1 e^{-\tau_a/\mu_0} e^{-\tau/\mu'_0}. \quad (32)$$

Because of the scattering in the overlying atmosphere, the upper boundary of the ocean is illuminated from above not only by the direct solar light but also by the diffuse radiation. Therefore, the upper boundary condition in the ocean has to be modified to contain the diffuse radiation transmitted from the atmosphere into the ocean:

$$\mathbf{I}_w(0, \Omega) = \mathcal{R}_w \mathbf{I}_w(0, \Omega') + \mathcal{T}_{aw} \mathbf{I}_a(\tau_a, \Omega'), \quad \mu > 0. \quad (33)$$

Here, $\mathbf{I}_a(\tau_a, \Omega')$ is the Stokes vector of the radiation field just above the ocean–atmosphere interface, $\mathcal{T}_{aw} = \int_0^{2\pi} d\varphi' \int_0^1 d\mu' \mathbf{T}_{aw}(\Omega, \Omega') \otimes$ is the transmission operator, and $\mathbf{T}_{aw}(\Omega, \Omega')$ is a 4×4 matrix determining the angular transmission properties of the air–water interface illuminated from the above.

The boundary conditions and expressions for the single scattering source function discussed in Sections 4.2.1–4.2.3 are summarized in Table 2. We note that the transfer of the direct solar radiation through the ocean is modeled neglecting the wind-roughness of the water surface, i.e. a flat air–water interface is assumed. This is why the single scattering source function, $\mathbf{Q}_w(\tau, \Omega)$, in the right panel of Table 2 is the same for a wind-roughened and for a flat ocean surface.

The VRTE formulated at the beginning of this section along with the appropriate boundary conditions as listed in Table 2 can be used to model the radiation field in the atmosphere and ocean. The simulations can be done in the spectral region from the UV to thermal infrared. The explicit notation of the wavelength dependence for all relevant quantities is omitted throughout the paper.

5. Solving the vector radiative transfer equation

As discussed above, a radiative transfer equation along with appropriate boundary conditions represents the so-called boundary value problem. Comprehensive reviews of numerical methods to solve BVPs related to the radiative transfer through the terrestrial atmosphere have been presented by Lenoble [56] and Mishchenko et al. [91] for scalar and vector RTEs, respectively. In this study, we consider only the source function integration technique and discrete-ordinates method, which are employed in the SCIATRAN radiative transfer model.

5.1. Formal solution of VRTE

The most general way to solve VRTE is provided by its formal solution. This method is often referred to as the source function integration technique [100,101]. Applying the standard technique for solving first-order differential equations (see e.g. [6,102,96]) to VRTE given by Eq. (17), its formal solution is written as

$$\mathbf{I}(\tau, +\mu, \varphi) = \mathbf{I}(0, +\mu, \varphi) e^{-\tau/\mu} + \frac{1}{\mu} \int_0^\tau \mathbf{J}(\tau', +\mu, \varphi) e^{-(\tau-\tau')/\mu} d\tau', \quad (34)$$

Table 2

The upper boundary condition (UBC), single scattering source function (SSF), and lower boundary (LBC) condition for a coupled ocean–atmosphere system. For uncoupled models, omit the terms underlined by curly brackets.

	Atmosphere	Ocean
<i>Wind-roughed ocean surface</i>		
UBC	$\mathbf{0}$	$\mathcal{R}_w \mathbf{I}_w(0, \Omega') + \mathcal{T}_{aw} \mathbf{I}_a(\tau_a, \Omega')$
SSF	$\mathbf{Q}_a(\tau, \Omega)$	$\mathbf{Q}_w(\tau, \Omega) \underbrace{e^{-\tau_a/\mu_0}}$
LBC	$\mathbf{R}(\Omega, \Omega_0) \mathbf{I}_1 \mu_0 e^{-\tau_0/\mu_0} + \mathbf{I}_a^\dagger(\tau_0, \Omega) + \mathcal{T}_{wa} \mathbf{I}_w(0, \Omega')$	$\mathbf{I}_w^\dagger(\tau_0, \Omega)$
<i>Flat ocean surface</i>		
UBC	$\mathbf{0}$	$\mathbf{R}_F(\mu') \mathbf{I}_w(0, \Omega') + \mathcal{T}_F(\mu') \mathbf{I}_a(\tau_a, \Omega')$
SSF	$\mathbf{Q}_a(\tau, \Omega) + \frac{\omega(\tau)}{4} \mathbf{Z}(\tau, \Omega; -\mu_0, \varphi_0) \mathbf{R}_F(\mu_0) \mathbf{I}_1 e^{-(2\tau_a - \tau)/\mu_0}$	$\mathbf{Q}_w(\tau, \Omega) \underbrace{e^{-\tau_a/\mu_0}}$
LBC	$\mathbf{I}_a^\dagger(\tau_0, \Omega) + \mathcal{T}_F(\mu') \mathbf{I}_w(0, \Omega')$	$\mathbf{I}_w^\dagger(\tau_0, \Omega)$
<i>Definitions</i>		
	$\mathbf{Q}_a(\tau, \Omega) = \frac{\omega_a(\tau)}{4} \mathbf{Z}_a(\tau, \Omega, \Omega_0) \mathbf{I}_1 e^{-\tau/\mu_0}$	
	$\mathbf{I}_a^\dagger(\tau_0, \Omega) = \mathcal{R} \mathbf{I}_a(\tau_a, \Omega') + \epsilon B_a(T_s) \mathbf{I}_1$	
	$\mathbf{Q}_w(\tau, \Omega) = \frac{\omega_w(\tau)}{4} \frac{\mu_0}{\mu'} \mathbf{Z}_w(\tau, \Omega; \mu'_0, \varphi_0) \mathbf{T}_F(\mu_0) \mathbf{I}_1 e^{-\tau/\mu'_0}$	
	$\mathbf{I}_w^\dagger(\tau_0, \Omega) = \mathbf{R}(\Omega, \mu'_0, \varphi_0) \mathbf{I}_1 \mu'_0 e^{-\tau_0/\mu'_0} + \mathcal{R} \mathbf{I}_w(\tau_w, \Omega') + \epsilon B_w(T_s) \mathbf{I}_1$	

$$\mathbf{I}(\tau, -\mu, \varphi) = \mathbf{I}(\tau_0, -\mu, \varphi) e^{-(\tau_0 - \tau)/\mu} + \frac{1}{\mu} \int_{\tau}^{\tau_0} \mathbf{J}(\tau', -\mu, \varphi) e^{-(\tau' - \tau)/\mu} d\tau', \quad (35)$$

where the total source function, $\mathbf{J}(\tau, \pm\mu, \varphi)$, is given by the sum of the multiple scattering, internal emission, and single scattering source functions:

$$\mathbf{J}(\tau, \pm\mu, \varphi) = \mathbf{J}_m(\tau, \pm\mu, \varphi) + \mathbf{J}_e(\tau, \pm\mu, \varphi) + \mathbf{J}_s(\tau, \pm\mu, \varphi). \quad (36)$$

The positive or negative sign of the polar angle cosine, μ , denotes the downward or upward direction of the radiation and source function, respectively. The Stokes vectors at the upper and lower boundaries of the medium are represented by $\mathbf{I}(0, +\mu, \varphi)$ and $\mathbf{I}(\tau_0, -\mu, \varphi)$, respectively, and determined by the boundary conditions.

The formal solution of VRTE represented by Eqs. (34) and (35) can be applied to practical RT problems if the source function, $\mathbf{J}(\tau, \pm\mu, \varphi)$, on the right hand side of both equations is known. Most commonly, the single scattering and internal emission parts of the source function can be either derived analytically or easily calculated numerically, whereas the multiple scattering source function is generally unknown. In the framework of the SCIATRAN model, the source function integration technique (i.e. the formal solution of VRTE) is employed as follows:

- When modeling observations of the direct solar light transmitted through the Earth's atmosphere the contribution of all scattering processes can be neglected. This means that the total source function, $\mathbf{J}(\tau, \pm\mu, \varphi)$, is equal to zero and Eq. (34) results in

$$\mathbf{I}(\tau, \mu_0, \varphi_0) = \pi e^{-\tau/\mu_0} \mathbf{I}_1, \quad (37)$$

where μ_0 is the cosine of the solar zenith angle and the boundary condition given by Eq. (11) is taken into account. This expression describing the exponential

attenuation of the direct solar light is known as the Beer–Lambert law, see e.g. [103]. Using the Characteristics method [104] a similar solution can be obtained for a spherical atmosphere as well.

- Neglecting the multiple scattering contribution (i.e. $\mathbf{J}_m(\tau, \pm\mu, \varphi)$ is set to zero), the formal solution of VRTE provides the so-called single scattering approximation. The latter is useful for modeling the radiation field in spectral ranges where either the gaseous absorption is strong or the total optical thickness is small, i.e. the contribution of the multiply scattered radiation to the entire signal is insignificant. Furthermore, this approximation is used by the single scattering correction algorithm [105,106]. The latter is aimed at improving the modeling accuracy when using phase function truncation techniques (see e.g. [107] and references therein).
- After the multiple scattering source function is obtained at Gaussian quadrature points [103,36] using the discrete-ordinates method (see below), the source function integration technique is employed to calculate the Stokes vectors for user-defined directions (post-processing algorithm).
- When calculating a fully spherical or an approximative spherical solution, the formal solution of VRTE is employed iteratively. This means that the integration on the right hand sides of Eqs. (34) and (35) is done with the multiple scattering source function resulting from a lower-order approximation. A detailed discussion of this method is presented by Rozanov et al. [108,109,48].

5.2. Angular discretization of VRTE

Most of the numerical methods for solving VRTE require discretization with respect to angular variables

(polar and azimuthal angles). This discretization is essential for transforming the integro-differential RT equation into the ordinary differential equation. In addition to the discretization, a separation technique is widely used allowing the dependencies on polar and azimuthal angles to be treated independently. Most commonly, the Stokes vector and phase matrix are expanded in the Fourier series resulting in a system of RT equations for Fourier harmonics of the Stokes vector [110,111,36]. Each of those equations can be solved then independently.

The expansion of scattering matrix elements is usually performed using either the generalized spherical functions $P_{mn}^s(\cos \gamma)$ [112,110] or Wigner d-functions $d_{mn}^s(\gamma) = i^{n-m} P_{mn}^s(\cos \gamma)$ [90]. Owing to the recurrence algorithm presented by Mishchenko et al. [91], the latter approach is computationally more efficient, and has thus been preferred for the implementation in SCIATRAN. Coefficients of the expansion of scattering matrix elements in a series of generalized spherical functions are commonly referred to as the Greek constants (see e.g. [113,9,110,111] for details).

The discretization over the polar angle is done representing the radiation field by a number of upwelling and downwelling streams. Both the upwelling, $\mathbf{I}_-(\tau)$, and downwelling, $\mathbf{I}_+(\tau)$, radiations are defined then by the following column vectors:

$$\mathbf{I}_\pm(\tau) = [\mathbf{I}^T(\tau, \pm\mu_1), \mathbf{I}^T(\tau, \pm\mu_2), \dots, \mathbf{I}^T(\tau, \pm\mu_N)]^T, \quad (38)$$

where μ_i are the quadrature points of the double-Gauss scheme adopted in SCIATRAN (see e.g. [103] for details), N is the total number of the quadrature points, and the superscript T denotes the transpose operation.

Within the atmosphere, the Gaussian-quadrature points and weights are always the same. On the contrary, this is not the case for a coupled ocean-atmosphere system where strong refraction of light occurs at the air-water interface. For a flat sea surface, the incident radiation penetrating from the atmosphere into the ocean is refracted within the so-called Fresnel cone. Independent of the incidence direction, the polar (zenith) angle of the refracted beam cannot be larger than the critical angle (about 48.3° for the air and sea water). Thus, the 0 – 90° angle interval for the incident light in the atmosphere is projected into the 0 – 48.3° interval for the refracted light in the ocean, and some additional nodes are needed to account for the light traveling through the ocean outside the Fresnel cone. Similar to Jin et al. [39], the SCIATRAN model merges the directions of the refracted light corresponding to the Gaussian-quadrature incidence directions with additional quadrature points covering the polar angle range outside the Fresnel cone. This merged grid is often referred to as the coupled underwater quadrature points. A detailed discussion of this method is given by He et al. [66].

5.3. Discrete-ordinates method

As discussed above, the separation technique results in splitting the VRTE into independent equations for azimuthal Fourier terms, and the discretization of the polar angle allows all angular integrals to be replaced by finite sums. As a result, for each azimuthal Fourier term a system

of coupled first order linear ordinary differential equations for the Stokes vectors of the up- and downwelling radiation as functions of the optical depth τ is obtained.

In the framework of the discrete-ordinates method, the general solution of this differential equation system is found assuming a vertically homogeneous medium. Following Siewert [35,36], the solution is written as

$$\mathbf{I}_\pm(\tau) = \mathbf{I}_\pm^h(\tau; C_1, \dots, C_{N_c}) + \mathbf{I}_\pm^p(\tau), \quad (39)$$

where $\mathbf{I}_\pm^h(\tau; C_1, \dots, C_{N_c})$ is the general solution of the homogeneous equation (i.e. the right hand side is set to zero), $\mathbf{I}_\pm^p(\tau)$ is a particular solution of the inhomogeneous equation, and C_j are arbitrary constants (j runs from 1 to N_c). The number of constants, N_c , is equal either to $2N$ or to $8N$ for the scalar or vector RTE, respectively, where N is the number of the Gaussian-quadrature points. The constants are to be determined from the boundary conditions. The analytical expressions for $\mathbf{I}_\pm^h(\tau; C_1, \dots, C_{N_c})$ and $\mathbf{I}_\pm^p(\tau)$ are given in Appendix A. Further details on the solution method, its numerical implementation in SCIATRAN, and selected applications to the radiative transfer through a single homogeneous layer are presented by Rozanov and Kokhanovsky [42].

In the case of a vertically inhomogeneous medium, the latter is assumed to consist of several homogeneous layers. The solution of VRTE, see Eq. (39), has to be found for all layers and contains $L \times N_c$ arbitrary constants, where L is the number of layers. These constants are obtained by requiring continuity of the Stokes vector across the layer interfaces and satisfaction of the boundary conditions. Details on how to formulate the linear algebraic system for a vertically inhomogeneous medium are given in Appendix B.

As mentioned above, the Stokes vector for directions not matching the Gaussian-quadrature points can be obtained using the post-processing algorithm which implies the formal solution of VRTE as given by Eqs. (34) and (35). In these equations, the integration over the optical depth τ within each homogeneous layer is performed analytically.

5.4. Conservative scattering

As discussed in detail in Appendix A, the general solution of the homogeneous equation, which is needed in the framework of the discrete-ordinates method, see Eq. (39), is obtained as a linear combination of all elementary solutions, $\Phi(\nu_j, \mu_i) e^{-\tau/\nu_j}$, see Eq. (A.14). The latter is found solving the eigenvalue problem given by Eq. (A.28). In a non-absorbing medium (conservative scattering), one of the eigenvalues, λ , is equal to zero, i.e. a pair of the separation constants, $\nu = \pm \sqrt{1/\lambda}$, is infinite leading to a loss of two elementary solutions. In the SCIATRAN model, missing elementary solutions in the case of conservative scattering are replaced by analytical solutions as suggested by Chandrasekhar [6]. Further details on the general solution of the homogeneous equation in the case of conservative scattering can be found in [36,114].

Using the above-mentioned technique, the accuracy of the so-called pseudo-absorber approximation can be

investigated. This approximation is widely used in the framework of the discrete-ordinates technique to avoid a special treatment of the conservative scattering case. Essentially, one introduces a weak fake absorption within a non-absorbing layer. However, a too weak absorption causes a numerical instability whereas too large absorption results in systematic errors in the simulated radiation. To demonstrate this, we compare the reflected radiation at the top of a non-absorbing homogeneous layer with a black underlying surface ($A=0$) calculated by employing the analytical solution and pseudo-absorber approximation. The RT calculations are done for a solar zenith angle of 36.87° ($\mu_0 = 0.8$), polar angle cosines of 0.01, 0.1, 0.2, ..., 0.9, 1.0 and seven azimuthal angles between 0° and 180° in 30° steps. The results of the comparison are presented in Fig. 2. The relative errors are averaged over all viewing geometries and shown as functions of the absorption probability of the pseudo-absorber, $p = 1 - \omega$, where ω is the single scattering albedo. The simulations are done for phase functions typical for the Rayleigh (left panels) and aerosol (right panels) scattering for layer optical thicknesses of 0.2 and 2. The plots reveal a strong dependence of the modeling error on the absorption probability. In the considered examples, minimum errors occur at $p \approx 1 \times 10^{-4}$. The amplitude of the error strongly depends on the phase function and optical thickness of the layer. Thus, for example, for an absorption probability of $\sim 1 \times 10^{-4}$, the error is only $\sim 0.001\%$ for the Rayleigh phase function and $\tau_0 = 0.2$ (see upper left panel of Fig. 2), whereas it reaches $\sim 0.1\%$ for an aerosol phase function and $\tau_0 = 2$ (see lower right panel of Fig. 2). Furthermore, when decreasing the absorption probability

below the optimal value, the approximation error increases. For example, in the case of aerosol scattering, the approximation error reaches $\sim 10\%$ if p is decreased to $\sim 5 \times 10^{-7}$. Thus, using a too weak or a too strong pseudo-absorber might significantly influence accuracy of the solution.

5.5. Phase function truncation technique

For a scattering medium which is characterized by a highly stretched phase function, the RT calculations using the Fourier series expansion approach are typically time consuming. This is because a large number of phase function expansion terms is needed for an accurate representation of the strong forward scattering. The increase of computational burden is explained by the fact that in the framework of discrete-ordinates method the scattering integral in Eq. (A.11) has to be calculated numerically and, thus, is replaced by a finite sum as given by Eq. (A.13). With increasing number of Fourier series terms, K , in the expansion of the phase matrix, see Eq. (A.1), the associated Legendre functions and generalized spherical functions under the scattering integral oscillate stronger (see e.g. Appendix F in [91]). Therefore, to perform the numerical integration with a desired accuracy one needs to increase the number of Gaussian-quadrature points, N , in Eq. (A.13). In particular, it was shown that $N=K/2$ ensures numerically stable results [103]. Furthermore, dimensions of the basic eigenvalue problem to obtain the eigenvectors and separation constants (see Eq. (A.24)) as well as of the linear algebraic system (see Eq. (B.12)) to

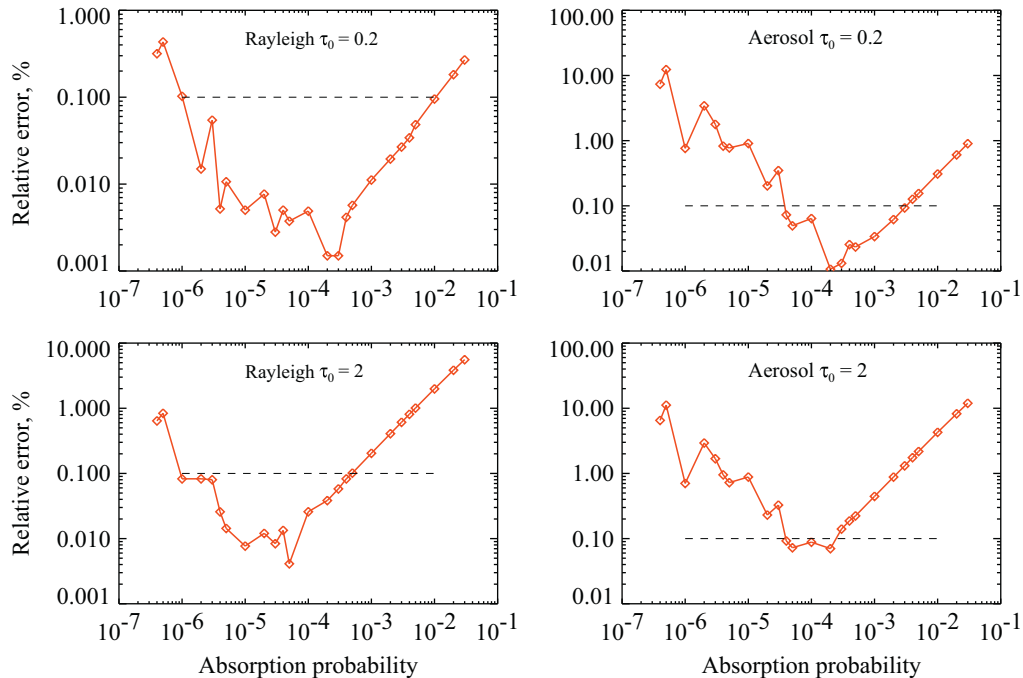


Fig. 2. Approximation error as a function of absorption probability ($1-\omega$) caused by introducing a pseudo-absorber. Calculations of the reflected intensity at the top of a homogeneous layer without absorption using a black underlying surface ($A=0$) were performed employing the exact analytical solution and pseudo-absorber approximation.

obtain arbitrary constants increase with N resulting in an increase of the computation time.

A trade-off between the modeling accuracy and computational efficiency can be achieved by employing the phase function truncation technique, which uses an approximation to replace the forward scattering cone of the phase function. In scalar radiative transfer problems, the most common approximations are provided by the Delta function [115], Delta-fit [116], and Delta-M [117] methods. Modeling errors resulting from different methods have been analyzed both theoretically and numerically by Rozanov and Lyapustin [107]. In particular, it has been demonstrated that the combination of the Delta-M method with the single scattering correction technique [106] provides the best overall accuracy of the modeled radiation. The Delta-M method has also been demonstrated to be suitable for an extension to the vector radiative transfer problems [118,119].

For the reasons discussed above, the Delta-M method has been preferred for the implementation in SCIATRAN. In the framework of this method, the expansion coefficients of the scattering matrix elements, i.e. Greek constants, are written after transformation as follows:

$$\tilde{\alpha}_{i,m} = \frac{\alpha_{i,m} - f(2m+1)}{1-f}, \quad i = 1, 2, 3, 4; \quad (40)$$

$$\tilde{\beta}_{i,m} = \frac{\beta_{i,m}}{1-f}, \quad i = 1, 2; \quad (41)$$

where the parameter f is defined as

$$f = \frac{\alpha_{i,M}}{2M+1}. \quad (42)$$

All expansion coefficients with $m > M$ are set to zero, i.e. the corresponding expansion terms are skipped. Truncation of the scattering matrix expansion series requires an appropriate scaling of the optical parameters. The scaling is done for both scalar and vector RTEs as follows:

$$\tilde{\sigma}_s = \sigma_s(1-f), \quad \tilde{\sigma}_e = \sigma_e + \sigma_s f, \quad \tilde{\omega} = \frac{1-f}{1-\omega f}, \quad (43)$$

where σ_s , σ_e , ω are the scattering cross section, extinction cross section, and single scattering albedo, respectively, and the scaled quantities are marked by tildes.

It is worth noting that Eqs. (40) and (42) are written under the assumption that the expansion coefficients of the scattering matrix include the common multiplier $(2m+1)$. Otherwise, as used e.g. by Min and Duan [119], the multiplier $(2m+1)$ in Eq. (40) and the denominator $2M+1$ in Eq. (42) have to be removed.

5.6. Truncation of the Fourier series

Depending on the observation and illumination geometries the azimuthal dependence of the Stokes vector might be weak requiring much less Fourier series terms to be approximated with sufficient accuracy. This is the case, for example, for near-nadir or near-zenith observations. A common technique widely used in such situations to reduce computational costs is to truncate the azimuthal Fourier series if sufficient approximation accuracy is achieved. This is done based on a prescribed convergence criterion.

In the SCIATRAN model, significance of the next Fourier term is determined from its relative contribution into each non-zero component of the Stokes vector:

$$\varepsilon_i(\tau_v, \Omega_v, \Omega_s; K') = 1 - \mathbf{I}_i^{K'-1}(\tau_v, \Omega_v, \Omega_s) / \mathbf{I}_i^{K'}(\tau_v, \Omega_v, \Omega_s). \quad (44)$$

Here, $\{\tau_v, \Omega_v, \Omega_s\}$ represent the altitude, light traveling direction and illumination geometry, respectively, i runs through components of the Stokes vector, and superscripts $K'-1$ and K' denote the so-called partial sums, i.e. the Stokes vectors obtained accounting for $K'-1$ and K' Fourier terms, respectively. Decisive is the maximum relative contribution calculated for all altitudes, light traveling directions, illumination geometries, and Stokes components as follows:

$$\varepsilon(K') = \max_i |\varepsilon_i(\tau_v, \Omega_v, \Omega_s; K')|. \quad (45)$$

The convergence is reached if two subsequent maximum relative contributions are below the prescribed criterion, ε_c :

$$\varepsilon(K') \leq \varepsilon_c \quad \text{and} \quad \varepsilon(K'+1) \leq \varepsilon_c. \quad (46)$$

5.7. Internal thermal emission

As mentioned in Section 4.1, the internal thermal emission is accounted for by including the corresponding source term in the RTE, see Eqs. (5) and (7). The Planck function describing the thermal emission is isotropic and depends on the vertical coordinate τ . Although the Planck function can be easily calculated at any point in the medium, its analytical representation (as a function of τ) is too complicated to be used in the framework of the discrete-ordinates method. Most commonly, an exponential approximation of the Planck function is used instead [120–123]. An efficient parameterization implemented in the SCIATRAN model is discussed below.

For a finite atmospheric layer with top and bottom optical depths of τ_{l-1} and τ_l , respectively, we assume the Planck function to be calculated from its analytical representation at the top and bottom of the layer (B_{l-1} and B_l , respectively) and approximated by a sine Fourier series within the layer:

$$B(\tau) = B_{l-1} e^{-b_0(\tau-\tau_{l-1})} \left[1 + \sum_{k=1}^K a_k \sin(kx) \right], \quad (47)$$

where $x = \pi(\tau - \tau_{l-1}) / \Delta\tau_l$, $\Delta\tau_l = \tau_l - \tau_{l-1}$ is the optical thickness of the layer, and the coefficient b_0 is calculated from the Planck function values at the layer boundaries:

$$b_0 = \frac{1}{\Delta\tau_l} \ln \frac{B_{l-1}}{B_l}. \quad (48)$$

This ensures that exact values of the Planck function are reproduced at the top and bottom of each atmospheric layer. The coefficients a_k are fitted to provide the best match within the layer between the approximation and the Planck function calculated from its analytical representation.

As discussed in detail in Appendix A.3, τ -dependent coefficients in the particular solution of the inhomogeneous RTE, see Eqs. (A.46) and (A.47), are obtained integrating the inhomogeneous source term with an exponential function

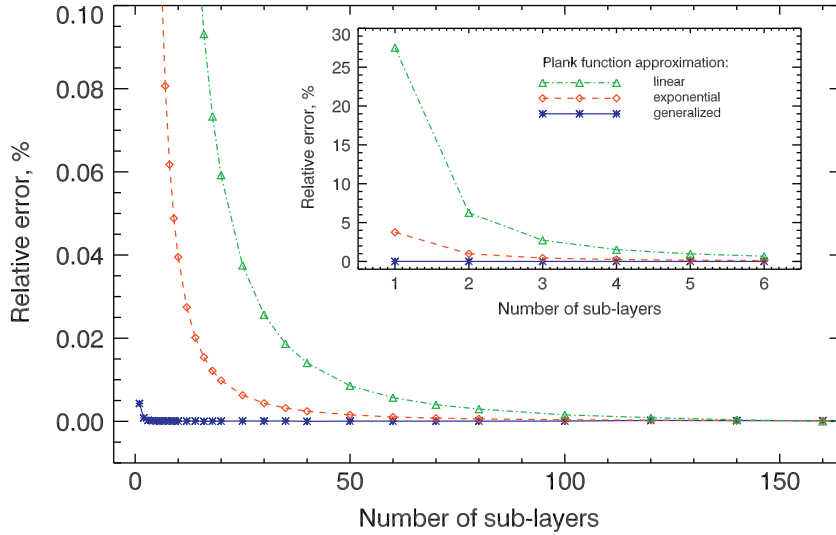


Fig. 3. Relative errors in the outgoing radiation resulting from different Planck function approximations (see text).

[36]. Thus, it is convenient to rewrite the Planck function approximation given by Eq. (47) to contain exponential functions as well. Introducing the complex exponent $e^{ikx} = \cos(kx) + i \sin(kx)$, we obtain

$$B(\tau) = B_{l-1} e^{-b_0(\tau-\tau_{l-1})} \left[1 + \sum_{k=1}^K a_k \operatorname{Im}\{e^{ikx}\} \right], \quad (49)$$

where $\operatorname{Im}\{\}$ denotes the imaginary part of a complex function and i is the imaginary unity. Taking into account that all coefficients a_k are real, this expression can be rewritten as follows:

$$B(\tau) = B_{l-1} \operatorname{Im}\left\{ \sum_{k=0}^K a_k e^{-b_k(\tau-\tau_{l-1})} \right\}, \quad (50)$$

where $a_0 = i$ and $b_k = b_0 - \pi k i / \Delta\tau_l$.

Following from the discussion above, the Planck function within each atmospheric layer can be represented by a sum of exponential terms. This approximation provides the following advantages:

- Representing the Planck function according to Eq. (50) is a generalization of the approximations used before. In particular, the exponential approximation suggested by Kylling and Stamnes [122] in the framework of the exponential-linear-in-depth approximation and used later by Fu and Liou [120], Fu et al. [121], and Rathke and Fischer [123] is obtained from Eq. (50) restricting the sum to the zeroth term:

$$B(\tau) = B_{l-1} e^{-b_0(\tau-\tau_{l-1})}. \quad (51)$$

In the case of a small gradient of the Planck function within a given atmospheric layer, this results in

$$B(\tau) = B_{l-1} + (B_l - B_{l-1}) \frac{\tau - \tau_{l-1}}{\Delta\tau_l}. \quad (52)$$

This expression represents the linear-in-optical-depth approximation suggested by Wiscombe [124] and

implemented later in the RT codes DISORT [34] and LIDORT [41].

- In a plane-parallel medium, the optical depth integrals in the particular solution of the inhomogeneous RTE, see Eqs. (A.46) and (A.47), can be written in a similar form as for the direct solar radiation and, thus, can be calculated in the same manner.
- In the SCIATRAN model, an input parameter controls the accuracy of the parameterization given by Eq. (50). Thus, the required number of terms is determined individually for each atmospheric layer depending on the Planck function gradient within the layer and desired approximation accuracy.

The performance of the generalized Planck function parameterization implemented in SCIATRAN, see Eq. (50), in comparison to the exponential and linear approximations given by Eqs. (51) and (52), respectively, is illustrated in Fig. 3. For the generalized parameterization, the approximation accuracy of 0.01% is selected. The linear approximation results are obtained using the standard DISORT code¹ and the exponential approximation is simulated by SCIATRAN in accordance with Eq. (51). The calculations are performed at 3.7 μm wavelength including the absorption by H_2O , CH_4 , and N_2O . The vertical distribution of the species corresponds to a tropospheric layer between 0 and 10 km and the temperature gradient is about 6 K/km. The layer is illuminated by the solar radiation incident at an angle of 30°. The internal thermal radiation is taken into account. The calculations are done for ten polar angles (from 0° to 80° with a step of 10°, and for 85°) and three azimuthal angles (i.e. 0°, 90°, 180°). The presented results are averaged over all viewing geometries. The figure shows relative errors in the outgoing radiation at the top of the

¹ Available via ftp://climate.gsfc.nasa.gov/pub/wiscombe/Multiple_Scatt/.

medium, resulting from different Planck function approximations. The relative error is calculated with respect to the solution obtained with 200 sub-layers (considered as true). Fig. 3 reveals that the approximation error decreases with the number of sub-layers. This is because the error is mainly determined by the layer inhomogeneity. It follows that the solution obtained employing the generalized approximation for the Planck function differs from the true solution by less than 0.01% even without any sub-layering. For the exponential and the linear approximations, a comparable accuracy is achieved by using 20 and 50 sub-layers, respectively.

The results shown in Fig. 3 are obtained for an aerosol optical thickness of 1, which is found to be the worst case with respect to the performance of both exponential and linear approximation methods. Although, for other aerosol optical thicknesses less sub-layers are required to obtain an accurate solution, the overall conclusions with respect to the relative performance of the approximations remain the same.

5.8. Pseudo-spherical approximation

In the discussion above, the atmosphere was assumed to consist of several plane-parallel layers (the so-called plane-parallel atmosphere). Although this approximation is widely used in radiative transfer theory, it is not always applicable or might result in significant modeling errors. In particular, inaccurate results might be obtained at large solar zenith angles, and no calculations are possible if the Sun is below the horizon. This limitation can be avoided employing the so-called pseudo-spherical approximation, which has originally been suggested by DeLuisi and Mateer [125] and used thereafter by many authors. This approximation has been shown to provide a sufficient accuracy of the modeled radiation for near-nadir/zenith viewing geometries at solar zenith angles up to about 92° [126,127]. In the pseudo-spherical approximation, the boundary value problem as defined by Eqs. (17)–(19) is formulated in exactly the same way as for the plane-parallel medium, whereas a spherical shell atmosphere is assumed when calculating the attenuation of the direct solar light, which contributes into the single scattering source function, see Eqs. (16) and (20). In other words, the transfer of the scattered light is modeled assuming a plane-parallel medium while the direct solar beam is considered to travel through a spherical shell atmosphere.

When employing the pseudo-spherical approximation, the single scattering source function, which contains the spherical transmission function, does not have any analytical representation within a layer anymore. Thus, similarly to the internal thermal emission discussed in the previous section, a parameterization of the spherical transmission function within a layer is required to solve the resulting boundary value problem in the framework of the discrete-ordinates method. In the simplest case this is done by using an effective solar zenith angle within each altitude layer. The spherical transmission function at any point within an altitude layer $[\tau_{l-1}, \tau_l]$ is approximated then as

$$T_s(\tau) = e^{-\tau_s(\tau)} \approx T_s(\tau_{l-1}) e^{-(\tau-\tau_{l-1})/\mu_e} \equiv T_a(\tau), \quad (53)$$

where μ_e is the cosine of the effective solar zenith angle defined by

$$\mu_e = \frac{\tau_l - \tau_{l-1}}{\tau_s(\tau_l) - \tau_s(\tau_{l-1})} \equiv \frac{\Delta\tau_l}{\Delta\tau_{s,l}}, \quad (54)$$

τ is the vertical optical depth, and $\tau_s(\tau)$ is the optical depth calculated along the direct solar light path in a spherical shell medium (slant optical depth). This approximation referred to as the average secant approximation has been suggested in a slightly different form by Dahlback and Stamnes [127] and implemented in the RT model LIDORT [128]. Although this simple approximation results in correct values at layer boundaries, it cannot reproduce the behavior of the spherical transmission function within a layer with an accuracy sufficient for all practical applications.

A much more sophisticated parameterization is obtained by approximating the behavior of the spherical transmission function within a layer by the sine Fourier series in the same manner as for the Planck function (see Section 5.7):

$$T_a(\tau) = T_s(\tau_{l-1}) e^{-(\tau-\tau_{l-1})/\mu_e} \left[1 + \sum_{k=1}^K a_k \sin \left(k\pi \frac{\tau-\tau_{l-1}}{\Delta\tau_l} \right) \right]. \quad (55)$$

Here, the coefficients a_k are fitted to provide the best match within the layer between the approximation and the spherical transmission function calculated numerically at an appropriate number of sub-layers. This approach has been previously used by Spurr [128] to account for the sphericity of the Earth's atmosphere in the framework of the pseudo-spherical approximation. In contrast to [128] we first rewrite the approximation given by Eq. (55) as a sum of exponential terms. This is done by moving the exponential term inside the square brackets and taking into account that $\sin x = \text{Im}\{e^{ix}\}$:

$$T_a(\tau) = T_s(\tau_{l-1}) \left[e^{-(\tau-\tau_{l-1})/\mu_e} + \sum_{k=1}^K a_k \text{Im} \left\{ e^{-(\tau-\tau_{l-1})(1/\mu_e + ik\pi/\Delta\tau_l)} \right\} \right]. \quad (56)$$

Introducing further

$$\mu_k = \left(\frac{1}{\mu_e} + \frac{ik\pi}{\Delta\tau_l} \right)^{-1} = \frac{\mu_e \Delta\tau_l}{\Delta\tau_l + ik\pi\mu_e}, \quad (57)$$

the parameterization for the spherical transmission function is written as

$$T_a(\tau) = T_s(\tau_{l-1}) \text{Im} \left\{ \sum_{k=0}^K a_k e^{-(\tau-\tau_{l-1})/\mu_k} \right\}, \quad (58)$$

where a_0 is equal to i . The number of terms, K , depends on the optical and geometrical thicknesses of the layer and on the required approximation accuracy. The parameterization of the spherical transmission function given by Eq. (58) allows the particular solution of the inhomogeneous RTE to be obtained in the same way as for a plane-parallel medium (see Appendix A.3 for details).

The performance of the exponential sum approximation given by Eq. (58) is investigated by comparing the spherical transmission functions resulting from this approximation and those calculated for the case where

each layer is divided into 20 sub-layers. The comparisons are performed at solar zenith angles between 70° and 92° and wavelengths of 310 and 600 nm. The atmosphere is assumed to consist of 1 km layers between 0 and 60 km. The required approximation accuracy, which is controlled by a SCIATRAN input parameter, is set to 0.1%. At solar zenith angles of 70° and 80° (not shown here), the zeroth term (equivalent to the average secant approximation given by Eq. (53)) is sufficient to reach the required accuracy almost everywhere. Solely in the lowest altitude layer (0–1 km), two approximation terms are needed at the solar zenith angle of 80° . The results for solar zenith angles of 90° and 92° are presented in Fig. 4. The plot reveals that the average secant approximation is sufficient only above 29–48 km depending on the wavelength and solar zenith angle. At lower altitudes, additional approximation terms are needed. In general, the number of the required terms increases with solar zenith angle and with optical depth. In the lowermost atmospheric layers, highly pronounced maxima are seen in the right panels of Fig. 4. In particular, the maximum number of the exponential terms (19) is needed in two altitude layers at a solar zenith angle of 92° whereas at 90° the approximation fails to reach the requested accuracy in one of the layers.

It is also worth noting that at large solar zenith angles the refraction of light plays a significant role. In particular, the simulated outgoing radiation at the top of the atmosphere is underestimated if the refraction effects are neglected in the RT model. The modeling errors resulting from neglecting the refraction effects for the nadir viewing

geometry have been estimated by Rozanov et al. [85]. At 500 nm wavelength, the error is below 1% for solar zenith angles smaller than 84° , increases then to about 4% at 90° , and exceeds 10% at 92° . In the SCIATRAN model, the spherical transmission function can be calculated accounting for the refractive bending of the direct solar beam as described by Rozanov et al. [85]. In this case, the parameterization of the transmission function is performed in exactly the same manner as discussed above (see Eq. (58)).

5.9. Approximative spherical mode

While the pseudo-spherical approximation provides a sufficient modeling accuracy for near-nadir viewing geometry, it might result in significant errors for off-nadir observations. This has been demonstrated, for example, by Caudill et al. [126] who have found that, depending on the wavelength and viewing angle, a modeling error of up to 10% is expected for the backscattered ultraviolet radiation at a solar zenith angle of 85° . This estimation has been obtained by comparing the results from the pseudo-spherical approximation and from a fully spherical RT model. The main source of modeling errors in the pseudo-spherical approximation is an incorrect treatment of the light paths along the observer line-of-sight. In the SCIATRAN model, this error source is eliminated employing an approximative spherical approach as described by Rozanov et al. [109]. This approach is suitable for both off-nadir/-zenith and limb viewing geometries. A similar

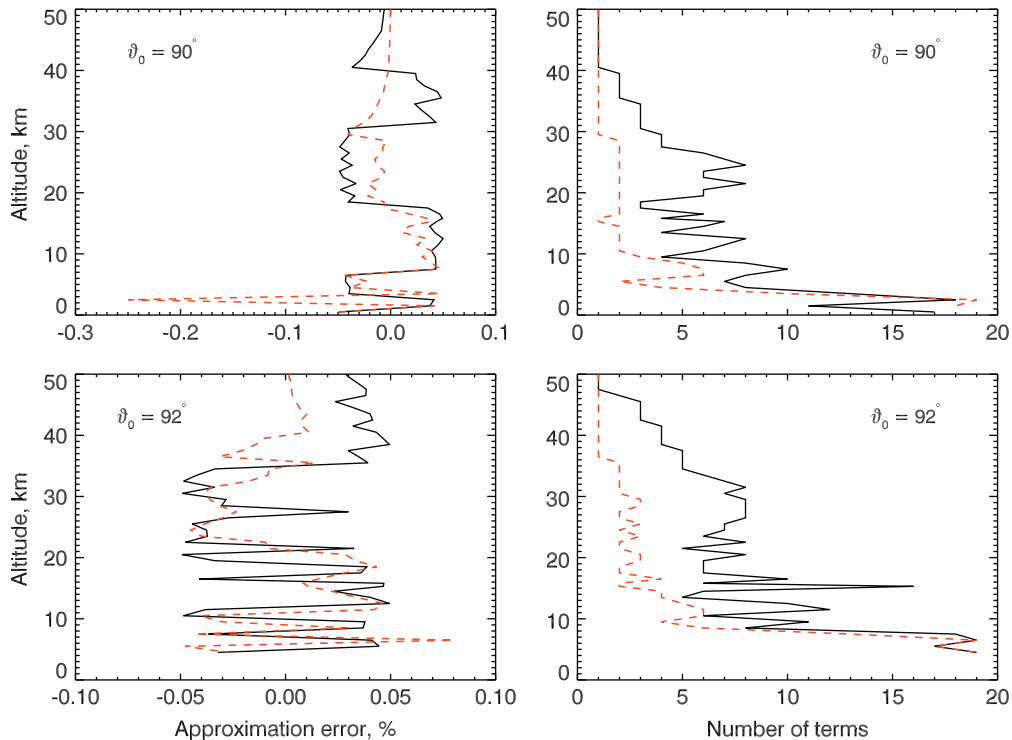


Fig. 4. Performance of the spherical transmission function parameterization. Left panels: approximation errors. Right panels: required number of the exponential terms. The results are shown for solar zenith angles of 90° (upper panels) and 92° (lower panels) and wavelengths of 310 nm (black solid lines) and 600 nm (red dashed lines). (For interpretation of the references to color in this figure caption, the reader is referred to the web version of this article.)

approach has been implemented later for a non-limb observation geometry in the RT model LIDORT [128], where it is referred to as the enhanced pseudo-spherical model, and for a limb-viewing geometry in the RT model LIMTRAN [129].

The approximative spherical solution is obtained employing the formal solution of the VRTE, see Section 5.1 for details, and accounts for the Earth's curvature for both direct and scattered solar light. The solution is found by integrating the appropriate source functions along the line-of-sight intersecting a spherical shell atmosphere. This technique is also known as the Characteristics method [104]. The Stokes vector describing the radiation traveling in the direction Ω_v (see Fig. 5) is given then by

$$\mathbf{I}(\Omega_v) = \mathbf{I}(\Omega_0)e^{-\tau_s} + \int_0^{\tau_s} [\mathbf{J}_m(\tau'_s, \Omega_s) + \mathbf{J}_s(\tau'_s, \Omega_s) + \mathbf{J}_e(\tau'_s)]e^{-\tau'_s} d\tau'_s, \quad (59)$$

where $\mathbf{I}(\Omega_0)$ is the Stokes vector at the boundary (i.e. top or bottom) of the atmosphere in the direction Ω_0 (in the limb-viewing geometry $\mathbf{I}(\Omega_0) = 0$), \mathbf{J}_m , \mathbf{J}_s , and \mathbf{J}_e are the multiple scattering, single scattering, and internal emission source functions, respectively, τ'_s is the spherical optical depth along the line-of-sight, and Ω_s defines the local line-of-sight direction. Clearly, the Stokes vectors and source functions in Eq. (59), with exception of \mathbf{J}_e , depend on the solar zenith angle, Ω_s° , as well. However, for simplicity this dependence is not indicated. A viewing geometry typical for limb observations is illustrated in Fig. 5. The thick solid line **AD** denotes the line-of-sight, an arbitrary point along the line-of-sight is marked by **S**, τ'_s and τ_s are obtained by integrating the extinction coefficient along **AS** and **AD**, respectively, and the angles Ω_v , Ω_s , and Ω_0 are defined with respect to the local verticals shown by the dashed lines. Thus, for each point **S** at the line-of-sight, all angles as well as the light paths are calculated accounting for the sphericity of the atmosphere. Details on the angle transformation within a spherical medium can be found in [108].

At each point, **S**, along the line of sight, the single scattering source function, $\mathbf{J}_s(\tau'_s, \Omega_s)$, is calculated as

$$\mathbf{J}_s(\tau'_s, \Omega_s) = \frac{\omega(\tau'_s)}{4} \mathbf{Z}(\tau'_s, \Omega_s, \Omega_s^\circ) \mathbf{I}_1 e^{-\tau_s^\circ}, \quad (60)$$

where the single scattering albedo, $\omega(\tau'_s)$, solar zenith angle, Ω_s° , and phase matrix $\mathbf{Z}(\tau'_s, \Omega_s, \Omega_s^\circ)$ at the point **S** are used, and the spherical optical depth between the point **S** and the top of the atmosphere, τ_s° , is obtained by

integrating the extinction coefficient along the direct solar beam (**SC** in Fig. 5).

Generally, the multiple scattering source function, $\mathbf{J}_m(\tau'_s, \Omega_s)$, cannot be directly calculated according to its definition, see Eq. (15), because the diffuse component of the radiation field Stokes vector is unknown. In the framework of the approximative spherical approach implemented in SCIATRAN, the multiple scattering source function is calculated from the radiation field obtained from employing the pseudo-spherical approximation, see Section 5.8, at a set of solar zenith angles:

$$\mathbf{J}_m^{\text{ps}}(\tau'_s, \Omega_s, \Omega_s^\circ) = \frac{\omega(\tau'_s)}{4\pi} \int_{(\Omega)} \mathbf{Z}(\tau'_s, \Omega_s, \Omega') \mathbf{I}^{\text{ps}}(\tau'_s, \Omega', \Omega_s^\circ) d\Omega'. \quad (61)$$

Here, the argument Ω_s° explicitly shows that the pseudo-spherical radiation field, \mathbf{I}^{ps} , is obtained by solving the pseudo-spherical RTE for a solar zenith angle of Ω_s° .

Consequently the approximative spherical solution is written as

$$\mathbf{I}(\Omega_v) = \mathbf{I}(\Omega_0)e^{-\tau_s} + \int_0^{\tau_s} [\mathbf{J}_m^{\text{ps}}(\tau'_s, \Omega_s, \Omega_s^\circ) + \mathbf{J}_s(\tau'_s, \Omega_s) + \mathbf{J}_e(\tau'_s)]e^{-\tau'_s} d\tau'_s. \quad (62)$$

It follows that in the approximative spherical model the sphericity of the Earth's atmosphere is fully accounted for when performing the integration along the line-of-sight as well as when calculating the single scattering source function whereas the multiple scattering contribution is accounted for using an approximation. A discussion of the numerical aspects concerning the employed discretization scheme and interpolation technique is presented by Rozanov et al. [108,109,48].

For a spherical shell atmosphere, the single scattering albedo, $\omega(\tau'_s)$, used in Eqs. (60) and (61) to calculate the source functions is assumed to be a function of the altitude only. In the framework of the approximative spherical model, an additional extension can be easily introduced allowing the atmospheric properties to vary with the solar zenith angle. This is done considering the single scattering albedo to be a function of both the vertical coordinate and the solar zenith angle. In particular, this approach is used to account for a photochemical change in vertical distributions of atmospheric species. The impact of the photochemical change on simulated NO_2 slant columns has been investigated by Rozanov [108] while Mueller et al. [130] have compared BrO slant columns resulting from SCIATRAN simulations to those obtained from ground-based zenith sky measurements and from the space-borne instrument GOME. In the current version of SCIATRAN this extension is implemented only in the scalar mode.

5.10. Coupled ocean–atmosphere RT model

As discussed in Section 4.2.3, in a coupled ocean–atmosphere system the upper boundary condition for the ocean contains the contribution of the radiation traveling from the atmosphere to the ocean through the air–water interface (see Table 2) while the lower boundary condition for the atmosphere contains the radiation traveling from the ocean to the atmosphere. This means that the solution of the BVP in the atmosphere depends on the solution in

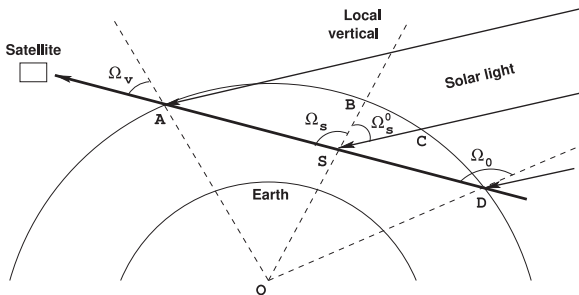


Fig. 5. Typical limb-viewing observation geometry.

the ocean and vice versa. Thus, either one needs to formulate a joint BVP describing both atmosphere and ocean by one system of RTE's or an iterative approach can be employed. When using the former method, the matrix related to the linear algebraic equation system which needs to be solved to obtain the required constants (see Section 5.3) becomes much larger because of a larger vertical extension of the joint medium and because of otherwise unnecessary quadrature points which need to be introduced for the atmosphere. The latter is necessary because the matrix dimensions for the joint system are determined by the number of Gaussian-quadrature points needed to describe the radiative transfer in the ocean, which is higher than the number for the atmosphere (see Section 5.2). As increased matrix dimensions result in a substantial slow-down of the solution process, the iterative approach has been preferred for the implementation in SCIATRAN. In the framework of this approach, the BVP for the atmosphere is solved first using an a priori estimation for the water-leaving radiation (term $I_w(0, \Omega')$ in Table 2) in the lower boundary condition. In this step, the water-leaving radiation can either be approximated (e. g. Gordon approximation [131]) or set to zero. Thereafter, the upper boundary condition for the ocean can be obtained as listed in Table 2. Subsequently, the BVP for the ocean is solved delivering an updated lower boundary condition for the atmosphere and the BVP for the atmosphere is then solved again. The iterative process is run until the convergence is reached both for the water-leaving radiation and for the radiation penetrating into the ocean. This means that differences between the results from two subsequent iterations are below a pre-selected threshold for both quantities.

The computational efficiency of the iterative approach in the framework of the discrete-ordinates technique is owed to the fact that both general solution of the homogeneous RTE and particular solutions of the inhomogeneous RTE need to be calculated only once for each medium (atmosphere and ocean). Furthermore, the matrix describing the linear equation system for the constants (see Section 5.3) does not change during the iterative process. Thus, for this matrix, the very time-consuming operation of the LU decomposition also needs to be done only once for each medium. It follows that at each iterative step only a linear algebraic system with a pre-factorized (LU decomposed) matrix needs to be solved, which is performed by means of the computationally efficient forward and backward substitution technique.

For a single scattering albedo typical for natural water (less than 0.5 at 415 nm), the above discussed iterative process converges typically after 3 iterations, where each iterative step comprises solving BVPs for both atmosphere and ocean. For single scattering albedo values higher than 0.9, which, however, are less realistic, the convergence slows down. The convergence rate for different combinations of atmospheric optical thickness and single scattering albedo within the ocean is presented in Table 3. The results are obtained for the following parameter settings:

- single scattering albedo: 0.9, 0.99, 0.995, 0.997, 1 for the ocean and 1 (conservative scattering) for the atmosphere;

Table 3

Number of iterations needed to satisfy convergence criteria of 0.1% for different combinations of atmospheric optical thickness τ_a and ocean single scattering albedo ω_w , assuming $\tau_w = 1000$ and $\omega_s = 1$. Each iterative step comprises solving BVPs for both atmosphere and ocean.

ω_w	τ_a			
	0.25	2.5	25	250
0.5	3	3	3	3
0.9	4	4	4	4
0.99	5	6	7	7
0.995	5	7	9	9
0.997	5	8	11	12
1	6	16	71	240

- optical depth: 1000 for the ocean and 0.25, 2.5, 25, 250 for the atmosphere;
- light scattering is determined by the Rayleigh scattering matrix in the atmosphere and by the Henyey–Greenstein phase function with the asymmetry factor $g=0.95$ in the ocean;
- refractive index: 1.0 in the atmosphere and 1.338 in the ocean;
- ocean bottom albedo: Lambertian, $A=1$.

It follows that even for an unrealistically small absorption within the ocean ($\omega_w=0.9$) four iterations are sufficient for all considered atmospheric optical thicknesses. The convergence rate decreases considerably in the case of conservative scattering in the ocean and an optically thick conservatively scattering atmosphere (last row and last column in Table 3). However, this scenario is unrealistic in nature and, thus, is of interest only for theoretical considerations.

6. Atmosphere

To obtain the numerical solution of the VRTE as discussed in the previous section, one needs to specify the optical characteristics of the atmosphere and either reflecting properties of the underlying surface for an uncoupled atmospheric problem or optical properties of the water for a coupled ocean–atmosphere system. In this section, we focus our discussion on optical characteristics of the atmosphere while underlying surface properties and optical characteristics of the water are discussed in the following sections.

The main processes determining the radiative transfer in the atmosphere are the absorption by gaseous species, molecular scattering, absorption and scattering by aerosol and cloud particles, and thermal emission. The related optical characteristics needed to solve the VRTE are the extinction and scattering coefficients, as well as phase functions or scattering matrices (scalar or vector case, respectively). To calculate these quantities, a database is needed which contains information on vertical distributions and spectral characteristics of gaseous absorbers, vertical profiles of the pressure and temperature, molecular scattering characteristics, as well as optical characteristics of aerosols and clouds. The database of atmospheric

parameters which is a part of the distributed SCIATRAN software package is discussed in detail below.

6.1. Gaseous absorbers, pressure, and temperature

The SCIATRAN software package incorporates a climatological database obtained from a 2D chemical transport model developed at the University of Bremen [132] which is similar to the well-known SLIMCAT model [133]. This database contains monthly and zonally averaged distributions of atmospheric trace gases which show significant absorption features in the UV–Vis–IR spectral range (O_3 , NO_2 , SO_2 , ClO , $HCHO$, BrO , NO_3 , $OCIO$, O_2 , H_2O , CO_2 , N_2O , CO , CH_4 , NO , NH_3 , HNO_3 , OH , HF , HCl , HBr , HI). Additionally, pressure and temperature information is contained. The data is provided in the altitude range 1–95 km for 10° latitude bins. Alternatively, a similar dataset obtained from a 2D chemical transport model developed at MPI Mainz [134] or a globally averaged US Standard model atmosphere [135] can be used. For ozone, several measurement based climatologies are also provided [136–138]. The database profiles of ozone and water vapor can be scaled to obtain desired columnar amounts while the pressure profile can be scaled to match a pre-defined surface pressure. In addition, user-defined vertical profiles can be provided for any absorber. This allows users to input their own information where available and use database contents everywhere else. Depending on the spectral range and required accuracy, absorption features of atmospheric trace gases can be accounted for in three different ways as discussed below.

In the UV–Vis spectral range, broadband absorption signatures showing rather slow spectral variations are typical for atmospheric trace gases. Most important in this spectral range are the Hartley, Huggins, and Chappuis absorption bands of ozone (shown by the green curve in Fig. 6). Most typically, the absorption cross sections in this spectral range depend moderately on the temperature and only weakly on the pressure. This allows one to use pre-convolved or moderate spectral resolution cross sections. The temperature dependence of the cross sections is accounted for either providing a set of cross sections measured at different temperatures [139–142] or using a parameterization [143,144]. Absorption cross sections of the following species are included in the SCIATRAN database: O_3 [143,139,141,145], NO_2 [140,139], SO_2 [146], ClO [147], $HCHO$ [148], BrO [142,149,150], NO_3 [151], $OCIO$ [152], O_4 [153], and O_2 [154,144,155]. The spectral resolution of the cross sections is 0.24–0.54 nm depending on the spectral region.

In the NIR–TIR spectral range, sharp spectral signatures owing to the molecular absorption or emission dominate in the observed spectra of the scattered, transmitted, or emitted radiation. These spectral features exhibit a strong dependence on the pressure and temperature. The most accurate way to consider these signatures is to perform the so-called line-by-line calculations. This method implies radiative transfer calculations with a very high spectral sampling. At each wavelength, contributions from all relevant spectral lines of all considered species need to be summed up. The information on the line positions, intensities, and further parameters needed to calculate

these contributions are provided by the HITRAN (High-resolution TRANsmision) database [156]. In the SCIATRAN model, absorption features of the following molecules can be calculated using the HITRAN database: O_3 , NO_2 , SO_2 , ClO , $HCHO$, O_2 , H_2O , CO_2 , N_2O , CO , CH_4 , NO , NH_3 , HNO_3 , OH , HF , HCl , HBr , HI .

As mentioned above, a sufficient accuracy of line-by-line calculations can only be achieved when calculating at a high spectral sampling, which makes this approach quite time consuming. For many practical applications, however, simulated spectra with only a moderate spectral resolution are needed. This means that the simulated radiance needs to be convolved with an instrument slit function. Thus, using this approach, resulting moderate resolution spectra are typically highly oversampled. A significant speed-up can be achieved when calculating integral signals for pre-defined spectral intervals rather than modeling at a highly sampled spectral grid. In the SCIATRAN model, this is done taking advantage of the so-called correlated-k approximation [157]. The ESFT (exponential-sum fitting of transmissions) coefficients employed in the framework of this approximation are pre-calculated in accordance with the spectral sampling and resolution of the SCIAMACHY instrument [158,83,159] using the HITRAN database [156]. The SCIATRAN database provides ESFT coefficients for the following spectral intervals and samplings: 0.394–1.07 μm (0.05 nm), 1.07–1.8 μm (0.2 nm), 1.92–2.06 μm (0.025 nm), 3.5 nm–40 μm (0.1 μm).

Vertical optical thicknesses of major absorption species included in the SCIATRAN database are shown in Figs. 6 and 7. In the UV–Vis–NIR spectral range (Fig. 6) the calculations are done with a spectral resolution of 0.24 nm and a sampling of 0.1 nm while in the NIR–TIR spectral range (Fig. 7) a spectral resolution of 2 nm and a sampling of 1 nm are used.

6.2. Rayleigh scattering

Light scattering by particles which are much smaller than the wavelength of the light is usually referred to as the Rayleigh scattering. In the Earth's atmosphere this is the scattering by the air molecules. Similar to other scattering processes discussed in the course of this study, the Rayleigh scattering is characterized by the scattering coefficient, which describes the fraction of light scattered in the atmosphere per unit distance, and by the scattering matrix, which determines the angular distribution of the scattered light.

Following Mishchenko et al. [91], the Rayleigh scattering matrix can be written as

$$F(\gamma) = \frac{3d}{4} \begin{bmatrix} (1 + \cos^2 \gamma) & -\sin^2 \gamma & 0 & 0 \\ -\sin^2 \gamma & (1 + \cos^2 \gamma) & 0 & 0 \\ 0 & 0 & 2 \cos \gamma & 0 \\ 0 & 0 & 0 & 2d' \cos \gamma \end{bmatrix} + \mathbf{D}, \quad (63)$$

where

$$d = \frac{1-\delta}{1+\delta/2}, \quad d' = \frac{1-2\delta}{1-\delta}, \quad (64)$$

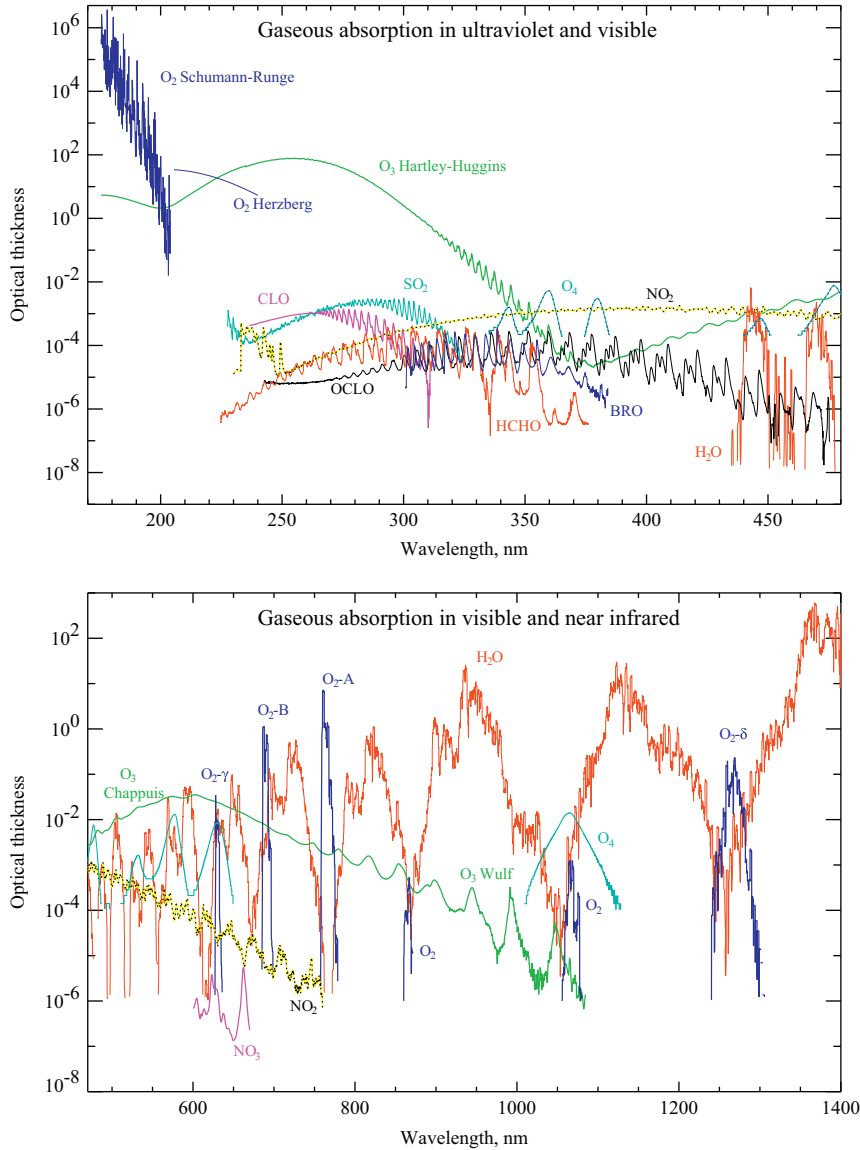


Fig. 6. Vertical optical thicknesses of main gaseous absorbers in UV-Vis (upper panel) and Vis-NIR (lower panel) spectral ranges. (For interpretation of the references to color in this figure caption, the reader is referred to the web version of this article.)

the depolarization factor, δ , accounts for the anisotropy of molecules, and the 4×4 matrix \mathbf{D} contains only one non-zero element, $D_{11} = 1 - d$. The depolarization factor shows only a weak dependence on the wavelength ranging from 0.031 to 0.027 between 300 and 800 nm (see e.g. [160]). The SCIATRAN model allows the usage of both, a constant and wavelength dependent depolarization factor.

The Rayleigh scattering coefficient is obtained as a product of the Rayleigh scattering cross section, $\sigma_{ray}(\lambda)$, and the molecular number density, N . As discussed, e.g., by van de Hulst [92], the most common expression for the Rayleigh scattering cross section at a wavelength λ is given by

$$\sigma_{ray}(\lambda) = \frac{24\pi^3}{N^2 \lambda^4} \left[\frac{n^2(\lambda) - 1}{n^2(\lambda) + 2} \right]^2 F(\lambda), \quad (65)$$

where $n(\lambda)$ is the refractive index of air and $F(\lambda) = (6 + 3\delta)/(6 - 7\delta)$ is the depolarization term also referred to as the King factor. It is worth noting here that according to the Lorentz–Lorenz relation, the term in the square brackets (often referred to as the Lorentz–Lorenz factor) is proportional to the air density, N . Thus, N^2 in the denominator cancels out ensuring the expected independence of the Rayleigh scattering cross section from the molecular number density. As the refractive index of the air is close to unity, the following approximative expression for the Lorentz–Lorenz factor is appropriate:

$$\frac{n^2(\lambda) - 1}{n^2(\lambda) + 2} \approx \frac{2}{3} [n(\lambda) - 1]. \quad (66)$$

Although the relationship provided by Eq. (65) looks quite simple, there is no exact analytical representation for

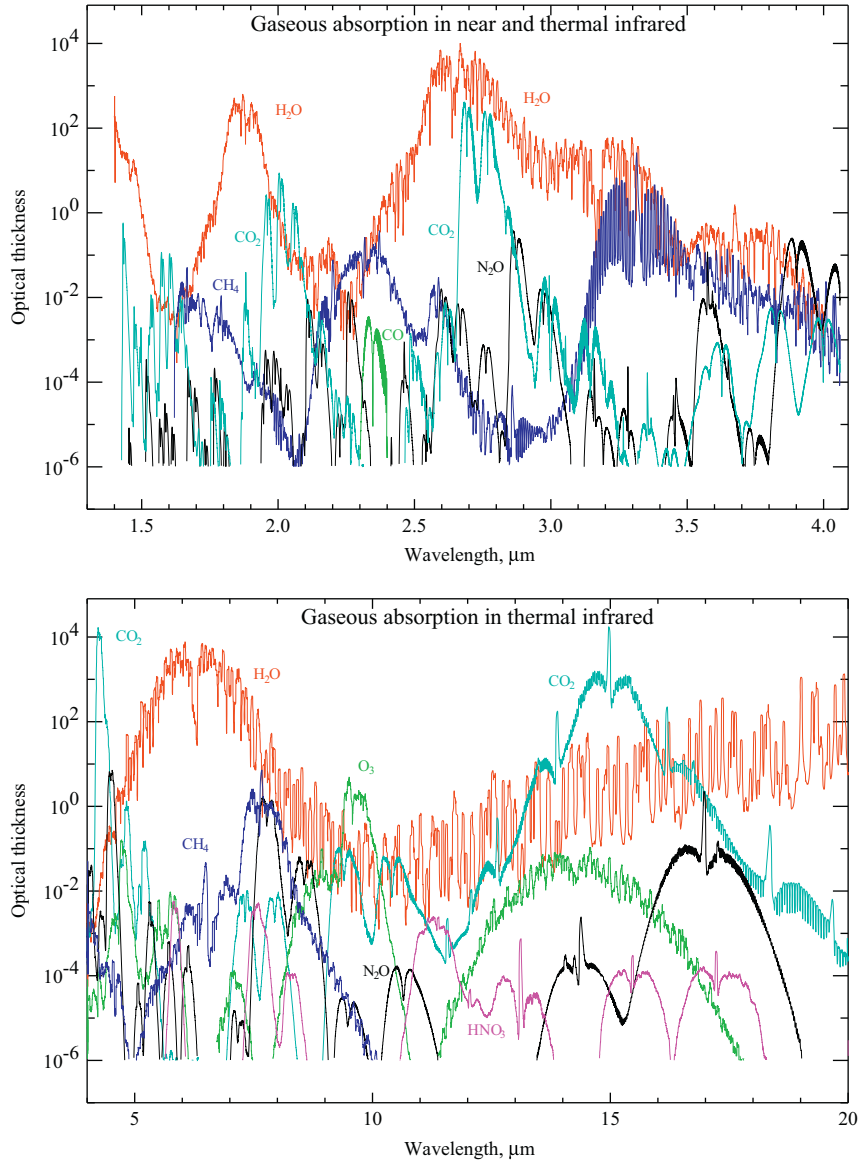


Fig. 7. Same as in Fig. 6 but in NIR–TIR (upper panel) and TIR (lower panel) spectral ranges.

the wavelength dependence of both the King factor and the refractive index of the air. For this reason, several commonly used approximations [160–162] are implemented in the SCIATRAN model. A detailed description of these approximations is presented below.

6.2.1. Modified Bates approximation

According to Bates [160], the Rayleigh scattering cross section is represented by a sum of contributions due to the main atmospheric constituents, and the wavelength dependencies of the Lorentz–Lorenz and King factors are approximated for each component independently. In the SCIATRAN model, contributions by four atmospheric constituents are considered, namely, nitrogen (N₂), oxygen (O₂), argon (Ar), and carbon dioxide (CO₂). Taking into account Eq. (66), the Rayleigh scattering coefficient as given by Eq. (65) is then

represented as

$$\sigma_{\text{ray}}(\lambda) = \frac{32\pi^3}{3N^2\lambda^4} \sum_k C_k [n_k(\lambda) - 1]^2 F_k(\lambda), \quad (67)$$

where k runs over all considered atmospheric constituents whose fractional volume abundances are denoted by C_k . Following Bodhaine [162], the latter are set to 78.084, 20.946, 0.934, 0.036 for N₂, O₂, Ar, and CO₂, respectively.

The wavelength dependence of the O₂ refractive index is approximated as suggested by Bates [160]:

$$[n_{\text{O}_2}(\lambda) - 1] \times 10^8 = A_{\text{O}_2} + \frac{B_{\text{O}_2}}{40.9 - \lambda^{-2}}, \quad (68)$$

where λ is the wavelength in μm. The coefficients A_{O_2} and B_{O_2} for different wavelength intervals are listed in Table 4. For the refractive index of N₂, the wavelength dependence parameterization suggested by Bates [160] has been

Table 4

Coefficients of the wavelength dependence parameterization for refractive indexes of O₂ and N₂ at 15 °C and 1013.25 hPa.

Molecule	A	B	Spectral range, μm
O ₂	23 796.7	168 988.4	$\lambda < 0.221$
	22 120.4	203 187.6	$0.221 < \lambda < 0.288$
	20 564.8	248 089.9	$0.288 < \lambda < 0.546$
	21 351.1	218 567.0	$0.546 < \lambda$
N ₂	6998.749	3 233 582.0	$\lambda < 0.254$
	5989.242	3 363 266.3	$0.254 < \lambda < 0.468$
	6855.200	3 243 157.0	$0.468 < \lambda < 2.06$

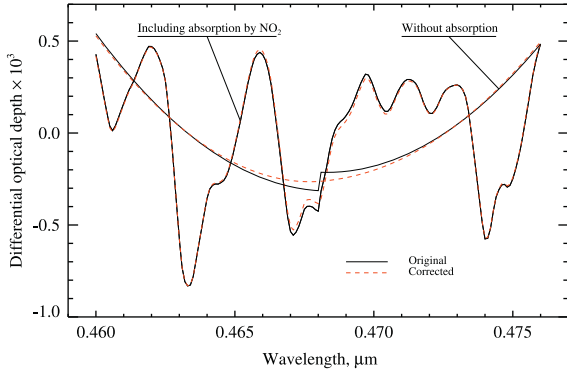


Fig. 8. Differential optical depth calculated using the corrected (red dashed line) and uncorrected (black solid line) refractive index. Calculations are done for the nadir observation geometry at a solar zenith angle of 25°. (For interpretation of the references to color in this figure caption, the reader is referred to the web version of this article.)

modified to remove a discontinuity at 0.468 μm, which results from an imperfect match of the parameterizations used above and below this wavelength. The resulting approximation employed in SCIATRAN is written as

$$[n_{N_2}(\lambda) - 1] \times 10^8 = A_{N_2} + \frac{B_{N_2}}{144 - \lambda^{-2}} + D_{N_2} \frac{\Delta_\lambda}{|\Delta_\lambda|} \exp\left(-\frac{|\Delta_\lambda|}{0.003}\right), \quad (69)$$

where λ is the wavelength in μm, $\Delta_\lambda = 0.468 - \lambda$, and $D = 2.27684009$. Similar to the refractive index of O₂, the coefficients A_{N_2} and B_{N_2} for different wavelength intervals are listed in Table 4. The first two terms on the right hand side of Eq. (69) are from the original Bates work and the third term provides a correction for the discontinuity. Fig. 8 shows the impact of the correction term on the spectral behavior of the differential optical depth (DOD) between 0.46 and 0.475 μm. The DOD is calculated from the modeled outgoing radiance at the top of the atmosphere, $I(\lambda)$, as follows:

$$\text{DOD}(\lambda) = \ln I(\lambda) - P(\lambda), \quad (70)$$

where $P(\lambda)$ denotes a second order polynomial.

Following Bodhaine et al. [162], the wavelength dependencies of the refractive indexes of Ar and CO₂ in the SCIATRAN model are implemented according to Dalgarno [163] and Owens [164], respectively:

$$[n_{Ar}^2(\lambda) - 1] \times 10^8 = 5.547 \times 10^4 [1 + 5.15 \times 10^{-3} \lambda^{-2} + 4.19 \times 10^{-5} \lambda^{-4}], \quad (71)$$

$$[n_{CO_2}(\lambda) - 1] \times 10^8 = 22822.1 + 117.8 \lambda^{-2} + \frac{2406030}{130 - \lambda^{-2}} + \frac{15997}{38.9 - \lambda^{-2}}, \quad (72)$$

where λ is the wavelength in μm. Note that in contrast to other atmospheric constituents, the approximation for Ar is given for $n^2(\lambda) - 1$ rather than for $n(\lambda) - 1$.

It should be pointed out that all approximations discussed above, see Eqs. (68)–(72), have been obtained for standard conditions (15 °C, 1013.25 hPa). In the SCIATRAN model, the dependence of the refractive indexes on the temperature and pressure is accounted for as discussed by Birch and Downs [165]:

$$n(\lambda) - 1 = [n_s(\lambda) - 1] \frac{P[1 + P(60.1 - 0.972t) \times 10^{-10}]}{96095.43(1 + 0.003661t)}. \quad (73)$$

Here, t is the temperature in °C, P is the pressure in Pa, and $n_s(\lambda)$ is the refractive index at standard conditions.

The wavelength dependence of the King factors is approximated according to Bates [160] as follows:

$$F_{N_2}(\lambda) = 1.034 + 3.17 \times 10^{-4} \lambda^{-2}, \quad (74)$$

$$F_{O_2}(\lambda) = 1.096 + 1.385 \times 10^{-3} \lambda^{-2} + 1.448 \times 10^{-4} \lambda^{-4}, \quad (75)$$

$$F_{Ar}(\lambda) = 1.00, \quad (76)$$

$$F_{CO_2}(\lambda) = 1.15. \quad (77)$$

As above, λ denotes the wavelength in μm.

Our investigations show that the air refractive index calculated as discussed above agrees with the results presented in [166–168] within 0.2% in the entire spectral range covered by the SCIATRAN model.

6.2.2. Bucholtz approximation

Unlike the Bates approach, Bucholtz [161] has suggested a parameterization for the Rayleigh cross sections which does not require any splitting into components. The approximation has been obtained by a least-squares fit of the Rayleigh cross section data pre-calculated in two spectral ranges. The latter has been done in accordance with Eq. (65) using the parameterization for the air refractive index as suggested by Peek and Reeder [168] and the effective King factor proposed by Bates [160]:

$$F_{\text{eff}}(\lambda) = \frac{\sum_k C_k [n_k(\lambda) - 1]^2 F_k(\lambda)}{[\sum_k C_k (n_k(\lambda) - 1)]^2}. \quad (78)$$

The resulting approximation for the Rayleigh scattering cross section is written as

$$\sigma_{\text{ray}}(\lambda) = A \lambda^{-(B+C\lambda+D\lambda^{-1})}, \quad (79)$$

where λ is the wavelength in μm. The coefficients A , B , C , and D for two spectral ranges are listed in Table 5.

As reported by Bucholtz [161], the resulting approximation accuracy is within 0.4% for wavelengths less than 0.25 μm, better than 0.2% in the 0.25–0.5 μm range, and better than 0.1% for wavelengths greater than 0.5 μm. It should be noted, however, that the pre-calculated Rayleigh cross section database in Bucholtz' study ranges from 0.2 to 4 μm and the fit accuracy for wavelengths

Table 5

Coefficients of the wavelength dependence parameterization for the Rayleigh scattering cross section according to Bucholtz (for 15 °C and 1013.25 hPa).

λ , μm	A	B	C	D
0.2–0.5	3.01577×10^{-28}	3.55212	1.35579	0.11563
> 0.5	4.01061×10^{-28}	3.99668	1.0298×10^{-3}	2.71393×10^{-2}

outside this interval might substantially differ from the estimations above.

6.2.3. Bodhaine approximation

Similar to the Bucholtz approach discussed in the previous section, the approximation suggested by Bodhaine et al. [162] parameterizes the wavelength dependence of the Rayleigh scattering cross section:

$$\sigma_{\text{ray}}(\lambda) = \frac{1.0455996 - 341.29061\lambda^{-2} - 0.9023085\lambda^2}{1 + 0.0027059889\lambda^{-2} - 85.968563\lambda^2} 10^{-28}, \quad (80)$$

where λ is the wavelength in μm .

This parameterization has been obtained in a similar manner as the one by Bucholtz (see Section 6.2.2). First, the Rayleigh scattering cross section has been calculated in accordance with Eq. (65) for the 0.25–1 μm spectral range. The refractive index of the air has been approximated in accordance with Peek and Reeder's [168] formula which has additionally been corrected for a higher CO_2 concentration (360 ppm instead of 300 ppm in the original formula). The King factor of the air has been calculated accounting for contributions due to N_2 , O_2 , Ar, and CO_2 (the so-called weighted King factor):

$$F_w(\lambda) = \sum_K C_k F_k(\lambda) / \sum_K C_k, \quad (81)$$

where K runs over all the above-mentioned atmospheric constituents. The calculations have been done using the King factors for atmospheric species, $F_k(\lambda)$, as provided by Bates [160], see also Eqs. (74)–(77), and fractional volume abundances, C_k , of 78.084, 20.946, 0.934, and 0.036 for N_2 , O_2 , Ar, and CO_2 , respectively. The obtained Rayleigh scattering cross section data has then been fitted to obtain the approximation coefficients in Eq. (80).

As reported by Bodhaine et al. [162], the resulting approximation is accurate to better than 0.002% between 250 and 550 nm, better than 0.01% between 550 and 850 nm, and still better than 0.05% up to 1000 nm. It is worth noting that the pre-calculated Rayleigh cross section database in the Bodhaine et al. study ranges from 250 to 1000 nm and the fit accuracy for wavelengths outside this interval is initially unpredictable. Our estimations show that the approximation error increases with the wavelength from 0.2% at 1.2 μm to about 3% at 2 μm and reaches 19% at 3 μm .

6.2.4. User-defined mode

In the framework of the SCIATRAN model, experienced users can select the so-called “user defined” mode to calculate the Rayleigh scattering cross section. This is a flexible approach allowing one to combine approximations

published by different authors. In particular, either the exact representation or an approximation for the Lorentz–Lorenz factor can be chosen:

$$\frac{n^2(\lambda)-1}{n^2(\lambda)+2} \approx \frac{1}{3} [n^2(\lambda)-1] \approx \frac{2}{3} [n(\lambda)-1]. \quad (82)$$

Furthermore, one of the pre-defined wavelength parameterizations for the refractive index of air can be used. Here, the formula proposed by Peck and Reeder [168], old and new formulas suggested by Edlen [166,167], as well as the Bates approach [160] are available. The latter approach requires fractional volume abundances for main atmospheric constituents (N_2 , O_2 , Ar, and CO_2) to be specified in the input file while the former three formulas are scaled to the fractional volume abundance of CO_2 specified by the user. The King factor can be calculated either from the depolarization factor specified by the user (constant or wavelength dependent) or by employing one of the two pre-defined approximations, namely the effective or weighted King factor according to Eq. (78) or (81), respectively.

6.3. Atmospheric aerosol

Light scattering by aerosols is described by the extinction and scattering coefficients as well as by the scattering matrix. Similar to the Rayleigh scattering, the extinction and scattering coefficients are represented by the products of the aerosol number density and the corresponding cross sections. The extinction and scattering cross sections together with the scattering matrix are often referred to as the optical characteristics of the aerosol. The scattering matrix is commonly represented by the Greek constants (Legendre expansion coefficients in the scalar case) which are obtained using the Mie theory, see e.g. [169,97,170] and references therein. Here, a spherical shape of the aerosol particles is assumed and both a particle size distribution and a refractive index for each aerosol type need to be specified.

In the SCIATRAN model, the so-called aerosol layer concept is employed, i.e. the vertical distribution of the aerosol is described by a number of aerosol layers. Within each layer, which is defined by its top and bottom altitudes, the optical characteristics of the aerosol are assumed not to change while the aerosol number density may vary. The aerosol characteristics can be either read from the internal database (as described below) or specified by the user in the input file. In the latter case, which is referred to as the user-defined mode, the user needs to provide profiles of the aerosol extinction and scattering coefficients as well as the scattering matrix for each aerosol layer at a desired number of wavelengths.

The internal aerosol database of SCIATRAN is calculated using the `spher.f` code developed by Mishchenko et al. [171], which is publicly available at <http://www.giss.nasa.gov/staff/mmishchenko/brf/>. The code is intended to provide Legendre expansion coefficients or Greek constants for polydisperse spherical particles using the standard Lorenz–Mie theory. Non-spherical or inhomogeneous particles cannot be accounted for.

The most generally applicable aerosol parameterization provided by SCIATRAN is the so-called WMO database. It can be used in the entire spectral range covered by the SCIATRAN model for both scalar and vector radiative transfer calculations. The WMO database is compiled in accordance with World Meteorological Organization (WMO) recommendations [172] on particle size distributions and spectral refractive indexes for six basic components of the atmospheric aerosol. These are the water soluble, dust, oceanic, soot, stratospheric, and volcanic aerosols. The size distributions for both stratospheric and volcanic aerosols are assumed to be described by the modified gamma distribution:

$$f_{\text{mg}}(r) = \frac{rsb^{2/s}}{\Gamma(2/s)} \exp(-br^s) \quad (83)$$

while for other aerosol components, particles are assumed to be distributed in accordance with the lognormal law, see e.g. Davies [173]:

$$f_{\text{ln}}(r) = \frac{1}{r|s|\sqrt{2\pi}} \exp\left[-\frac{(\ln r - b)^2}{2s^2}\right]. \quad (84)$$

In both equations, r is the particle radius in μm . The particle size distribution parameters s and b for each aerosol component are listed in Table 6. For numerical reasons, concentration of particles smaller than $0.005 \mu\text{m}$ and larger than $20 \mu\text{m}$ is assumed to be zero.

The parameterizations for commonly used aerosol types such as continental, maritime, and urban aerosols are obtained by an appropriate mixing of the optical properties of the basic aerosol components:

$$k_e(\lambda, z) = N(z) \sum_j p_j \sigma_{e,j}(\lambda), \quad k_s(\lambda, z) = N(z) \sum_j p_j \sigma_{s,j}(\lambda), \quad (85)$$

$$F_{\lambda}(\gamma) = \sum_j p_j F_{j,\lambda}(\gamma) \sigma_{s,j}(\lambda) / \sum_j p_j \sigma_{s,j}(\lambda), \quad (86)$$

where $N(z)$ is the aerosol particle number density, k_e/k_s is the extinction/scattering coefficient, $\sigma_{e,j}/\sigma_{s,j}$ is the extinction/scattering cross section, $F_{j,\lambda}(\gamma)$ is the scattering matrix, and p_j is the fractional abundance of the “ j ”-th aerosol component. The summation runs over all considered aerosol components. Within each aerosol layer, the aerosol composition and the scattering matrix do not change while the particle number density might depend on the altitude. For commonly used aerosol types, the fractional

abundances of the basic aerosol components recommended by WMO [172] are listed in Table 7. In the SCIATRAN model, the fractional abundances are specified in the input file and can be adjusted by users according to their needs. The extinction and scattering cross sections as well as the scattering matrix are stored in the SCIATRAN database at 61 wavelengths. The aerosol number density is calculated from the aerosol extinction coefficient profile provided by the user. The profile can be provided at any wavelength in the spectral range covered by the SCIATRAN model.

In addition to the WMO parameterization, the widely used LOWTRAN 7 [60] and SCIATRAN [174] aerosol databases are incorporated in the SCIATRAN software package. Both databases are suitable only for scalar (unpolarized) radiative transfer calculations.

The SCIATRAN aerosol parameterization contains information about a variety of the aerosol basic components adapted from the database compiled by Koepke and Hess [175]. The resulting aerosol characteristics are calculated by summing up contributions from different aerosol components according to Eqs. (85) and (86). The aerosol number density is either provided by the user or calculated from the aerosol extinction coefficient profile. In the latter case, the extinction coefficient profile needs to be provided by the user at any wavelength in the spectral range covered by the SCIATRAN model. The SCIATRAN parameterization covers the spectral range from 225 nm to $2.5 \mu\text{m}$. The number of stored Legendre expansion coefficients of the scattering phase functions is limited to 50 which makes this parameterization suboptimal for strongly elongated phase functions.

The LOWTRAN 7 database contains parameterizations for several pre-defined aerosol compositions. In the lower atmosphere, the aerosol properties can be adjusted according to the humidity and visibility parameters selected by the user. In the stratosphere, aerosol parameterizations corresponding to background atmosphere or several levels of volcanic activity can be selected. The pre-defined parameterizations contain both the phase function and scattering/extinction coefficient. Neither the aerosol composition nor the number density can be changed independently. For the scattering phase function only the Henyey–Greenstein

Table 7

Fractional abundances of the basic aerosol components for different aerosol types according to the WMO aerosol parameterization implemented in SCIATRAN.

Type	Water soluble	Dust	Oceanic	Soot
Continental	0.93877	2.27×10^{-6}	0	0.061230
Maritime	0.99958	0	0.00042	0
Urban	0.59450	1.66×10^{-7}	0	0.40550

Table 6

Particle size distribution parameters for the aerosol components according to the WMO aerosol parameterization implemented in SCIATRAN.

Parameter	Stratospheric	Volcanic	Water soluble	Dust	Oceanic	Soot
b	18	16	−5.298	−0.6932	−1.204	−4.44
s	1	0.5	0.08948	0.08948	−0.08219	−0.3666

analytical model (see e.g. [7]) is available. The LOWTRAN 7 database covers the spectral range from 200 nm to 6 μm .

For the stratospheric aerosols, the extinction coefficient can be set in accordance with the ECSTRA (Extinction Coefficient for STRatospheric Aerosol) model, which has been developed by Fussen and Bingen [176] based on the SAGE II measurements from October 1984 to December 1995. The database covers the spectral range from 335 nm to 1.02 μm providing the aerosol extinction coefficient as a function of the latitude and of the volcanic activity parameter.

Independent of the input method, the aerosol extinction and scattering coefficients can be scaled to a desired value of the aerosol optical thickness, $\tau(\lambda_r)$, which can be specified by the user at any wavelength, λ_r , within the spectral range covered by the SCIATRAN model. In this case vertical profiles of both the scattering and the extinction coefficients are multiplied at all wavelengths by a constant factor which is obtained as follows:

$$C = \frac{\tau(\lambda_r)}{\int_{z_0}^{z_{\max}} k_e(\lambda_r, z) dz}, \quad (87)$$

where the integration is performed from the surface to the top of the atmosphere.

6.4. Clouds

Generally, clouds in the Earth's atmosphere consist of water droplets and/or ice crystals whose scattering properties can be described in the same way as for the aerosols. The fact that the refractive indexes of both the liquid water and ice are well known makes the cloud parameterization even a bit easier as compared to the aerosols. In SCIATRAN, clouds are defined as layers whose lower and upper boundaries need to be specified by the user. The optical characteristics of each cloud layer (extinction and scattering cross sections as well as the scattering matrix) can be either read from the internal database of SCIATRAN or specified by the user in the input file. Internal databases for water and ice clouds available in the SCIATRAN model can also be combined to parameterize mixed clouds.

In the user-defined mode an additional absorber within a cloud layer (e.g. soot) can be introduced. For this absorber, both real and imaginary parts of the refractive index as functions of wavelength as well as a number density profile need to be specified. This capability of SCIATRAN allows the user to model for example the impact of impurities on the spectral reflection properties of a snow layer, see Section 7.2 for details.

6.4.1. Water cloud database

The water cloud database contains the scattering and extinction cross sections as well as scattering matrices calculated by employing the Mie theory [97,171]. The calculations are done at 451 spectral points between 0.2 and 40 μm using the refractive index of pure water proposed by Segelstein [177]. Following Deirmendjian [97] the water droplet size distribution is assumed to be

described by the gamma distribution:

$$f(r) = \left(\frac{\eta}{r_m}\right)^{\eta+1} \frac{r^\eta}{\Gamma(\eta+1)} \exp\left(-\eta \frac{r}{r_m}\right), \quad (88)$$

where r_m is the mode radius, η is the half-width parameter, and $\Gamma(\eta+1)$ is the gamma function. The mode radius is related to the effective radius r_{eff} which is defined as

$$r_{\text{eff}} = 3 \frac{\bar{V}}{\bar{S}}, \quad (89)$$

where \bar{V} is the average volume and \bar{S} is the average surface area of the particles. For the water droplet size distribution given by Eq. (88), it follows:

$$r_{\text{eff}} = r_m \left(1 + \frac{3}{\eta}\right), \quad (90)$$

see [178] for details. As discussed by Kokhanovsky [178] a value of 6 for the half-width parameter η provides optimal representation for continental and marine clouds. In particular, the frequently used cloud model C1 of Deirmendjian [97] is obtained with $r_{\text{eff}} = 6 \mu\text{m}$ and $\eta = 6$.

The SCIATRAN database contains optical characteristics of water clouds calculated for $\eta = 6$ and effective radii of water droplets between 4 and 20 μm in steps of 2 μm .

6.4.2. Ice cloud database

Optical characteristics of ice clouds are calculated in the framework of the geometrical optics approximation using the ray tracing Monte-Carlo code [179]. The cloud particles are assumed to be randomly oriented. The extinction coefficient is given by $k_e = N \cdot \bar{S}/2$, where N is the particle number density related to the volumetric concentration of particles, C_v , via the following relationship: $N = C_v/\bar{V}$. The data of Warren and Brandt [180] for the ice refractive index is used. The calculations are done at 73 wavelengths between 0.2 and 40 μm representing ice crystals as either fractal particles [179] or hexagonal prisms. In the latter case, the cloud optical characteristics are calculated only for the hexagonal prism heights of 100 μm and side lengths of 12.5, 25, and 50 μm . The results are averaged with respect to the particle orientation while no averaging with respect to the prism heights and/or lengths is performed.

The fractal particle model uses regular tetrahedrons with a side length L as its basic elements. The second generation fractals considered in this study are obtained as follows. First, to each side surface of any tetrahedral element another element of the same size and shape is attached forming the first generation fractal. Then, yet another tetrahedral element is attached to each side surface of this fractal forming the second generation fractal. For the resulting fractal particle a roughness is introduced. The results are averaged with respect to the particle orientation. An averaging with respect to the tetrahedron side length, L , is not performed. The cloud optical characteristics are calculated for tetrahedron side lengths of 50, 100, and 300 μm , which corresponds to effective radii of 23, 46, and 142 μm , respectively. The geometrical cross sections ($S_g = S/4$) of the resulting fractal particles are 1652, 6599, and 63 283 μm^2 , respectively.

The elements of the scattering matrices calculated for ice crystals (hexagonal prisms and fractal particles) and water droplets (polydisperse spherical particles) are shown in Fig. 9. The calculations are done at a wavelength of 550 nm. As expected, the phase function (F_{11} element) corresponding to hexagonal prisms shows a backscattering peak as well as both primary and secondary halos at scattering angles of $\sim 22^\circ$ and $\sim 46^\circ$, respectively. The phase function of water droplets displays the primary and secondary rainbows at scattering angles of $\sim 140^\circ$ and $\sim 125^\circ$, respectively. A detailed discussion of scattering patterns from the viewpoint of the electromagnetic scattering theory is presented among others by Mishchenko et al. [90].

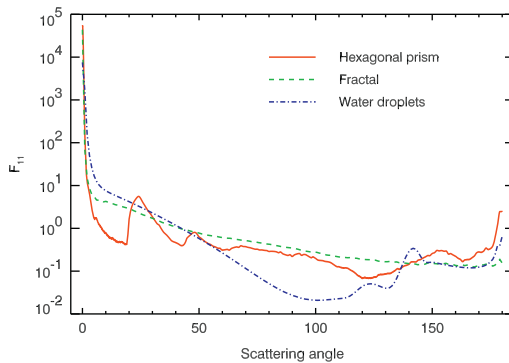
It should be noted here that due to its limits of validity the geometrical optics approximation might result in significant errors when the particle size is comparable to the wavelength of the incident light (e.g. in the thermal infrared region).

6.4.3. Vertical inhomogeneity of cloud optical characteristics

Within each cloud layer the SCIATRAN model offers the possibility to introduce a vertical inhomogeneity of cloud optical characteristics. The vertical coordinate within a cloud is defined by employing the concept of the dimensionless “altitude” as suggested by Feigelson [181], i.e. it is introduced as $x = (h_t - z)/(h_t - h_b)$, where h_t and h_b are the cloud top and bottom heights, respectively. The user needs to specify the size and amount of the cloud particles as functions of the vertical coordinate x , which ranges from 0 to 1. The particle size is defined by the effective radius for water droplets (see Eq. (89)) and by the side length for ice crystals. This parameter is used then to obtain the extinction/scattering cross section and the scattering matrix by interpolating between the database entries. The amount of the cloud particles can be defined alternatively by (i) the number density of water droplets and/or ice crystals in absolute units, (ii) the liquid and/or ice water contents (LWC and/or IWC, respectively) in absolute units, (iii) the shape of the LWC and/or IWC profile, (iv) the shape of the extinction coefficient profile.

From the given shape profile, the vertical distributions of LWC and IWC are obtained as follows:

$$C(z) = P \frac{s(z)}{\int_{h_b}^{h_t} s(z) dz}, \quad (91)$$



where $C(z)$ represents either the LWC or IWC vertical profile whose shape is denoted by $s(z)$ and the integral parameter P denotes either the liquid water path (LWP) or the ice water path (IWP), respectively. The LWP/IWP integral parameters need to be specified by the user in addition to the profile shapes.

The number density profiles are obtained from the LWC and/or IWC profiles using the following relationship: $N(z) = C(z)/\bar{V}(z)/\rho$, where $C(z)$ represents the vertical profile of either LWC or IWC, $\bar{V}(z)$ is the average volume of a particle, and ρ is the density of water or ice, respectively.

If the amount of cloud particles is defined by the shape of the extinction coefficient profile, the cloud optical thickness, $\tau(\lambda_r)$, at a reference wavelength, λ_r , is required as an additional input parameter. The particle number density profile is calculated then as follows:

$$N_p(z) = \frac{\tau(\lambda_r)}{\int_{h_b}^{h_t} s(z) \sigma_e(\lambda_r) dz} s(z), \quad (92)$$

where $\sigma_e(\lambda_r)$ is the extinction cross section at the wavelength λ_r and $s(z)$ is the shape of the extinction coefficient profile.

Most commonly, the extinction/scattering coefficient is calculated by multiplying the corresponding cross section by the particle number density. Alternatively, it can be obtained directly from the particle size parameter and LWC/IWC profiles employing simple analytical expressions as discussed by Kokhanovsky [178,182].

7. Surface reflection

The intensity and spectral behavior of the diffuse radiation in the terrestrial atmosphere are strongly affected by the reflecting properties of the underlying surface. The most straightforward quantitative characteristic of this reflecting properties is given by the surface albedo, which is most commonly defined as the ratio of the upwelling to the downwelling fluxes. In the visible spectral range, albedo of a land surface is usually about 0.1 depending on the vegetation state, soil type and moisture content. The albedo of the ocean ranges between 0.05 and 0.15 depending on the wind speed. For a snow covered

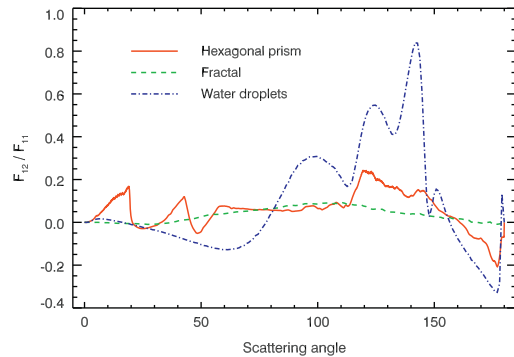


Fig. 9. Scattering matrix elements of ice crystals (hexagonal prisms and fractal particles) and water droplets (polydisperse spherical particles). The calculations are done at a wavelength of 550 nm for the hexagonal prism height and side length of 100 μm and 25 μm , respectively, tetrahedron side length of 100 μm , and a water droplet effective radius of 10 μm .

surface it might vary from 0.5 to 0.9 depending on the snow age and illumination angle [183].

In the most general case, the relationship between the radiation incident on the surface and the reflected radiation is given by

$$\mathbf{I}(\tau_0, -\mu, \varphi) = \frac{1}{\pi} \int_0^{2\pi} \int_0^1 \mathbf{R}(-\mu, \varphi, \mu', \varphi') \mathbf{I}(\tau_0, \mu', \varphi') \mu' d\mu' d\varphi', \quad (93)$$

where $\mu \in (0, 1]$, $\mathbf{I}(\tau_0, \mu', \varphi')$ and $\mathbf{I}(\tau_0, -\mu, \varphi)$ denote the Stokes vectors of the incident and reflected radiation, respectively, and $\mathbf{R}(-\mu, \varphi, \mu', \varphi')$ is referred to as the Bidirectional Reflectance Distribution Function (BRDF). In the case of a Lambertian reflection, Eq. (93) simplifies to

$$\mathbf{I}(\tau_0, -\mu, \varphi) = \frac{A}{\pi} \int_0^{2\pi} \int_0^1 \mathbf{R}_{11} \mathbf{I}(\tau_0, \mu', \varphi') \mu' d\mu' d\varphi', \quad (94)$$

where A is the surface albedo and \mathbf{R}_{11} is 4×4 matrix with the element (1,1) equal to 1 and all other elements equal to zero.

The SCIATRAN model allows the user to choose between the BRDF and Lambertian reflection. In the former case, one can either use one of the built-in models described in detail below or supply his/her own subroutine to calculate BRDF. For a Lambertian reflection, either a constant or spectral dependent albedo can be used. Additionally, a vegetation database providing the land surface albedo as a function of the season and geographical location [184] is incorporated into the SCIATRAN software package.

7.1. Land surface

One of the widely used models to approximate the bidirectional reflection function of a land surface is the so-called RPV model proposed by Rahman et al. [61]. In the framework of this model, the surface reflectance is parameterized by (i) the light reflection strength, ρ_0 , (ii) the so-called Minnaert exponent, k , determining the reflection anisotropy level, and (iii) the relative amount of the forward and backward reflection controlled by the asymmetry parameter g :

$$R(\mu_v, \mu_s, \varphi) = \rho_0 [\mu_v \mu_s (\mu_v + \mu_s)]^{k-1} F(g) H(G), \quad (95)$$

$$F(g) = \frac{1-g^2}{(1+2g \cos \zeta + g^2)^{3/2}}, \quad H(G) = 1 + \frac{1-\rho_0}{1+G}. \quad (96)$$

Here, the phase angle ζ and the function G are defined as

$$\cos \zeta = \mu_v \mu_s - \sqrt{(1-\mu_v^2)(1-\mu_s^2)} \cos \varphi_r, \quad (97)$$

$$G = [\tan^2 \vartheta_v + \tan^2 \vartheta_s + 2 \tan \vartheta_s \tan \vartheta_v \cos \varphi_r]^{1/2}. \quad (98)$$

Note that $\zeta = \pi - \gamma$, where γ is the scattering angle. In these equations $\mu_v = \cos \vartheta_v$ and $\mu_s = \cos \vartheta_s$, where ϑ_v and ϑ_s denote the viewing angle and the solar zenith angle, respectively. The latter are defined as angles between the vertical z -axis direction and the direction to the satellite and to the sun, respectively. This means that ϑ_v and ϑ_s are always smaller than $\pi/2$, i.e. their cosines, μ_v and μ_s , are always positive. In contrast to the original publication

of Rahman et al. [61], the relative azimuthal angle, φ_r , is defined here to be zero for the forward scattering, i.e. if the observer looks toward the illumination source. Thus, the relative azimuth angle used by Rahman et al. [61] differs by π from our definition. The function $H(G)$ describes the so-called hot spot effect seen in the measured data as a strong increase in the surface reflectance at $\vartheta_v = \vartheta_s$ and $\varphi_r = \pi$ (see e.g. [185]). Eqs. (95)–(98) reveal that for this angle combination the function G is equal to zero and the function $H(G)$ reaches thus its maximum value, which results in the surface reflection maximum.

The RPV model has been successfully employed to retrieve the surface albedo from Meteosat observations (see [186] and references therein), and its performance for various reflecting surface types has been investigated in detail by Cabot and Dedieu [187]. In SCIATRAN, the RPV model is implemented using the land surface parameters discussed by Lyapustin [188] allowing the user to account for BRDF of various reflecting surfaces such as the forest, savanna, plowed field, and other. The horizontal variability of the surface reflection properties is not considered.

Another BRDF model implemented in SCIATRAN is the kernel-based linear Ross–Li model, which is described by the following equation:

$$R(\mu_v, \mu_s, \varphi_r) = k_0 + k_v F_v(\mu_v, \mu_s, \varphi_r) + k_g F_g(\mu_v, \mu_s, \varphi_r). \quad (99)$$

Here, $F_v(\mu_v, \mu_s, \varphi_r)$ and $F_g(\mu_v, \mu_s, \varphi_r)$ represent the volume scattering and geometric-optic terms (or kernels), respectively, and k_0 , k_g , and k_v are the input parameters. As discussed by Maignan et al. [62], the geometric-optic kernel accounts for the mutual shadowing of protrusions and is obtained as follows:

$$F_g(\mu_v, \mu_s, \varphi_r) = \frac{\mu_v + \mu_s}{\pi \mu_s \mu_v} (t - \sin t \cos t - \pi) + \frac{1 + \cos \zeta}{2 \mu_s \mu_v},$$

$$\cos t = \frac{2 \mu_s \mu_v}{\mu_s + \mu_v} \sqrt{G^2 + (\tan \vartheta_s \tan \vartheta_v \sin \varphi_r)^2},$$

$$t = \begin{cases} \arccos t, & \cos t \leq 1 \\ 0, & \cos t > 1, \end{cases} \quad (100)$$

where G is given by Eq. (98). The volume scattering term is calculated in accordance with the Roujean et al. model [63], which approximate the radiative transfer within a vegetation canopy:

$$F_v(\mu_v, \mu_s, \varphi_r) = \frac{4C(\zeta, \zeta_0)}{3\pi(\mu_v + \mu_s)} \left[\left(\frac{\pi}{2} - \zeta \right) \cos \zeta + \sin \zeta \right] - \frac{1}{3}. \quad (101)$$

Here, the phase angle ζ is given by Eq. (97) and the correction term $C(\zeta, \zeta_0)$ is used to improve the hot spot reflection modeling. Following Maignan et al. [62] the latter is implemented as

$$C(\zeta, \zeta_0) = 1 + \left(1 + \frac{\zeta}{\zeta_0} \right)^{-1}, \quad (102)$$

where the parameter ζ_0 was found to be between 1 and 2° for most of the reflecting land surfaces [62]. If the correction term, $C(\zeta, \zeta_0)$, is set to the unity, Eqs. (99)–(101) result in the linear LSRT model which was implemented for example in the SHARM RT code [33].

Following Breón and Vermote [64] a more convenient representation for the kernel-based linear Ross–Li model is implemented in SCIATRAN which allows one to introduce a wavelength dependence of BRDF:

$$\begin{aligned}
 R_\lambda(\mu_v, \mu_s, \varphi_r) &= K_0(\lambda) \rho(\mu_v, \mu_s, \varphi_r), \\
 \rho(\mu_v, \mu_s, \varphi_r) &= 1 + K_g F_g(\mu_v, \mu_s, \varphi_r) + K_v F_v(\mu_v, \mu_s, \varphi_r), \\
 K_0(\lambda) &= A_\lambda \left[\frac{2}{\pi} \int_0^1 \int_0^1 \int_0^{2\pi} \rho(\mu_v, \mu_s, \varphi_r) \mu_v \mu_s d\mu_v d\mu_s d\varphi_r \right]^{-1}, \\
 A_\lambda &= c A_{\text{veg}}(\lambda) + (1-c) A_{\text{soil}}(\lambda), \\
 K_v &= \alpha_v x + \beta_v, \quad K_g = \alpha_g x + \beta_g, \\
 x &= (A_{\lambda_1} - A_{\lambda_2}) / (A_{\lambda_1} + A_{\lambda_2}).
 \end{aligned} \quad (103)$$

Here, $A_{\text{veg}}(\lambda)$ and $A_{\text{soil}}(\lambda)$ are the spherical albedos of the vegetation and soil, respectively, c is a fraction of the vegetation, A_{λ_1} and A_{λ_2} are the spherical albedos of the vegetation–soil mixture at wavelengths $\lambda_1 = 865$ nm and $\lambda_2 = 675$ nm, respectively, and the parameters α_v , β_v , α_g and β_g are listed in Table 8. Thus, the linear kernel-based soil–vegetation BRDF in SCIATRAN is initialized with the four input parameters, namely, spectral dependent Lambertian albedos of the soil, $A_{\text{soil}}(\lambda)$, and vegetation, $A_{\text{veg}}(\lambda)$, the vegetation fraction, c , in the vegetation–soil mixture, and the hot spot parameter ζ_0 .

An example BRDF of a grassland at a solar zenith angle of 50° is presented in Fig. 10. The left panel shows BRDF obtained from the RPV model as a polar contour plot with the solar direction depicted by the red asterisk and the hot spot (maximum reflection) seen at a viewing angle of 50° and an azimuthal angle of 180° . The right panel presents the principal plane cross sections of the grassland BRDF obtained with the RPV (black solid line) and the kernel-

based linear Ross–Li (blue dashed line) models. The results from the latter model are obtained at 410 nm with $c = 1$ (100% vegetation) and $\zeta_0 = 1.5^\circ$ while the RPV model is run with $\rho_0 = 0.014$, $k = 0.810$, and $g = -0.169$ (UV–visible spectral range). The plot is limited to viewing angles smaller than 85° because the RPV model results in an unrealistic enhancement of the BRDF at larger viewing angles, which is caused by very small μ_v values in Eq. (95). Similarly, the BRDF values resulting from the kernel-based linear Ross–Li model might be negative or unrealistically large at solar zenith angles above about 75° .

7.2. Snow surface

The bidirectional reflectance distribution function of a snow covered surface is implemented in the SCIATRAN model employing the extended RPV parameterization suggested by Degünther and Meerkötter [189]. In that study, a measured BRDF of a snow surface reported by Warren et al. [190] has been parameterized by introducing an additional additive term and an additional multiplicative term in the land surface RPV model discussed above, see Eqs. (95)–(98). The resulting expression for the snow surface BRDF is written as

$$R(\mu_v, \mu_s, \varphi_r) = \rho_0 \left\{ [\mu_v \mu_s (\mu_v + \mu_s)]^{k-1} F(g) H(G) + \frac{d}{\mu_s} \right\} T, \quad (104)$$

$$T = t_1 \exp[t_2(\pi - \zeta)] + 1, \quad (105)$$

where the factor T accounts for a strong forward scattering by snow, and, in accordance to [189], $\rho_0 = 0.728$, $k = 0.946$, $g = 0.042$, $d = -0.003$, $t_1 = 2$, and $t_2 = -4$. It should be noted that this parameterization has been obtained from the measurements in the UV–visible spectral range and does not account for a spectral variability of the snow reflectance.

Decrease in the snow reflectance at longer wavelengths, which results from the absorption by the ice, can be accounted for within SCIATRAN by using an asymptotic model [178]. In particular, following Kokhanovsky and Zege [191] the reflection function of an optically semi-infinite

Table 8
Parameters α_v , β_v , α_g , and β_g of the kernel-based linear Ross–Li model suggested by Breón and Vermote [64].

Wavelengths	α_v	β_v	α_g	β_g
< 700 nm	1.0	0.5	0.2	0.1
≥ 700 nm	2.0	0.5	−0.05	0.15

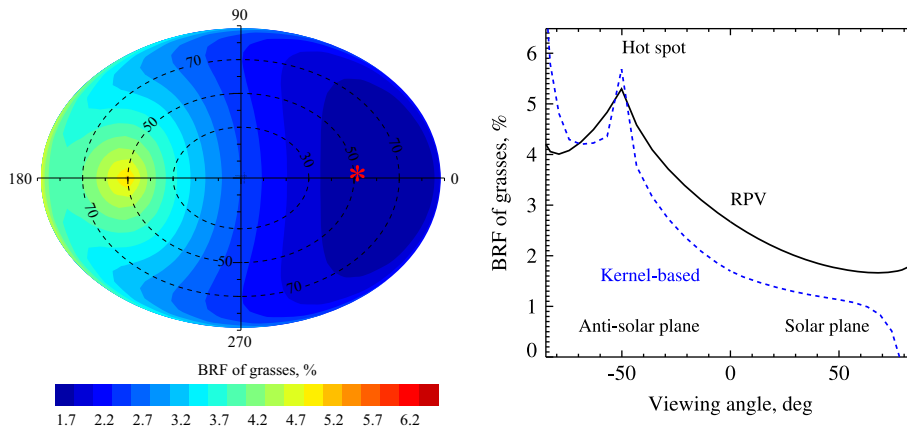


Fig. 10. BRDF of a grassland in the visible spectral range at a solar zenith angle of 50° . Left panel: BRDF resulting from the RPV model as a contour plot. The asterisk marks the solar direction. Right panel: principal plane cross sections for BRDFs resulting from the RPV (black solid line) and the kernel-based linear Ross–Li (blue dashed line) models. Positive viewing angles correspond to the forward scattering (observer looks toward the illumination source). (For interpretation of the references to color in this figure caption, the reader is referred to the web version of this article.)

snow layer can be obtained as

$$R(\mu_s, \mu_v, \varphi_r) = R_{0\infty}(\mu_s, \mu_v, \varphi_r) \exp[-4sQ(\mu_s, \mu_v, \varphi_r)], \quad (106)$$

where $R_{0\infty}(\mu_s, \mu_v, \varphi_r)$ represents the reflection function for a non-absorbing layer, μ_s and μ_v are the cosines of the solar and viewing zenith angles, respectively, and φ_r is the relative azimuth angle. The parameter s and the function $Q(\mu_s, \mu_v, \varphi_r)$ are given by

$$s = \sqrt{\frac{1-\omega_0}{3(1-\omega_0g)}} \quad \text{and} \quad Q(\mu_s, \mu_v, \varphi_r) = \frac{u(\mu_s)u(\mu_v)}{R_{0\infty}(\mu_s, \mu_v, \varphi_r)}, \quad (107)$$

respectively, where

$$u(\mu_{s,v}) = \frac{3}{7}(1 + 2\mu_{s,v}). \quad (108)$$

The values of the single scattering albedo, ω_0 , asymmetry parameter, g , and also of $R_{0\infty}(\mu_s, \mu_v, \varphi_r)$ depend on the wavelength and ice grain model (i.e. the shape and size of the ice crystals as well as their refractive index). Currently, only the parameterization for fractal ice grains [192] is available in SCIATRAN. In this case the reflection function for a non-absorbing layer is obtained as

$$R_{0\infty}(\mu_s, \mu_v, \varphi_r) = \frac{a + b(\mu_s + \mu_v) + c\mu_s\mu_v + p(\gamma)}{4(\mu_s + \mu_v)}, \quad (109)$$

where $a=1.246$, $b=1.186$, $c=5.157$, and the approximation for the phase function, $p(\gamma)$, is given by

$$p(\gamma) = 11.1e^{-0.087\gamma} + 1.1e^{-0.014\gamma}. \quad (110)$$

The scattering angle, γ , is to be provided in degrees. Furthermore, the asymmetry factor of 0.76 is assumed and the single scattering albedo is estimated according to [182].

A more accurate treatment of the snow surface reflection can be done by calculating the radiative transfer within the snow layer. In the framework of the SCIATRAN model a snow layer is represented by introducing at the bottom of the atmosphere a vertically inhomogeneous ice cloud layer with a very large optical thickness (see Section 6.4 for details on ice cloud parameterization). The performance of this approach is demonstrated in Section 12.2 by comparing the SCIATRAN simulations with the results from the other RT models (snow layer optical thicknesses up to 50 000) and in Section 13.3 by comparing the reflectance of a snow covered surface modeled by SCIATRAN with in situ measurements.

7.3. Ocean surface

The reflection of light from the ocean surface is represented in the SCIATRAN model by a weighted sum of the Fresnel reflection, R_F , water leaving radiation, R_{WL} , and reflection by sea foam, R_{SF} , as follows:

$$R_{\text{ocean}} = (1-c)[R_F + R_{WL}] + cR_{SF}, \quad (111)$$

where the wind speed dependent weighting factor, c , represents the foam covered fraction of the ocean surface. In the SCIATRAN model, the wind speed dependence of the parameter c is accounted for as suggested by Monahan and

Muircheartaigh [193]:

$$c = av^b. \quad (112)$$

Here, $a = 2.95 \times 10^{-6}$, $b = 3.53$, and v is the wind speed in (m/s) at 10 m altitude. It is worth noting here that all reflection terms in Eq. (111) depend on the illumination and observation geometry. A detailed discussion of the reflection terms is given in the subsections below.

7.3.1. Fresnel reflection

For a flat ocean surface, reflection of light is determined by Fresnel's law and the reflectance distribution is described by

$$\mathbf{R}(\mu, \mu', \varphi - \varphi') = \frac{\pi}{\mu'} \mathbf{R}_F(\mu') \delta(\mu - \mu') \delta(\varphi - \varphi'), \quad (113)$$

where pairs (μ', φ') and (μ, φ) denote incidence and reflection angles, respectively. Here, we use the same convention for μ' and μ as for μ_s and μ_v in Section 7.1, i.e. both μ' and μ are always positive. $\mathbf{R}_F(\mu')$ is the so-called Fresnel reflection matrix given by [169,67]

$$\mathbf{R}_F(\mu') = \frac{1}{2} \begin{bmatrix} r_{\parallel}^2 + r_{\perp}^2 & r_{\parallel}^2 - r_{\perp}^2 & 0 & 0 \\ r_{\parallel}^2 - r_{\perp}^2 & r_{\parallel}^2 + r_{\perp}^2 & 0 & 0 \\ 0 & 0 & 2 \operatorname{Re}\{r_{\parallel} r_{\perp}^*\} & 2 \operatorname{Im}\{r_{\parallel} r_{\perp}^*\} \\ 0 & 0 & -2 \operatorname{Im}\{r_{\parallel} r_{\perp}^*\} & 2 \operatorname{Re}\{r_{\parallel} r_{\perp}^*\} \end{bmatrix}. \quad (114)$$

Here, r_{\parallel} and r_{\perp} are the ratios of amplitudes of the incident and reflected electromagnetic waves for the parallel and perpendicular polarized components, respectively, asterisk denotes the complex-conjugation, and

$$2 \operatorname{Re}\{r_{\parallel} r_{\perp}^*\} = r_{\parallel} r_{\perp}^* + r_{\perp} r_{\parallel}^*, \quad 2 \operatorname{Im}\{r_{\parallel} r_{\perp}^*\} = i(r_{\parallel} r_{\perp}^* - r_{\perp} r_{\parallel}^*).$$

For simplicity reasons, the dependence of r_{\parallel} and r_{\perp} on μ' is not indicated. In the scalar case the Fresnel reflection coefficient simplifies to

$$R_F(\mu') = \frac{1}{2}(r_{\perp}^2 + r_{\parallel}^2). \quad (115)$$

A detailed discussion of the Fresnel reflection can be found elsewhere, e.g. [99].

In the case of a rough sea surface, the random orientation of the surface elements results in a certain probability that for given incidence, (μ', φ') , and reflection, (μ, φ) , angles there is a surface element contributing to the reflected radiation according to Fresnel's law. Most commonly, this probability is described by the wave slope probability distribution function (PDF) suggested by Cox and Munk [194,195].

In the SCIATRAN model, the reflection function of a rough sea surface is implemented following Nakajima and Tanaka [196]. In the scalar case this approach results in

$$R(\mu, \mu', \varphi - \varphi') = \frac{\pi}{4\mu\mu'\mu_n} \mathbf{P}(\mu_n, \sigma) S(\mu, \mu') R_F(\gamma), \quad (116)$$

where $\mathbf{P}(\mu_n, \sigma)$ is the wave slope PDF, σ^2 is the mean square slope, $S(\mu, \mu')$ accounts for wave shadowing effects [196–198],

$$\mu_n = \frac{\mu + \mu'}{\sqrt{2(1 - \cos \gamma)}} = \frac{\mu + \mu'}{2 \cos(\zeta/2)} \quad (117)$$

is the cosine of the angle between the surface element normal and the z -axis of the coordinate system, γ is the scattering

angle:

$$\cos \gamma = -\mu\mu' + \sqrt{(1-\mu^2)(1-\mu'^2)} \cos(\varphi-\varphi'), \quad (118)$$

and ζ is the phase angle given by Eq. (97).

One of the commonly used representations for the wave slope PDF is the isotropic Gaussian shape defined by

$$\mathbf{P}(\mu_n, \sigma) = \frac{1}{\pi\sigma^2\mu_n^3} \exp\left(-\frac{1-\mu_n^2}{\sigma^2\mu_n^2}\right), \quad (119)$$

where σ^2 depends on the wind speed. This wind speed dependence is usually approximated as $\sigma^2 = a + bv$, where v is the wind speed measured in (m/s) at the elevation 10 m above the sea surface and estimations for coefficients a and b can be found, e.g. in [199,200,194,196]. In the SCIATRAN model, both the wind speed and the approximation coefficients are to be provided by the user.

An example reflection function of the ocean surface calculated according to Eq. (116) for a wind speed of 10 m/s is shown in Fig. 11. The left panel of the plot depicts the so-called glint effect which is seen as a strong increase in the reflection function in the solar direction around the mirror reflection angle. The right panel shows the reflection function in the principal plane (i.e. $\varphi = 0$, we remind the reader that the solar azimuth angle, φ_0 , is assumed to be zero) calculated using the approximation coefficients a and b provided by different authors. One sees that the approximation coefficients influence significantly the maximum brightness and the width of the glint pattern.

In SCIATRAN, reflection of the direct solar beam ($\mu' = \mu_0$, $\varphi' = \varphi_0 = 0$) from the ocean surface can alternatively be modeled using the azimuthally dependent Gram–Charlier wave slope PDF, which is defined by

$$\begin{aligned} \mathbf{P}(z_u, z_c) = & \frac{1}{2\pi\sigma_c\sigma_u} e^{-(\xi^2+\eta^2)/2} \\ & \times \left[1 - \frac{C_{21}}{2}(\xi^2-1)\eta - \frac{C_{03}}{6}(\eta^2-3)\eta + \frac{C_{40}}{24}(\xi^4-6\xi^2+3) \right. \\ & \left. + \frac{C_{22}}{4}(\xi^2-1)(\eta^2-1) + \frac{C_{04}}{24}(\eta^4-6\eta^2+3) \right]. \quad (120) \end{aligned}$$

Here, $\xi = z_c/\sigma_c$ and $\eta = z_u/\sigma_u$ are the standardized slope components, σ_c and σ_u are the root mean square values of

the slope components z_c and z_u in the crosswind and upwind (the direction which the wind is coming from) directions, respectively. The latter are determined by the azimuth angle of the upwind direction (with respect to the solar azimuth angle), φ_W , as follows:

$$\begin{aligned} z_c &= z_y \cos \varphi_W - z_x \sin \varphi_W \quad \text{and} \\ z_u &= z_y \sin \varphi_W + z_x \cos \varphi_W, \end{aligned} \quad (121)$$

where the slope components z_x and z_y are given by

$$z_x = -\frac{\sin \vartheta \cos \varphi - \sin \vartheta_0}{\cos \vartheta + \cos \vartheta_0} \quad \text{and} \quad z_y = -\frac{\sin \vartheta \sin \varphi}{\cos \vartheta + \cos \vartheta_0}, \quad (122)$$

respectively. We remind the reader that according to our previous conventions $\mu = \cos \vartheta$, $\mu_0 = \cos \vartheta_0$, and both μ and μ_0 are positive.

Besides the wind direction, the Gram–Charlier wave slope PDF requires c_{ij} coefficients (see Eq. (120)) as well as σ_c and σ_u parameters to be specified by the user. The c_{ij} coefficients can be used as estimated either by Cox and Munk [194] or by Breon and Henriot [199]. A detailed discussion of these estimations and comparisons to measurements are presented by Breon and Henriot [199]. Following Cox and Munk [194], Ebuchi and Kizu [200], and Breon and Henriot [199], σ_c and σ_u can be represented as linear functions of the wind speed: $\sigma_c^2 = a_c + b_c v$ and $\sigma_u^2 = a_u + b_u v$. The estimations for the coefficients a_c , b_c , a_u , and b_u provided in the above-mentioned publications are used then as the input parameters for SCIATRAN. Alternatively, an input parameter structure similar to that of the SHARM code [33] can be used. In this case, the ratio $k = \sigma_u/\sigma_c$ specified by the user and the relationship $\sigma^2 = \sigma_u^2 + \sigma_c^2$ is used, where σ^2 is parameterized in the same manner as for the isotropic Gaussian PDF (see discussion after Eq. (119)).

It is worth noting here that in the SCIATRAN model, the reflection of the diffuse radiation from the rough sea surface is always calculated using the isotropic Gaussian PDF (Eq. (119)) while either Gaussian or Gram–Charlier (Eq. (120)) wave slope PDF can be selected for the reflected direct radiation.

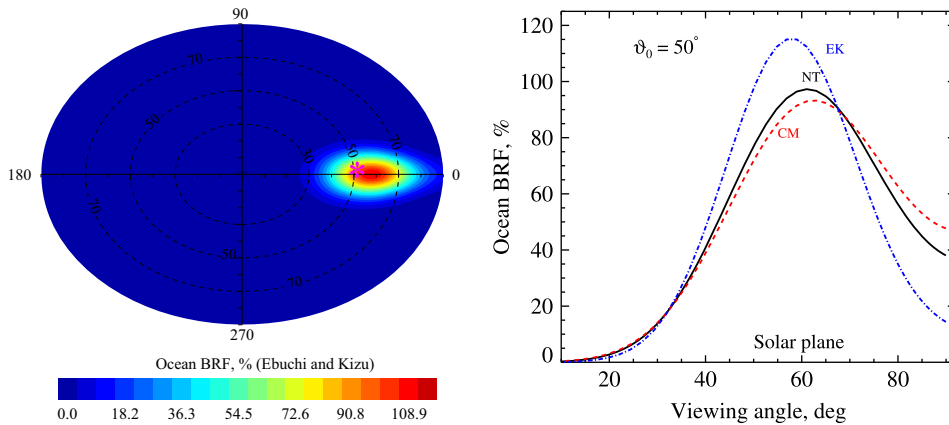


Fig. 11. Reflection function of the ocean surface at 500 nm for a solar zenith angle of 50° and 10 m/s wind speed. The left panel shows a polar contour plot obtained using a and b coefficients as suggested by Ebuchi and Kizu [200]. The right panel presents the reflection function in the principal plane for the parameters a and b from different authors, namely, EK – Ebuchi and Kizu [200], NT – Nakajima and Tanaka [196], CM – Cox and Munk [194].

In the vector mode, the reflection matrix for the rough ocean surface, $\mathbf{R}(\mu, \mu', \varphi - \varphi')$, is calculated with an external FORTRAN routine (ocean.phase.f) available at <http://www.giss.nasa.gov/~cirmim/brf>. A detailed description of the theoretical background is presented by Tsang et al. [198] and by Mishchenko and Travis [197].

7.3.2. Water leaving radiation and sea foam

Portion of the radiation passing through the air–water interface and returning back to the atmosphere after interaction with the ocean is commonly referred to as the water leaving radiation. In the SCIATRAN model, the modified Gordon approximation [201,131,202] is used to describe the corresponding reflection function:

$$R_{WL}(\vartheta_0, \vartheta, \varphi) = \pi \frac{m_a^2 \beta(\lambda, \gamma)}{m_w^2 \alpha(\lambda, C)} \frac{t_{aw}(\vartheta_0) t_{wa}(\vartheta')}{\cos \vartheta + \cos \vartheta'}. \quad (123)$$

Here, m_a and m_w are the refractive indices of the air and water, respectively, and ϑ' is the polar angle at which the radiation traveling through the water hits the air–water interface. This angle is related to the polar angle of the reflected radiation traveling through the atmosphere, ϑ , in accordance to Snell's law, $m_w \sin \vartheta' = m_a \sin \vartheta$. The absorption coefficient, $\alpha(\lambda, C)$, and volume angular scattering coefficient, $\beta(\lambda, \gamma)$, of the oceanic water are discussed in detail below (see Section 8, Eqs. (127), (130), and (134)). The former depends on the chlorophyll concentration, C , while the latter is a function of the angle between the light traveling direction and the refracted solar beam within the water. Transmission of the light from the atmosphere to the water and in the opposite direction is described by the functions, $t_{aw}(\vartheta_0)$ and $t_{wa}(\vartheta')$, respectively:

$$t_{aw}(\vartheta_0) = 1 - \frac{1}{\pi} \int_0^{2\pi} \int_{\pi/2}^{\pi} R_a(\vartheta_0, \vartheta, \varphi) \cos \vartheta \sin \vartheta d\vartheta d\varphi, \quad (124)$$

$$t_{wa}(\vartheta') = 1 - \frac{1}{\pi} \int_0^{2\pi} \int_0^{\pi/2} R_w(\vartheta', \vartheta, \varphi) \cos \vartheta \sin \vartheta d\vartheta d\varphi. \quad (125)$$

Here, R_a and R_w are the reflection functions of the air–water interface for the radiation traveling through the air and water, respectively. The SCIATRAN model uses look-up tables for the integral terms in Eqs. (124) and (125) which are pre-calculated for a set of angles and wind speeds. R_a has been calculated as described in Section 7.3.1 assuming the Gaussian wave slope PDF and the mean square slope given by $\sigma^2 = 0.003 + 0.00512\nu$, where ν is the wind speed. The calculations have been done for a single wavelength of 560 nm. The look-up table for R_w term has been adopted from [203].

Reflection function of whitecaps (foam) produced by breaking waves at the ocean surface is treated in the framework of SCIATRAN as proposed by Kokhanovsky [204]:

$$R_{SF}(\vartheta_0, \vartheta, \varphi) = R_0(\vartheta_0, \vartheta, \varphi) \exp(-\sqrt{D\alpha(\lambda, C)}). \quad (126)$$

Here, the parameter D accounts for both the air concentration in the foam and the thickness of bubble walls. In the SCIATRAN model this parameter needs to be set by user. Most commonly, it ranges between 1 and 100 mm.

In particular, the experimental data presented by Moore et al. [205] are well reproduced when using $D=85$ mm. The reflection function $R_0(\vartheta_0, \vartheta, \varphi)$ refers to a non-absorbing foam layer. In the SCIATRAN model $R_0(\vartheta_0, \vartheta, \varphi) = 1$ is used, which is a good approximation for thick foam layers. The water absorption coefficient $\alpha(\lambda, C)$ is calculated as discussed below, see Section 8.

8. Inherent optical properties of natural waters

As inherent optical properties (IOPs) of natural water one usually denotes properties that depend only on the composition of the water and are independent of the light field in which they are measured. In the radiative transfer theory most commonly used IOPs are the spectral absorption coefficient, spectral attenuation (extinction) coefficient and spectral volume scattering function (phase function). The implementation of these IOPs in the SCIATRAN radiative transfer model is discussed in detail in the following subsections. Similar to aerosols and clouds in the atmosphere, the IOPs of hydrosol particles can be either used as implemented in SCIATRAN or specified by the user in a control file (user-defined mode).

8.1. Spectral absorption coefficient

The total spectral absorption coefficient of sea water is obtained as

$$\alpha(\lambda, C) = \alpha_w(\lambda) + \alpha_C(\lambda) + \alpha_p(\lambda), \quad (127)$$

where $\alpha_w(\lambda)$ is the pure water absorption coefficient according to Pop and Fry [206]. Following Morel and Maritorena [207] the chlorophyll related absorption coefficient, $\alpha_C(\lambda)$, is written as

$$\alpha_C(\lambda) = 0.06 A_C(\lambda) C^{0.65}, \quad (128)$$

where $A_C(\lambda)$ is the wavelength dependent specific absorption coefficient of chlorophyll as described by Prieur and Sathyendranath [208] and C is the chlorophyll concentration in mg/m^3 . The pigment (dissolved organic matter components or yellow matter) absorption coefficient, $\alpha_p(\lambda)$, is implemented in accordance with Morel and Maritorena [207] as

$$\alpha_p(\lambda) = 0.2[\alpha_w(\lambda_0) + 0.06C^{0.65}]e^{-S(\lambda-\lambda_0)}. \quad (129)$$

Here, the spectral slope parameter, S , is set to 0.014 nm^{-1} and $\lambda_0 = 440 \text{ nm}$. As pointed out by Mobley [209], the spectral slope parameter varies from 0.014 to 0.019 nm^{-1} depending on the relative proportion of specific types of the yellow matter.

8.2. Spectral scattering coefficient

The elastic angular scattering coefficient of seawater is represented by a sum of the corresponding coefficients for the “pure” seawater, $\beta_w(\lambda, \gamma)$, and for the particulate matter, $\beta_p(\lambda, \gamma)$. Both coefficients are functions of the wavelength, λ , and scattering angle, γ . A detailed discussion of each term is presented below.

Pure water scattering: Following the studies of Morel [210], Shifrin [211], Buiteveld et al. [212], and Twardowski

et al. [213], the angular scattering coefficient of the pure water is represented as

$$\beta_w(\lambda, \gamma) = \beta_w(\lambda, 90^\circ)[1 + p(90^\circ) \cos^2 \gamma], \quad (130)$$

where $\beta_w(\lambda, 90^\circ)$ is the scattering coefficient for a scattering angle of 90° , $p(90^\circ) = (1 - \delta)/(1 + \delta)$ is the degree of polarization at 90° , and δ is the depolarization ratio. In the framework of the SCIATRAN model, one of the following parameterizations for $\beta_w(\lambda, 90^\circ)$ as proposed by Morel [210], Shifrin [211], and Buiteveld et al. [212], respectively, can be selected:

$$\beta_w(\lambda, 90^\circ) = 2.18 \times 10^{-4} (450/\lambda)^{4.32}, \quad (131)$$

$$\beta_w(\lambda, 90^\circ) = 0.93 \times 10^{-4} (546/\lambda)^{4.17}, \quad (132)$$

$$\beta_w(\lambda, 90^\circ) = \frac{2\pi^2}{\lambda^4 B_T} k T_a m^2 \left(\frac{\partial m}{\partial P} \right)_T C_f, \quad (133)$$

where λ denotes the wavelength in nm. The former two parameterizations are obtained for the normal pressure, temperature of 20°C , and depolarization ratio of 0.09 (i.e. $p(90^\circ) = 0.834862$). In the parameterization by Buiteveld et al. [212] given by Eq. (133) B_T denotes the isothermal compressibility of water (temperature dependent), k is the Boltzmann constant, T_a is the absolute temperature, m is the refractive index of water (function of λ and temperature) and $\partial m / \partial P$ is its pressure derivative. In the SCIATRAN model, approximations for B_T , m , and $\partial m / \partial P$ are adopted from Twardowski et al. [213] (see their Table 1). The Cabanes factor, $C_f = (6 + 6\delta)/(6 - 7\delta)$, accounting for the anisotropy of water due to fluctuations in the orientation of the molecules is calculated assuming a depolarization ratio, δ , of 0.051 as recommended by Farinato and Roswell [214].

As discussed by Twardowski et al. [213] the parameterizations given by Eqs. (131)–(133) need to be corrected for the salinity of the seawater. This is done by multiplying $\beta_w(\lambda, \gamma)$ by an empirical correction written as $[1 + 0.3S/37]$, where S is the salinity of the seawater. This correction has been obtained based on theoretical predictions published by Shifrin [211] and experimental results summarized by Morel [210]. A linearity with respect to the salinity has been assumed.

Scattering by the particulate matter: The particulate matter is usually assumed to consist of phytoplankton cells, detritus, bacteria, and suspended particles of mineral origin. In the SCIATRAN model its contribution to the total angular scattering coefficient can be accounted for by using two different approaches. The first one employs the measurements of the angular scattering coefficient performed by Petzold [215,216]. The alternative approach proposed by Kopelevich [217] uses a scattering model for particulates in water. The model is developed to approximate results of in situ measurements of inherent optical properties and particle size distributions made during several decades in the Pacific, Indian and Atlantic Oceans. According to this model, the angular scattering coefficient expressed in $\text{m}^{-1} \text{sr}^{-1}$ is represented by

$$\beta_p(\lambda, \gamma) = v_s \beta_s(\gamma) \left(\frac{550}{\lambda} \right)^{1.7} + v_l \beta_l(\gamma) \left(\frac{550}{\lambda} \right)^{0.3}, \quad (134)$$

where $\beta_s(\gamma)$ and $\beta_l(\gamma)$ are the angular scattering coefficients at 550 nm for small and large particles, respectively, and v_s and v_l are referred to as volume concentrations in units of cm^3 of particles per m^3 of water, i.e. in parts per million. The angular scattering coefficients are provided in a tabular form for discrete values of scattering angle among others by Haltrin [216]. Typical variation ranges of the volume concentrations have been estimated by Mobley [209] as $0.01 \leq v_s \leq 0.2$ and $0.01 \leq v_l \leq 0.4$. For each fraction of particles the concentration (mass of particles in a unit volume of water) is obtained by multiplying the corresponding volume concentration by the density of a single particle, ρ , e.g. for small particles $C_s = \rho_s v_s$. The small particle fraction is considered consisting of terrigenous particles with density $\rho_s = 2 \text{ g/cm}^3$ and relative (to the water) refractive index $n_s = 1.15$. Their size distribution has been found to be described by a combination of three Junge distributions $r^{-\nu}$ with $\nu = 2.5$ for $r \in [0.01, 0.05] \mu\text{m}$, $\nu = 3.5$ for $r \in [0.05, 0.1] \mu\text{m}$, and with $\nu = 4.5$ for $r \in [0.1, 1.3] \mu\text{m}$ [216]. The large fraction consist of organic particles of phytoplankton and detritus with density $\rho_l = 1 \text{ g/cm}^3$ and relative refractive index $n_s = 1.03$. The corresponding size distribution has been found to be described by the Junge distribution with $\nu = 3$ for $r \in [1.3, 13] \mu\text{m}$. A detailed discussion of this model can be found among others in [216,209,211]. According to Haltrin [216] the model gives very good predictions of the angular scattering coefficient for open oceanic water and for clean biologically stable waters with no clay or sand particles suspended by the water movement.

The angular scattering properties of the natural water can be described in the framework of the SCIATRAN model by (i) the small particle and the large particle phase functions according to the Kopelevich model [217], (ii) the pure water phase function according to the Shifrin model [211], (iii) the Petzold phase function adopted by Mobley et al. [218], and (iv) the Henyey–Greenstein phase function with an asymmetry factor of 0.95. As shown by Mobley et al. [218] this value of the asymmetry factor provides the best consistency with the average phase function for the natural water resulting from the measurements. Fig. 12 shows the above listed phase functions at a wavelength of 550 nm.

9. Sources of radiation

The radiative transfer processes can be modeled in the framework of SCIATRAN taking into account both inner and outer sources of radiation. The former sources include the thermal emission within the atmosphere and from the Earth's surface and the outer source is the incident solar radiance. The latter is characterized by the spectral flux of electromagnetic radiation through a unit area perpendicular to the traveling direction of the solar light (extra-terrestrial solar flux). This quantity is also often referred to as the irradiance and expressed in units of the power per unit area per unit spectral interval, e.g. $\text{W m}^{-2} \text{nm}^{-1}$.

The spectral database distributed along with the SCIATRAN model contains the extra-terrestrial solar spectrum in the spectral range $0.2\text{--}2.5 \mu\text{m}$ measured by Kurucz [219] and the solar spectrum referred to as “Standard Extraterrestrial

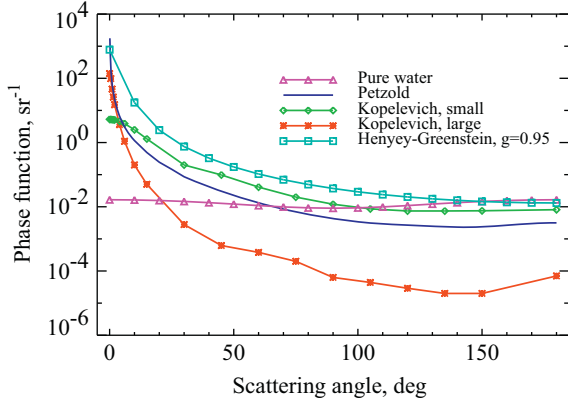


Fig. 12. Phase functions for natural water implemented in the SCIATRAN model. Wavelength dependent phase functions are calculated at the wavelength of 550 nm.

Spectrum Reference E-490-00" (SES_E490) (<http://rredc.nrel.gov/solar/spectra/am0/astm:2000.html>) covering the spectral range 0.12–400 μm . Furthermore, the user can supply his/her own irradiance spectra.

In the absence of the thermal emission, the solution of RTE is proportional to the solar irradiance and thus any appropriate irradiance units (IU) can be used. Besides the real irradiance SCIATRAN model can also be run assuming a spectral independent solar irradiance of π [IU] or 1 [IU], which is often used for comparisons of radiative transfer models. This approach, however, must not be used if both the solar radiation and the thermal emission are considered. In this case the solution of RTE is determined by the sum of both sources and thus both contributions must be expressed in the same physical units.

10. Output radiometric quantities

One of the main radiometric output quantities of SCIATRAN is the intensity of the radiation field (also referred to as the radiance), which describes the power of an electromagnetic wave per unit area per unit spectral interval per unit solid angle. In the SCIATRAN model the intensity is expressed in units of IU sr^{-1} where IU are the units of the extra-terrestrial solar flux (see Section 9). The radiance can be modeled at various viewing (ϑ, φ) and solar zenith angles (ϑ_0), observer altitudes z , and wavelengths λ . With the exception of the direct solar light observations the intensity of the diffuse radiation field is modeled by SCIATRAN, i.e. the contribution of the direct solar radiation is not included in the results.

In the vector mode the SCIATRAN model calculates the so-called Stokes vector containing the intensity and three additional Stokes parameters describing the polarization state of the electromagnetic radiation. All components of the Stokes vector are expressed in the same units (IU sr^{-1}). To facilitate analysis of the polarization state SCIATRAN provides additional output for the so-called ellipsometric parameters, namely, degree of polarization, degree of linear and circular polarization, ellipticity, and the polarization angle. These quantities are calculated following Hovenier et al. [9] (see Display 1.1 in this reference).

Instead of the intensity, the upward traveling radiation can also be described by the so-called reflection function or reflectance defined by

$$R(Z, \vartheta, \varphi; \mu_0) = \frac{\pi I(Z, \vartheta, \varphi; \mu_0)}{\mu_0 E_0}, \quad (135)$$

where E_0 is the incident solar flux at the top of the atmosphere and $\mu_0 = \cos \vartheta_0$ is the cosine of the solar zenith angle. For the sake of simplicity the explicit notation of the wavelength dependence is skipped throughout this section.

Additionally the SCIATRAN model can provide the vertical optical thickness as a function of wavelength, λ , for aerosol and cloud extinction, Rayleigh scattering, and all gaseous components:

$$\tau = \int_0^H k(z) dz, \quad (136)$$

where H is the top of the atmosphere altitude and $k(z)$ is the extinction coefficient at the altitude z . This output has been used to obtain vertical optical thicknesses of main gaseous absorbers in the UV, VIS, NIR, and TIR spectral ranges shown in Figs. 6 and 7 in Section 6.1.

Other quantities which can be modeled with SCIATRAN are the upward, $F_u(z, \mu_0)$, and downward, $F_d(z, \mu_0)$, diffuse fluxes as well as the downward direct flux, $F_{\text{dir}}^d(z, \mu_0)$, as functions of the altitude, z , within both the atmosphere and ocean:

$$F_u(z, \mu_0) = 2\pi \int_0^1 I^0(z, \mu; \mu_0) \mu d\mu, \quad (137)$$

$$F_d(z, \mu_0) = 2\pi \int_{-1}^0 I^0(z, \mu; \mu_0) \mu d\mu, \quad (138)$$

$$F_{\text{dir}}^d(z, \mu_0) = \mu_0 E_0 e^{-\tau_z/\mu_0}, \quad (139)$$

where $I^0(z, \mu; \mu_0)$ is the azimuthally averaged intensity (the zeroth Fourier harmonic of the intensity), and τ_z is the total optical depth between the altitude z and the top of the atmosphere. For the coupled ocean–atmosphere model the downward direct flux within the ocean is given by

$$F_{\text{dir}}^d(z, \mu_0) = \frac{\mu_0}{\mu'_0} E_0 [1 - R_F(\mu_0)] e^{-\tau_a/\mu_0} e^{-(\tau_z - \tau_a)/\mu'_0}, \quad (140)$$

where μ'_0 is the cosine of the solar zenith angle within the ocean, τ_a is the total optical thickness of the atmosphere. In the case of specular reflection from the ocean surface also the upward direct flux is present:

$$F_{\text{dir}}^u(z, \mu_0) = \mu_0 E_0 R_F(\mu_0) e^{-(2\tau_a - \tau_z)/\mu_0}. \quad (141)$$

Here, $R_F(\mu_0)$ is the Fresnel reflection coefficient of the ocean–atmosphere interface (see Section 7.3.1). Additionally, the actinic flux (or spherical flux [56]), which is often needed for photochemical calculations, can be calculated with SCIATRAN. Within the atmosphere the actinic flux is given by

$$\Phi(z, \mu_0) = 2\pi \int_{-1}^1 I^0(z, \mu; \mu_0) d\mu + \frac{F_{\text{dir}}^d(z, \mu_0)}{\mu_0} + \frac{F_{\text{dir}}^u(z, \mu_0)}{\mu_0}, \quad (142)$$

where the last term is appropriate only in the case of specular reflection. All fluxes are calculated in the irradiance

units (IU) which are determined by the units of the extra-terrestrial solar flux.

By dividing the diffuse and direct fluxes given by Eqs. (137)–(139) by the extraterrestrial solar flux, $\mu_0 E_0$, one obtains the plane albedo, diffuse transmittance under direct illumination, and direct transmission, respectively:

$$A_p(z, \mu_0) = \frac{F_u(z, \mu_0)}{\mu_0 E_0}, \quad t_d(z, \mu_0) = \frac{F_d(z, \mu_0)}{\mu_0 E_0},$$

$$t_{\text{dir}}(z, \mu_0) = e^{-\tau_z/\mu_0}. \quad (143)$$

Taking into account Eqs. (135) and (137) a commonly used expression for the plane albedo containing the integral of the reflection function [91,7] can be obtained:

$$A_p(z, \mu_0) = 2 \int_0^1 R^0(z, \mu; \mu_0) \mu d\mu, \quad (144)$$

where $R^0(z, \mu; \mu_0)$ is the zeroth Fourier harmonic of the reflection function.

Furthermore, the SCIATRAN model can be used to calculate the spherical albedo, $A_s(z)$, and the global transmittance (or diffuse transmittance under diffuse illumination), $T_d(z)$, which are defined as follows:

$$A_s(z) = \frac{4\pi}{E_0} \int_0^1 \int_0^1 I^0(z, \mu; \mu_0) \mu \mu_0 d\mu d\mu_0, \quad (145)$$

$$T_d(z) = \frac{4\pi}{E_0} \int_{-1}^0 \int_0^1 I^0(z, \mu; \mu_0) \mu \mu_0 d\mu d\mu_0 \quad (146)$$

Similar to the plane albedo, the spherical albedo can also be expressed as the integral of the reflection function:

$$A_s(z) = 4 \int_0^1 \int_0^1 R^0(z, \mu; \mu_0) \mu \mu_0 d\mu d\mu_0. \quad (147)$$

Comparing this equation to Eq. (144) a relation between the spherical and the plane albedo is obtained:

$$A_s(z) = 2 \int_0^1 A_p(z, \mu_0) \mu_0 d\mu_0. \quad (148)$$

The users who perform sensitivity studies or develop retrieval algorithms might benefit from the so-called weighting functions provided by SCIATRAN. The weighting functions also referred to as Jacobians describe sensitivity of the simulated radiance to variations of atmospheric and surface parameters and are obtained as partial derivatives of the intensity with respect to these parameters:

$$\mathbf{W}_k(z_v, \mu_v, \varphi_v) = \frac{\partial I(z_v, \mu_v, \varphi_v)}{\partial p_k}. \quad (149)$$

Here, z_v is the observer altitude, μ_v and φ_v define the viewing direction, and p_k is an atmospheric or surface parameter of interest. The weighting functions are provided in units of IU $\text{sr}^{-1} \cdot [p_k]^{-1}$, where $[p_k]$ are the units of the parameter p_k , e.g. IU $\text{sr}^{-1} \text{ km}$ for the extinction coefficient in (km^{-1}). In a linear approximation the weighting function can be used to obtain the intensity corresponding to a perturbed value of a parameter,

$$I(p_k + \Delta p_k, z_v, \mu_v, \varphi_v) \approx I(p_k, z_v, \mu_v, \varphi_v) + \mathbf{W}_k(z_v, \mu_v, \varphi_v) \Delta p_k, \quad (150)$$

where $I(p_k, z_v, \mu_v, \varphi_v)$ is the intensity of the radiation field corresponding to the unperturbed parameter value.

The weighting functions of the following parameters are currently implemented in SCIATRAN:

- number density of all atmospheric gaseous absorbers included in SCIATRAN;
- scattering and absorption coefficients of aerosols;
- scattering and absorption coefficients of clouds;
- cloud properties: effective radius of particles, particle number density, liquid and ice water content;
- cloud extension: top and bottom heights, optical thickness;
- pressure and temperature;
- surface elevation and Lambertian surface albedo.

The weighting functions can be calculated simultaneously with the radiance owing to the very efficient forward–adjoint technique [68,220,69] employed in the SCIATRAN model.

There are also two additional output quantities of SCIATRAN provided to support the algorithms relying on the DOAS technique [221,222]. The first one is the air mass factor describing the effective light path in the entire atmosphere obtained as

$$A(z_v, \mu_v, \varphi_v) = \frac{1}{\tau(\lambda)} [\ln I_0(z_v, \mu_v, \varphi_v) - \ln I(z_v, \mu_v, \varphi_v)], \quad (151)$$

where $\tau(\lambda)$ is the vertical optical thickness of the absorber which the air mass factor is calculated for and the radiances $I(z_v, \mu_v, \varphi_v)$ and $I_0(z_v, \mu_v, \varphi_v)$ are calculated including and excluding this absorber, respectively. The box air mass factor has a similar meaning but is related to each particular altitude layer, i.e. it describes the effective light path within an atmospheric layer. For each particular absorber and altitude layer the box air mass factor is closely related to the weighting function, see [223] for details, and is obtained in the framework of SCIATRAN as

$$\mathbf{A}_k(z_v, \mu_v, \varphi_v) = - \frac{\mathbf{W}_k(z_v, \mu_v, \varphi_v)}{I(z_v, \mu_v, \varphi_v) \Delta z_k \sigma}, \quad (152)$$

where σ is the absorber cross section and Δz_k is the geometrical thickness of the altitude layer z_k .

11. Comparisons to other radiative transfer models: scalar mode

11.1. Plane-parallel atmosphere

In this section simulations performed with the SCIATRAN model in the scalar mode, i.e. neglecting the polarization of light, are compared to the results from the Successive Order (SO) technique [224,20], Spherical Harmonics (SHARM) radiative transfer code [33], and Discrete Ordinate Radiative Transfer (DISORT) solver [34]. The latter is publicly available via http://climate.gsfc.nasa.gov/pub/wiscombe/Multiple_Scatt. The main feature of the SO technique is the summation of different orders of scattering which is very efficient for a clean atmosphere, where the light collected by an optical instrument undergoes just a few scattering events. The SHARM code is a rigorous radiative transfer model employing the spherical harmonics method, which is as accurate as the DISORT code

relying on the well-established discrete-ordinates technique [34].

11.1.1. Rayleigh scattering

For a pure molecular atmosphere the sun-normalized intensities (see below for details) at the top of the atmosphere calculated with the SCIATRAN, SHARM, and SO radiative transfer models are compared. The calculations are done for three solar zenith angles of 6.5° , 25.1° , and 69.6° , three relative azimuthal angles of 0° , 90° , and 180° , and viewing angle increasing from 2.84° to 88.14° with an increment of 3.71° . The results are compared for a black and ocean underlying surfaces. The calculations are done with the Rayleigh optical thickness of 0.24 and the depolarization term (King factor) set to 1. The grids for the solar zenith and viewing angles in all models are set in accordance to those from the SO code. The computation results from the SO code have kindly been provided by F. Zagolsky (private communication).

The comparison results are shown in Fig. 13. As the differences between the models are similar for all considered solar zenith angles only the results for a solar zenith angle of 25.1° are presented. The plots show the sun-normalized intensities, I_N , in the left panels and percentage differences in the right panels as functions of the viewing angle for three different azimuth angles (0° , 90° , and 180°). Here, the sun-normalized intensity is defined as

$$I_N = \frac{\pi I}{E_0}, \quad (153)$$

where I is the backscattered solar radiance and E_0 is the extra-terrestrial solar flux. We note that the relative azimuth angle of 180° corresponds to the backward scattering. The results are presented for a black (upper panels) and ocean (lower panels) underlying surfaces.

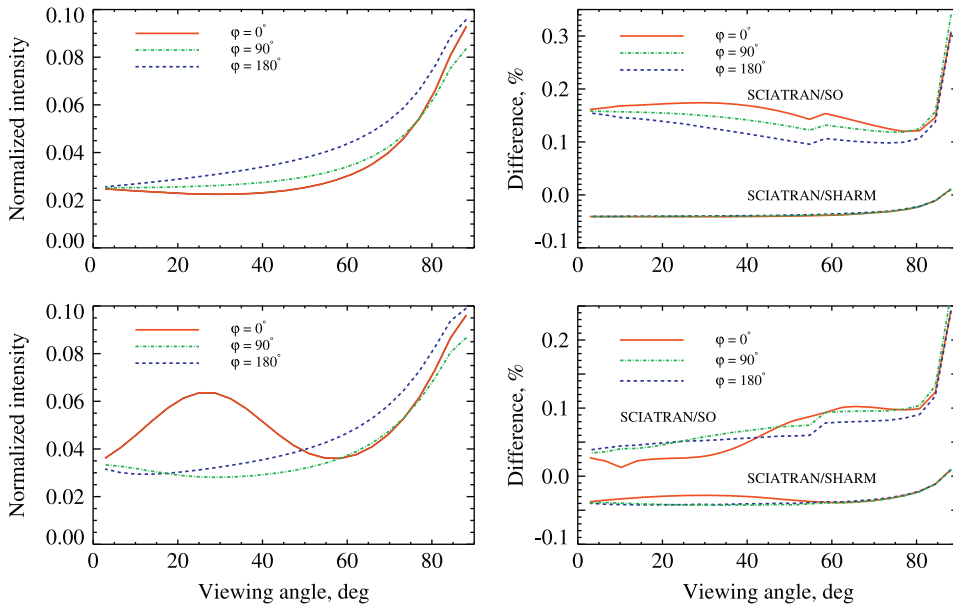


Fig. 13. Sun-normalized intensities at the top of atmosphere, Eq. (153), calculated with SCIATRAN (left panels) and percentage differences between the models (right panels). The calculations are done at a solar zenith angle of 25.1° for a black (upper panels) and ocean (lower panel) underlying surfaces.

The latter is described by the Fresnel reflection using the Cox–Munk approximation with a wind speed of 5 m/s. The sun-normalized intensities simulated for the underlying ocean surface (left panel of Fig. 13) clearly show the glint effect observed as a significant increase in the radiance reflected towards the observer ($\varphi = 0^\circ$) if the viewing angle is close to the solar zenith angle ($\sim 25^\circ$).

Fig. 13 reveals an excellent agreement between the SCIATRAN and SHARM models with relative differences never exceeding 0.05% for both black and ocean underlying surfaces. The agreement between the SCIATRAN and SO codes is slightly worse with relative differences generally between 0.1% and 0.2% for a black underlying surface and below 0.1% for an ocean surface. The disagreement increases for viewing angles larger than $\sim 85^\circ$ which is most probably because of the standard accuracy mode used in the SO code. This behavior is consistent with the results reported by Kotchenova et al. [18] for the comparisons between SHARM and 6SV1 models. Similar to the SO code the latter model relies on the successive order of scattering technique. For the standard accuracy mode the 6SV1 model was shown to diverge from SHARM by up to 0.3%. For a black underlying surface a comparison between SCIATRAN and DISORT has also been performed revealing an excellent agreement within 0.02% (results are not shown here).

11.1.2. Mie scattering and thermal emission

In this section the upward radiance at the top of the atmosphere and the downward radiance at the bottom of the atmosphere modeled with SCIATRAN accounting for the Mie scattering and thermal emission are compared with the DISORT results. The calculations are done at a wavelength of $3.7 \mu\text{m}$ and a solar zenith angle of 27° . Both radiative transfer models use (i) vertical profiles of the pressure, temperature, and gaseous species for July at

55 °N from the climatological database described in Section 6.1, (ii) Lambertian surface albedo of 0.3 (surface emissivity of 0.7); (ii) maritime/background aerosols according to the LOWTRAN aerosol parameterization [60], (iv) irradiance spectrum from SES_E490 model (see Section 9).

The comparison results are presented in Fig. 14. The upper panels show the upward radiance at the top of the atmosphere on the left and the downward radiance at the bottom of the atmosphere on the right. The scattered solar and thermal radiance is shown in red while the results obtained excluding the thermal emission are shown in blue. The lower panels show the percentage differences between the corresponding results from SCIATRAN and DISORT. The plot reveals that the thermal emission enhances significantly the upward radiance which is mainly due to a significant contribution of the thermal emission from the underlying surface. In contrast, the downward radiance is dominated by the strong forward scattering of the solar radiation while the contribution of the thermal emission from the atmosphere is rather small becoming noticeable only at grazing observation angles. In all considered cases the results from SCIATRAN and DISORT agree very well with maximum relative difference of about 0.1%.

11.2. Spherical atmosphere

Radiance at the top of the atmosphere calculated with five radiative transfer models, namely, SCIATRAN, SIRO [55], MCC++ [54], GSLS [225], and LIMBTRAN [129], for the limb viewing geometry are compared by Loughman et al. [226] for a variety of observation conditions. The calculations are

done including the Rayleigh and aerosol scattering as well as the ozone absorption. All considered models treat single scattering fully spherically while an approximation to account for the multiple scattering contribution is used in the LIMBTRAN model and in the CDI solver [109] of the SCIATRAN model. These models are referred to as the approximative spherical models. The other models (SIRO, MCC++, GSLS, and CDIPI [48] solver of the SCIATRAN model) treat both single and multiple scattering contributions fully spherically and are referred to as the fully spherical models.

The comparisons are performed for four solar zenith angles (20°, 60°, 80°, and 90°), three relative azimuth angles (20°, 90°, and 160°), and two surface albedos (0 and 0.95). For the single scattered radiances all models are found to agree within 1% almost everywhere. Comparisons of the total radiances show larger differences with 2–4% spread among the results of the fully spherical models. The approximative spherical models are found to show a positive bias increasing with the tangent height up to about 8% at 60 km.

11.3. Ocean overlayed by a black atmosphere

Results of the radiative transfer modeling through the ocean overlayed by a black atmosphere obtained with SCIATRAN are discussed in detail by Blum et al. [227]. In particular, simulations with SCIATRAN model and matrix operator [26], finite element [44], and invariant embedding [228] methods are compared to the results published by Mobley et al. [218] (results from seven radiative transfer models for several standard problems related to the underwater radiative transfer). For most of the considered cases the results from all models agree very well. In all

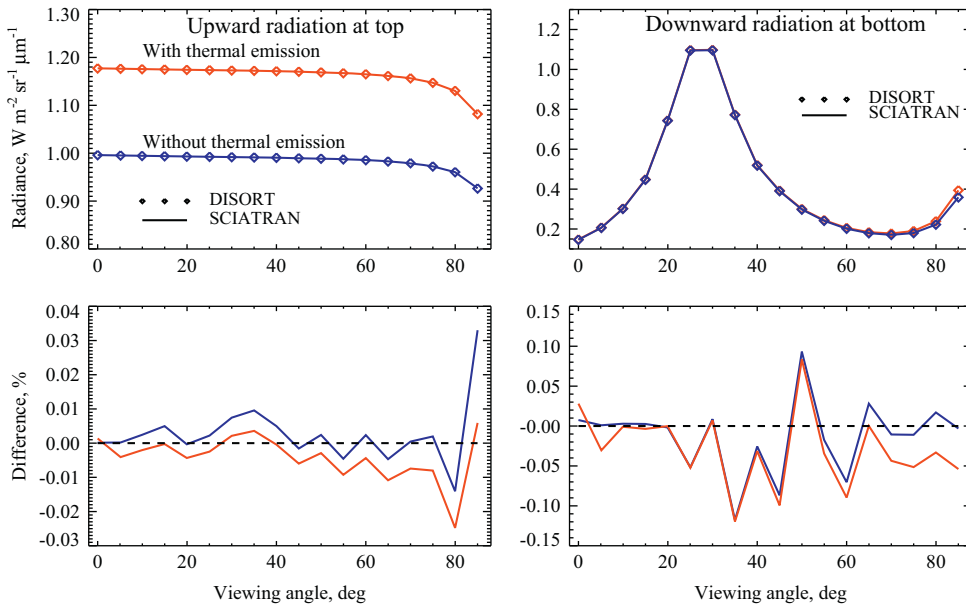


Fig. 14. Comparison between SCIATRAN and DISORT models. Upper panel: upward radiance at the top of the atmosphere (left panel) and downward radiance at the bottom of the atmosphere (right panel). The scattered solar and thermal radiance is shown in red while the results obtained excluding the thermal emission are shown in blue. The calculations are done at a wavelength of $\lambda = 3.7 \mu\text{m}$ and a solar zenith angle of 27°. Lower panels: percentage differences between the SCIATRAN and DISORT results. (For interpretation of the references to color in this figure caption, the reader is referred to the web version of this article.)

cases SCIATRAN results are well within the spread of the compared models.

11.4. Coupled ocean–atmosphere system

In this section radiative transfer simulations performed with SCIATRAN for a coupled ocean–atmosphere system are compared to the results from 3D Monte Carlo (MC) code [229] and the RAY radiative transfer model [230]. It should be noted here that the current version of SCIATRAN does not account for the polarization of light for a coupled ocean–atmosphere system while only the results for vector radiative transfer were available for the 3D MC code. The RAY model can be run in both scalar and vector modes.

The comparison is performed for the ocean–atmosphere scenario adopted from You et al. [229], namely, (i) ocean physical depth is 10 m and its extinction coefficient is 1 m^{-1} , (ii) physical depth of the atmosphere is 10 m and its extinction coefficient is 0.025 m^{-1} , (iii) Rayleigh scattering in the atmosphere, (iv) light scattering in the ocean is described by the Henyey–Greenstein phase function with an asymmetry factor of 0.95 (see Fig. 12), (v) the single scattering albedo is 0.5 for both the atmosphere and ocean, (vi) the Lambertian ocean bottom albedo is 0.5, (vii) the refractive indices of the atmosphere and the ocean are 1.0 and 1.338, respectively, (viii) the solar zenith angle is zero. The results are presented in terms of the sun-normalized intensity defined by $I_N = I/E_0$, where E_0 is the extra-terrestrial solar flux.

The comparison results are presented in Fig. 15. The upper left panel shows downward intensity just below the ocean surface (0.001 m depth) calculated with the 3D MC, RAY, and

SCIATRAN models. For the RAY model the results of vector calculations (i.e. accounting for the polarization of light) are presented while only scalar calculations can be done with SCIATRAN and only vector mode is available for 3D MC. A slight disagreement between SCIATRAN and other models within the Fresnel cone is found to be caused by the polarization effects. This is demonstrated in the upper right panel of Fig. 15 where the same intensity from SCIATRAN is compared to the scalar calculations with the RAY model. The plot reveals that including polarization effect the results from the RAY code agree very well with 3D MC simulations (upper left panel) while a good agreement is observed between the results from SCIATRAN and the scalar mode of RAY (upper right panel).

The lower panels of Fig. 15 show the results from the SCIATRAN and 3D MC models obtained for a wind-roughened ocean surface using the Gaussian wave slope probability distribution function according to Cox and Munk [194]. The calculations are done for a wind speed of 5 m/s (left plot) and 10 m/s (right plot) revealing a good agreement between the models. Because of compatibility reasons no calculations for this scenario can be done with the RAY model.

12. Comparisons to other radiative transfer models: vector mode

12.1. Plane-parallel medium underlain by a Lambertian surface

For a plane-parallel non-absorbing molecular atmosphere, the outgoing radiance at the top of the atmosphere calculated with SCIATRAN is compared to the tabulated

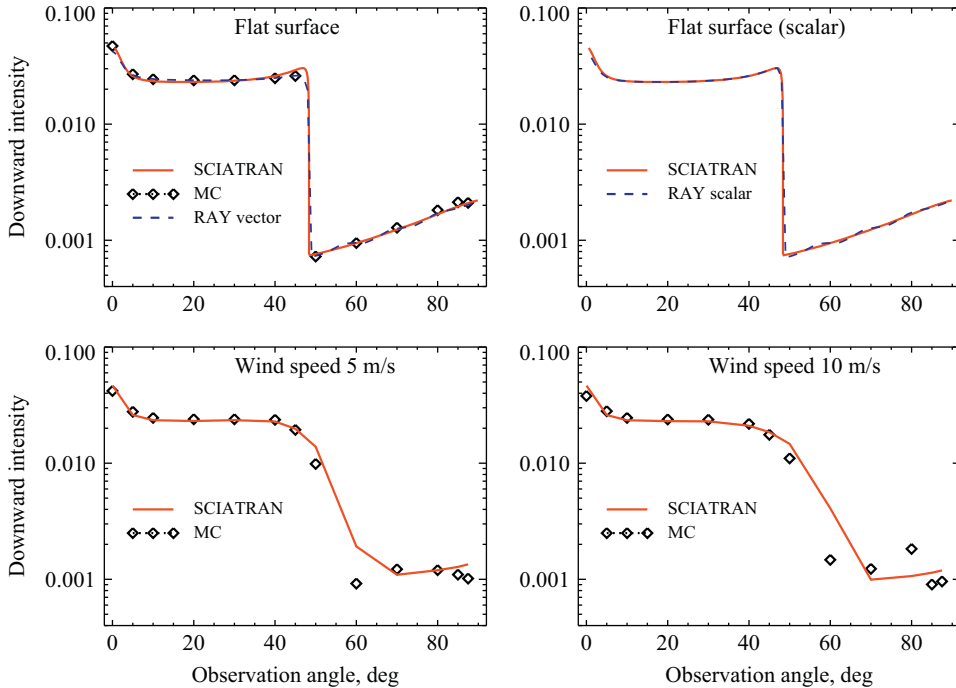


Fig. 15. Downward sun-normalized intensity just below the ocean surface (0.001 m depth) calculated with SCIATRAN, 3D MC, and RAY codes for a coupled ocean–atmosphere system. Upper panels: results for an absolutely flat ocean surface resulting from vector (except for SCIATRAN) and scalar calculations (left and right panels, respectively). Lower panels: results for a wind-roughened ocean surface for a wind speed of 5 m/s (left panel) and 10 m/s (right panel).

values published by Coulson et al. [231]. The comparison is performed at a solar zenith angle of about 23° for a zero surface albedo, and three optical thicknesses (0.05, 0.25, and 1). For the first component of the Stokes vector the results from SCIATRAN and from Coulson tables are found to agree within 0.07%. This is similar to the results presented by Kotchenova et al. [19] who have reported an agreement within 0.1% between the Coulson tables and the results from the 6SV1 model. Very good agreement between the SCIATRAN results and Coulson tables is also observed for the U component of the Stokes vector with the maximum difference of about 0.1% decreasing with the increasing optical thickness. For the Q component the agreement is worse with maximum difference of about 2.3% reached for the optical thickness of 1. As discussed by Natraj et al. [232] the remaining disagreement is caused by the limited precision of the Coulson tables, in particular with respect to the parameter Q. A comparison between SCIATRAN and updated tables published by Natraj et al. [232] (available at http://www.gps.caltech.edu/~vijay/Rayleigh_Scattering_Tables) shows an excellent agreement within seven decimal digits for all relevant components of the Stokes vector. The fourth component of the Stokes vector is not considered in this comparison as it is equal to zero for the Rayleigh scattering (see e.g. [233]).

A similar comparison considering the Mie scattering is performed employing the benchmark results published by Garcia and Siewert [234]. The comparisons are done for the radiance at the top of a plane-parallel homogeneous layer with an optical thickness of 1, single scattering albedo of 0.99, and the Lambertian albedo of the underlying surface of 0.1. The layer is illuminated by an unpolarized light with an incidence angle of about 78.5° . The scattering matrix and Greek constants are adopted from Vestrucci and Siewert [235] (their test problem II). The comparison shows a very good agreement between the SCIATRAN results and those published by Garcia and Siewert with the maximum difference of less than 0.01% for all components of the Stokes vector.

A further comparison is performed for the Stokes vector at the top of a non-absorbing homogeneous plane-parallel layers underlain by a black surface. The calculations are made with SCIATRAN, PSTAR [28], RAY [230], MYSTIC [51,52], 3DMCPOL [53], SOSVRT [236] and M-VDOM [237,238] radiative transfer models at a solar zenith angle of 60° and three relative azimuth angles (0° , 90° , and 180°). The results are compared for three types of the scattering particles, namely, Rayleigh scattering ($\tau_0 = 0.3262$), aerosol ($\tau_0 = 0.3262$), and cloud particles ($\tau_0 = 5$). A detailed discussion of the obtained results and description of the participating RT models are presented by Kokhanovsky et al. [239]. The comparison reveals a closest agreement between the SCIATRAN and PSTAR models which is also expected because both models employ the same numerical approach to solve VRTE (discrete-ordinates method). In particular, the results for the second component of the Stokes vector (Q) agree to about 0.2% for both the Rayleigh and aerosol scattering and to about 0.5% for the scattering by cloud particles. A similar agreement is also found in comparison between SCIATRAN and SOSVRT models.

The radiance at the top of a plane-parallel vertically inhomogeneous layer calculated with SCIATRAN is compared with the results published by Mishchenko [240] who has considered a classical problem of Rayleigh scattering neglecting the anisotropy effects. The presented benchmark results have an accuracy of four decimal digits. The comparisons are done for a layer illuminated by an unpolarized light with an incidence angle of about 26° . The optical thickness of the layer is 1, its underlying surface albedo is zero, and the single scattering albedo is set in accordance with $\omega_0 = \exp(-a\tau)$, where the optical depth τ is measured from the upper boundary of the layer and a is a given constant. For $a=0$ the problem simplifies to the conservative scattering in a vertically homogeneous medium. In this case the agreement within ± 1 of the last decimal unit is obtained. For an inhomogeneous layer ($a > 0$) the agreement is affected by the number of sub-layers used in SCIATRAN to describe the vertical inhomogeneity. In particular, for $a=0.1$, 20 sub-layers are needed to obtain an agreement within $\pm (1-2)$ of the last decimal unit. The number of the sub-layers required to keep the same level of agreement increases with the inhomogeneity of the layer. In particular, for $a=1$ (ω_0 varies from 1 at the top to ~ 0.37 at the bottom) 40 sub-layers need to be used in SCIATRAN.

12.2. Reflection by snow and ocean surfaces

In the framework of SCIATRAN a snow surface is modeled as an ice cloud layer with a very small geometrical thickness, zero bottom height and very large optical thickness which overlay a Lambertian surface (see Section 7.2 for details). The reflection from a snow surface modeled with SCIATRAN is compared with the results from the vector code provided by Mishchenko and Dlugach (private communications), which is based on the solution of the Ambarzumian equations [91] for the reflection from an optically semi-infinite medium. The calculations are performed at a solar zenith angle of about 37° and five relative azimuthal angles (0° , 60° , 90° , 120° , and 180°) assuming a single scattering albedo of 0.95 and an optical thickness of the layer of 50 000. The scattering matrix is calculated for a wavelength of 550 nm assuming a gamma distribution of spherical particles with a mode radius of $0.35 \mu\text{m}$ (see Eq. (88)) and a refractive index of 1.31. The I, Q, and U components of the Stokes vector resulting from SCIATRAN (lines) and calculated by Mishchenko and Dlugach (symbols) are shown in Fig. 16 revealing a very good agreement between the results.

For an ocean surface comparisons between the SCIATRAN and SO models [224,20] are performed in exactly the same way as discussed in Section 11.1.1 but accounting for the polarization of light. A comparison for the sun-normalized first component of the Stokes vector (see Eq. (153)) is presented in Fig. 17. The upper and lower panels show results for a black and an ocean underlying surface, respectively. The SCIATRAN results are presented in the left panels while the right panels show the percentage differences between the SCIATRAN and SO models. Similar to the scalar case (see Fig. 13) the glint effect is clearly seen for the reflection from an ocean surface (lower left panel).

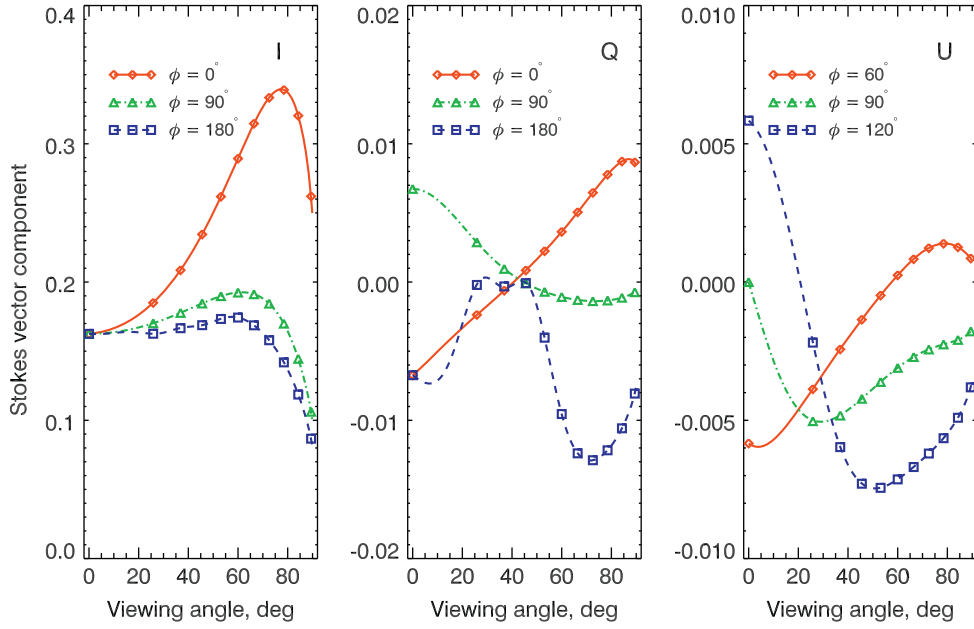


Fig. 16. Components of the Stokes vector (I, Q, and U) resulting from the SCIATRAN model (lines) and calculated by Mishchenko and Dlugach employing Ambarzumian equations (symbols). The calculations are performed at a solar zenith angle of about 37° and different relative azimuth angles assuming a single scattering albedo of 0.95 and an optical thickness of the layer of 50 000.

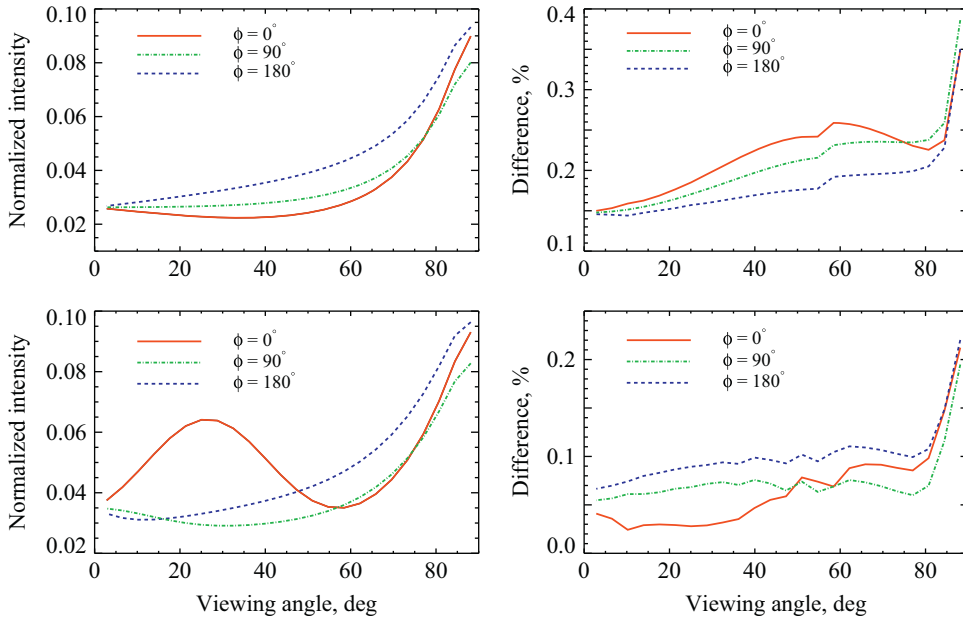


Fig. 17. Sun-normalized first component of the Stokes vector at the top of the atmosphere calculated with SCIATRAN (left panels) and percentage differences between the SCIATRAN and SO models (right panels). The calculations are done at a solar zenith angle of 25.1° for a black (upper panels) and ocean (lower panel) underlying surfaces.

The relative differences between both models are also similar to those for the scalar case. In particular, for a black underlying surface the models agree within 0.25% at viewing angles below about 85° while for an ocean surface the relative differences of less than 0.1% are observed at viewing angles below 80° .

12.3. Spherical atmosphere

For a spherical atmosphere the I, Q, and U components of the Stokes vector at the top of the atmosphere calculated with SCIATRAN, MYSTIC [51,52] and SIRO [55] radiative transfer models are compared. The comparisons

are made at wavelengths of 325, 450, and 765 nm for a viewing geometry typical for limb observations with the SCIAMACHY instrument [83,84]. A pure Rayleigh atmosphere (no absorption) with a black underlying surface is assumed.

The comparison results are summarized in Fig. 18. The SIRO results are not shown because of a very close agreement between the SIRO and MYSTIC models. The upper panels of Fig. 18 show the sun-normalized I, Q and U components of the Stokes vector at a wavelength of 325 nm and two selected solar zenith and relative azimuth angles (ϑ_0, φ). The same Stokes vector components obtained in the single scattering approximation are shown by the dotted lines revealing the significance of the multiple scattering contribution in all considered cases. While the single scattering results from SCIATRAN and MYSTIC are found to agree within 0.5% (not shown here), higher relative differences are observed for the Stokes vector components calculated accounting for the multiple scattering effects. The latter are illustrated in the lower panels of Fig. 18. The observed differences can be explained by the usage of the approximative spherical CDI solver within the SCIATRAN model (see Section 5.9). As reported in previous validation studies [226], for the first component of the Stokes vector this approximation results in an error increasing with the tangent height. This behavior is also

seen for the relative differences to MYSTIC shown in the lower left panel of Fig. 18.

The relative differences in the second Stokes vector component shown in the lower middle panel of Fig. 18 depend strongly on the observational geometry. While at smaller solar zenith angles and larger relative azimuth angles the difference between the results from SCIATRAN and from MYSTIC is below 1%, it increases to 1.5–5.5% for $\vartheta_0 = 47.3^\circ$ and $\varphi = 34.4^\circ$. For larger solar zenith angles and smaller relative azimuth angles it exceeds 10% (not shown here). This significant increase in the approximation error can be explained by a very small contribution of the single scattering (see dotted blue line in the upper middle panel). The relative differences between SCIATRAN and MYSTIC results for the U component of the Stokes vector are shown in the right panel of Fig. 18. Here, the impact of the observation geometry on the approximation error is much weaker and the results agree to better than 3% for all considered cases.

13. Selected comparisons with experimental data

While comparisons with other radiative transfer models or benchmark results, which are usually performed employing significant simplifications, verify the implementation of

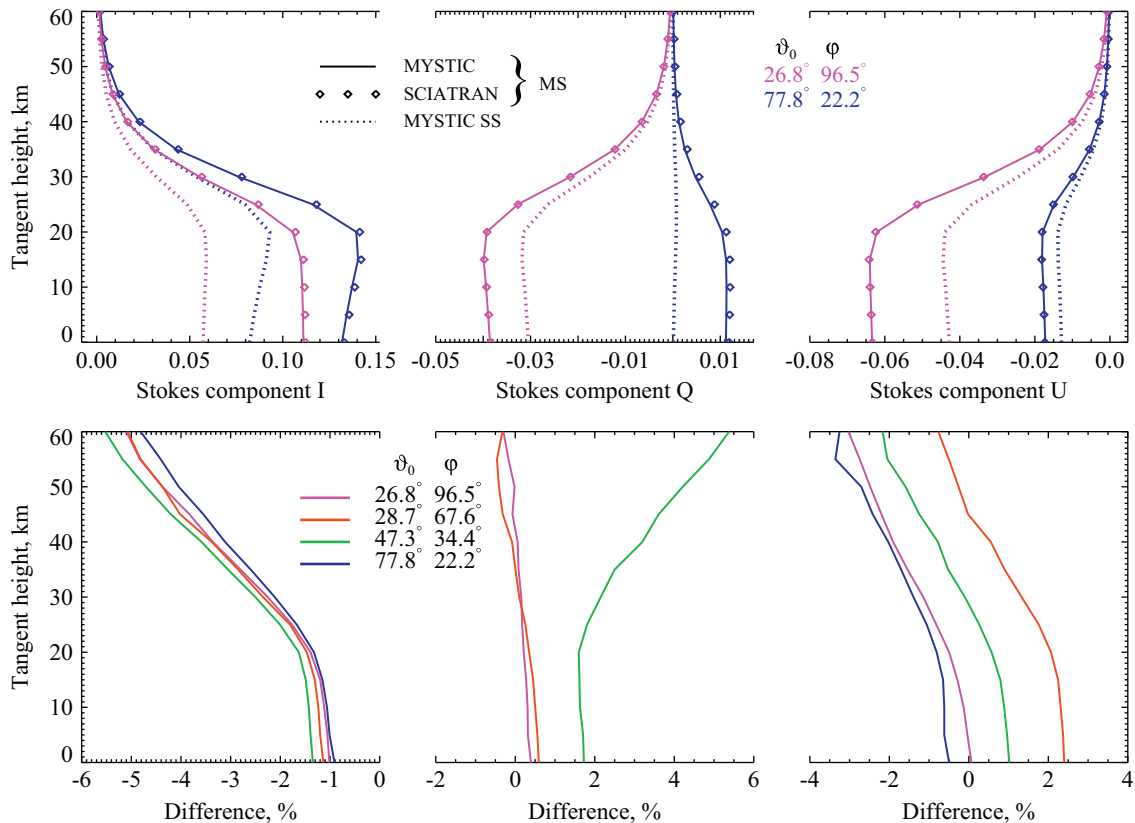


Fig. 18. Comparison between SCIATRAN and MYSTIC results for a limb viewing geometry. Upper panels: sun-normalized components of the Stokes vector at 325 nm calculated with MYSTIC (solid lines) and SCIATRAN (symbols) models for two selected solar zenith and relative azimuth angles. The MYSTIC results obtained in the single scattering approximation are shown by the dotted lines. Lower panels: relative difference between the SCIATRAN and MYSTIC results.

various radiative transfer modules, only comparison with measurement results can assure that all physical processes are properly accounted for. For this reason selected comparisons of the SCIATRAN modeling results with measurements from satellite, ground-based, and in situ instruments are presented in this section. Unless atmospheric and surface parameters needed for the radiative transfer modeling are known from the measurements, the main parameters are estimated employing a retrieval technique and an a priori knowledge is used for the others. The comparison is considered as successful if an acceptable agreement between the simulated and measured spectra is obtained and the estimated parameter values are physically reasonable. Although validation of the retrieved parameters is outside the scope of this study, validation papers are cited where appropriate.

13.1. Space-borne measurements of the spectral reflectance over the ocean by MERIS and AATSR instruments

In this section the SCIATRAN model is used to simulate the spectral reflectance (see Eq. (135)) at the top of the atmosphere underlain by an ocean surface as measured by MERIS (Medium Resolution Imaging Spectrometer) [241] and AATSR (Advanced Along-Track Scanning Radiometer) [242] space-borne instruments on board ENVISAT. For both instruments selected measurements performed over the Pacific Ocean at clear sky conditions are modeled. The measurements made on May 1, 2006 and September 18, 2006 with footprint coordinates of 28.08°N, 177.41°W and 28.34°N, 177.35°W, respectively, are selected for both MERIS and AATSR. The AERONET station located at the Midway island (28.21°N, 177.378°W, 20 m above sea level) provides independent information about the phase function and optical thickness of the aerosol.

The simulations are done with the scalar version of SCIATRAN employing the Buiteveld et al. [212] parameterization to describe the scattering coefficient of the pure water and the Kopelevich model [217] for the scattering by the particulate matter (see Section 8.2 for details). The bidirectional reflectance distribution function of an ocean surface is calculated accounting for the Fresnel reflection, water leaving radiance and whitecaps (see Section 7.3). The wave slope distribution is described by the Gram-Charlier PDF with the parameters adopted from [199] (see

Section 7.3.1). The viewing geometry is set in accordance to that of the selected satellite measurements with solar zenith angles of 27.46° and 36.08°, viewing angles of 12.34° and 12.42°, as well as relative azimuth angles of 170.06° and 133.20° for the measurements on May 1 and September 18, respectively. The phase function and optical thickness of the aerosol provided by the AERONET station and the total column of ozone from MERIS (275 DU) are used. The integral water vapor concentration is set to 2 g/cm². The wind azimuth is 36.75° on May 1 and 43.2° on September 18. Because of missing sources for a reliable information, some parameters need to be fitted. The retrieved values are listed below with the first value referring to the May 1 and the second to the September 18 measurements:

- chlorophyll concentration: 0.075 and 0.15 mg/m³;
- wind speed: 3.7 and 5.6 m/s;
- volume concentration of small particles (v_s in Eq. (134)): 0.047 ppm for both days;
- volume concentration of large particles (v_l in Eq. (134)): 0.01 and 0.02 ppm.

The spectral reflectances measured by MERIS and AATSR and simulated with SCIATRAN are presented in Fig. 19. The plot reveals that between 400 and 900 nm measurements from both MERIS and AATSR are well reproduced by SCIATRAN. The relative differences between the MERIS results and SCIATRAN simulations are found to be within 2% which is comparable with the radiometric accuracy of the MERIS instrument (less than 2% for the sun-normalized radiance, see <http://envsat.esa.int/handbooks/meris/>). A significant difference between AATSR data and SCIATRAN simulation observed at 1.6 μ m is most probably due to the fact that the AERONET aerosol optical thickness is not available at this wavelength and the SCIATRAN model is initialized by an extrapolated value.

The chlorophyll concentration and wind speed estimated to obtain the best match of the measured and modeled spectra are found to be in a reasonable agreement with those provided by MERIS. On May 1 the estimated chlorophyll concentration is about 7% higher than that from MERIS while on September 18 both values agree perfectly. The estimated wind speed is about 20%

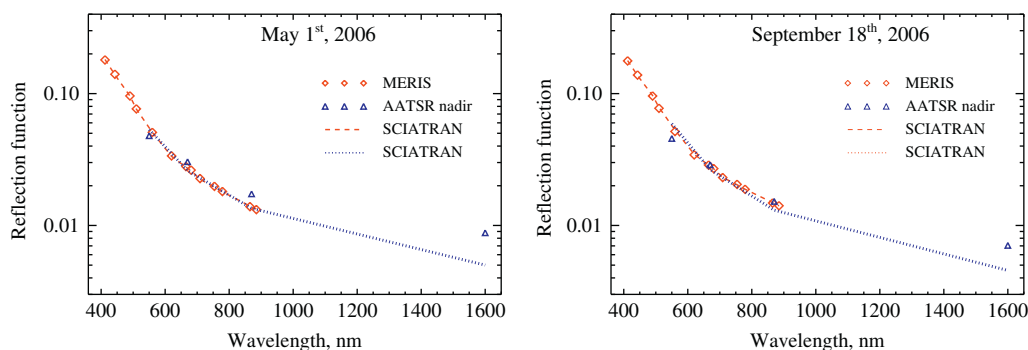


Fig. 19. Spectral reflectance measured by MERIS and AATSR space-borne instruments and modeled with SCIATRAN. Left panel: measurements on May 1, 2006 with footprint coordinates 28.08°N, 177.41°W. Right panel: measurements on September 18, 2006 with footprint coordinates 28.34°N, 177.35°W.

lower on May 1 and about 20% higher on September 18 as compared to the MERIS values. Further comparisons of MERIS observation data to the modeling results from SCIATRAN (both coupled ocean–atmosphere and uncoupled versions) are presented by Blum et al. [227].

13.2. Space-borne measurements of the spectral reflectance over a land surface by the SCIAMACHY instrument

The sun-normalized radiance within the O₂ and CO₂ absorption bands modeled with SCIATRAN is compared with the space-borne observations performed by the SCIAMACHY instrument [83,84] in the nadir viewing geometry. The selected spectral regions are used within the WFM-DOAS [243] and BESD [244] algorithms to retrieve the column densities of CO₂. Both algorithms employ SCIATRAN to perform the forward modeling.

The comparison is performed for a SCIAMACHY observation with the footprint coordinates of 44.51°N, 93.34°W (near Minneapolis, MN, USA) made on June 18, 2006. The SCIATRAN model is initialized with the cloud and aerosol parameters and the Lambertian surface albedo estimated from the SCIAMACHY measurements as described by Reuter et al. [245]. For the selected measurement an ice cloud with an estimated top height of 7.9 km and ice water path of 7.1 g m^{-2} ($\tau_0 \sim 0.23$ at 500 nm) is detected. The sun-normalized intensities at the top of the atmosphere simulated with SCIATRAN and observed by SCIAMACHY are presented in Fig. 20 revealing a very good agreement between the measured and modeled spectra in both spectral windows.

13.3. Ground-based measurements of the snow reflectance

In this section the snow reflectance modeled with SCIATRAN is compared with in situ measurements made on February 9, 2001 (12:00, local time) at Bihoro in eastern Hokkaido. The in situ instrument installed about 1 m above the surface was pointed downwards measuring the radiance reflected from the snow surface at viewing angles from 0° to 85° with a step of 5° and relative azimuthal angles of 0°, 45°, 67°, 90°, 180°, 225°, 247°, and 270°. The measurements were made at clear-sky conditions for a solar zenith angle of 53.5° and air temperature below −10 °C. Details on the experi-

mental setup and measurement procedure are described, e.g. by Kokhanovsky et al. [246].

The snow reflectance at 0.38 μm measured by the in situ instrument and modeled with SCIATRAN is presented in Fig. 21. The SCIATRAN calculations are made for a maritime atmosphere composed of oceanic and water-soluble aerosol (see Section 6.3). No fit is done for any atmospheric or surface parameters.

The color lines depict the SCIATRAN modeling results obtained employing different approximations for the snow surface reflection. The simplest method referred to as the empirical approach uses the modified four-parametric version of the bidirectional reflectance distribution function model suggested by Degünther and Meerkötter [189], see Section 7.2 for details. The results from this approach are depicted by the blue dot-dot-dashed line showing a quite high deviation from the measured values.

A much better approximation of the experimental data is obtained when considering the snow layer as an ice cloud layer. The ice particles are assumed as either fractals or hexagonal prisms with the local optical parameters described in Section 6.4. The calculations are made for a vertically homogeneous snow layer with an optical thickness of 5000. The corresponding results are presented in Fig. 21 by solid red and dot-dashed green lines, respectively. It follows that much better agreement between the simulated and measured data is observed.

The dashed magenta line shows the results from the analytical expression given by Eq. (109) which describes the reflection from an optically semi-infinite non-absorbing snow layer. This approach is referred to as the asymptotic approximation.

In conclusion, Fig. 21 reveals:

- The reflection from a snow layer is significantly underestimated when using the empirical model for the bidirectional reflectance distribution function from [189]. This is most probably because the parameters of the empirical model have been obtained for a snow containing impurities.
- The asymptotic approximation [191] shows much better agreement with measurements than the empirical model. The snow reflectance at viewing angles below about 50° is, however, systematically overestimated.

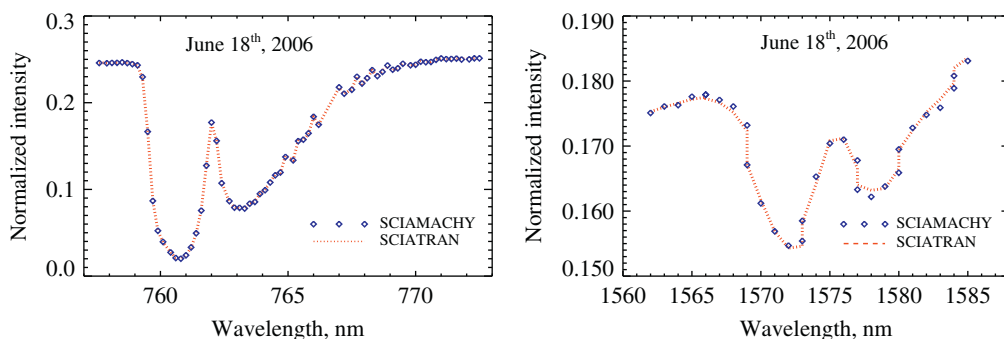


Fig. 20. Sun-normalized intensity at the top of the atmosphere simulated with SCIATRAN and measured by the SCIAMACHY instrument in nadir viewing geometry. The comparison is done for an observation with footprint coordinates of 44.51°N, 93.34°W performed on June 18, 2006. The spectral ranges corresponding to the O₂-A absorption band centered at ~762 nm and the CO₂ absorption band centered at ~1575 nm are shown in the left and right panels, respectively.

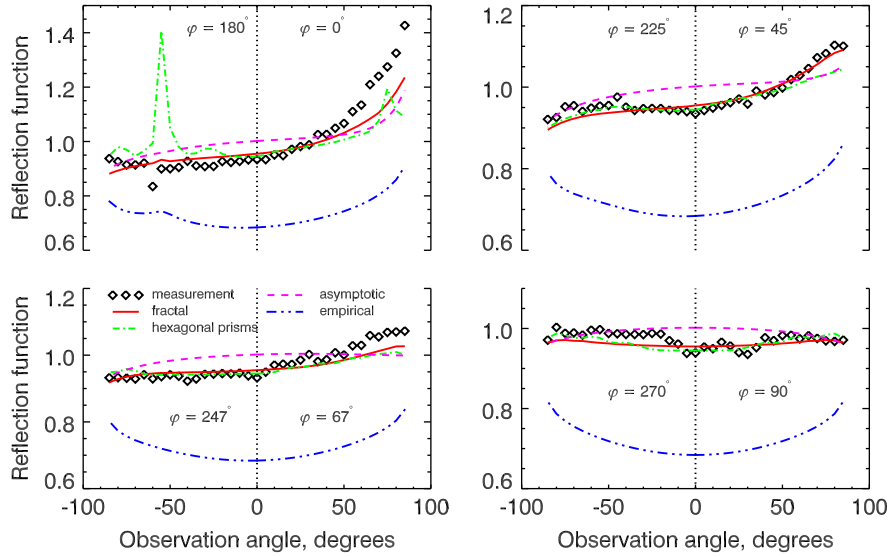


Fig. 21. Snow reflectance at 380 nm at a solar zenith angle of 53.5° measured by an in situ instrument (black symbols) and modeled with SCIATRAN (color lines). Results from different approximations used within SCIATRAN are shown by different colors (see text for details). Positive and negative observation angles correspond to different relative azimuthal angles, φ , as shown in plots. (For interpretation of the references to color in this figure caption, the reader is referred to the web version of this article.)

- The best results are obtained by representing the snow layer as an ice cloud and performing the full radiative transfer calculations.
- The agreement between the measured and simulated data is better when ice particles are represented by fractals rather than hexagonal prisms. The latter representation results in characteristic patterns in the forward and backward scattering directions which are not present in the measurements (see upper left panel in Fig. 21).
- At large viewing angles the snow reflectance is underestimated by the model for both forward and backward scattering directions (see upper left plot in Fig. 21). Most probably this is due to the specular reflection from the partially oriented plate-like crystals residing on a top of a real snow surface.

Further comparisons are presented by Kokhanovsky et al. [247], where SCIATRAN simulations are compared with hyperspectral (0.4–1.6 μm spectral range) measurements of the snow surface reflectance in the Swiss Alps.

13.4. Space-borne observations in limb viewing geometry performed by the SCIAMACHY instrument

Scattered solar radiation observed by the SCIAMACHY instrument in limb viewing geometry is compared to the SCIATRAN modeling results for a selected limb measurement with average footprint coordinates of 37.18° , 255.02° made at a solar zenith angle of 61.87° on January 27, 2004. The comparison is done for a wide spectral range between 600 and 1700 nm. The model calculations are performed using climatological pressure and temperature profiles for January at 35°N resulting from the 2D chemical transport model of the University of Bremen (see Section 6.1). Furthermore, vertical profiles of O_3 and H_2O retrieved

from the SCIAMACHY measurements and background aerosol scenario according to the LOWTRAN 7 model [60] are used.

The comparison results are presented in Fig. 22 for a tangent height of 12 km. The main plot shows the entire spectral range while two small plots in the corners zoom in the O_2 -A absorption band (lower left) and overlapped H_2O and CO_2 absorption signatures (upper right). The measured spectrum is shown by the blue curve while the green and red curves depict SCIATRAN modeling results for two different scenarios. The results shown by the green curve (further referred to as scenario 1) are obtained for a surface albedo of 0.6 and an aerosol extinction coefficient decreased by 50% with respect to the LOWTRAN background aerosol model. Here, a good agreement with the measurements are observed between 800 and 1100 nm while the measured radiance is underestimated at shorter and overestimated at longer wavelengths. The results shown by the red curve (further referred to as scenario 2) are obtained by increasing the surface albedo to 0.8 and further decreasing the aerosol loading to 20% of the LOWTRAN background aerosol model. In comparison to the scenario 1, this scenario results in an increase of the scattered radiation at the wavelengths below about 750 nm and a decrease at longer wavelengths. In the O_2 -A absorption band spectral region (around 760 nm) zoomed in the lower left corner of Fig. 22 the radiances resulting from both scenarios are similar. However, the scenario 2 results in a deeper minimum of the O_2 absorption signature, i.e. stronger absorption by O_2 . In general, scenario 2 provides much better agreement between the measured and simulated radiances for wavelengths longer than 1.2 μm . The only exception is observed in the H_2O absorption band spectral range around 1.4 μm zoomed in the upper right corner of Fig. 22. Here, the scenario 1 results in a better agreement between 1.35 and

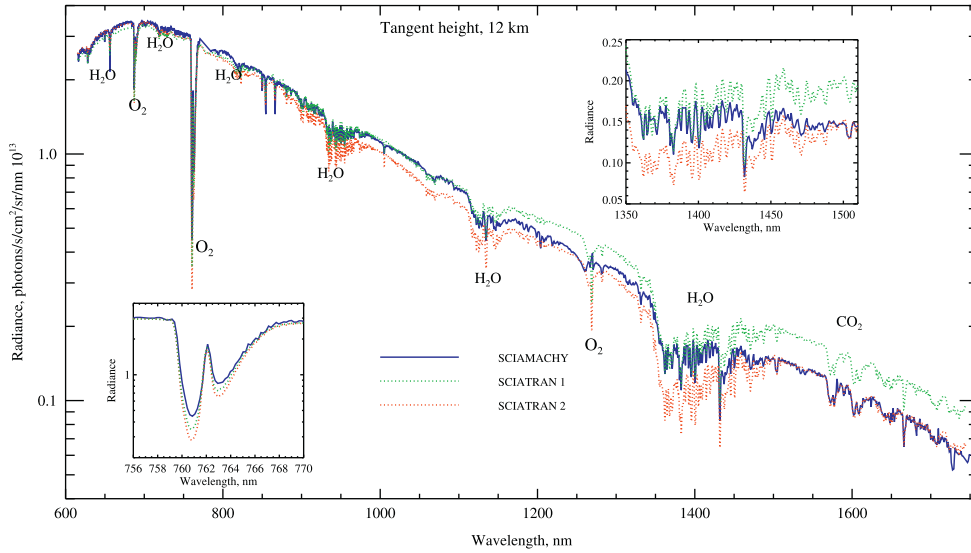


Fig. 22. Scattered solar radiation observed by the SCIAMACHY instrument in limb viewing geometry at a tangent height of 12 km (blue solid line) and modeled with SCIATRAN (dotted green and red lines). The results are shown for a limb measurement with average footprint coordinates of 37.18° , 255.02° made at a solar zenith angle of 61.87° on January 27, 2004. (For interpretation of the references to color in this figure caption, the reader is referred to the web version of this article.)

$1.42 \mu\text{m}$ while at longer wavelengths the results from scenario 2 are closer to the measurements. This is most probably due to the absorption by ice at a snow covered underlying surface which is not included in the simulations. As the selected measurement was made over the Sangre de Cristo Mountains (USA, Colorado and New Mexico States) with the mean elevation above the sea level of about $\sim 2.3 \text{ km}$, the assumption about a snow covered underlying surface is suitable.

In conclusion, both magnitude and general behavior of the spectral radiance with respect to gaseous absorption bands are well described by the SCIATRAN model. Remaining deviations can be explained by an imperfectness of the selected aerosol model and neglected absorption by ice at a snow covered underlying surface.

Besides the comparison presented here, the SCIATRAN model is used at the Institute of Environmental Physics of the University of Bremen as a forward model within the retrieval algorithms routinely used to retrieve vertical distributions of atmospheric trace gases (O_3 , NO_2 , H_2O , BrO) and stratospheric aerosols from the measurements of the scattered solar light performed by the SCIAMACHY instrument in limb viewing geometry. These retrievals have been extensively validated and the validation results can be found elsewhere [248–254].

13.5. Ship-borne measurements of the seawater reflectance

In this section the SCIATRAN radiative transfer model is applied to simulate the measurements of the solar radiation reflected from the ocean surface performed from the research vessel “Sonne” during the “TransBrom-Sonne” campaign. The measurements were made from October 9 to October 24, 2009 in the Pacific Ocean during the cruise from Tomakomai (Japan) to Townsville (Australia) (see <http://www.ifm-geomar.de/index.php?id=transbrom> for

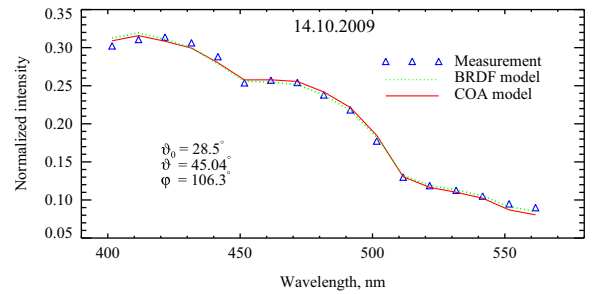


Fig. 23. Normalized intensity of the solar radiation reflected from the ocean surface as measured from the research vessel “Sonne” on October 14, 2009 at 1:48 PM UTC and modeled by SCIATRAN. The measured data are shown by blue triangles while SCIATRAN simulations using the uncoupled and coupled ocean–atmosphere models are depicted by dotted green and solid red lines, respectively. (For interpretation of the references to color in this figure caption, the reader is referred to the web version of this article.)

details). The spectral reflectivity of the ocean surface in the 400–570 nm spectral range was measured by a spectrometer installed at the compass platform of the ship.

A comparison of the observed and simulated radiances is performed for a selected measurement at cloud-free conditions made on October 14, 2009 at 1:48 PM UTC. The instrument line-of-sight was pointed towards the ocean surface at a viewing angle of 45° and azimuthal angle with respect to the ships traveling direction of 45° . Because of a lack of the absolute calibration the comparison is done for the normalized intensity,

$$N_I(\lambda) = \frac{S_{oc}(\lambda)}{S_{zen}(\lambda)}, \quad (154)$$

where $S_{oc}(\lambda)$ and $S_{zen}(\lambda)$ are the spectral signals obtained from the ocean and zenith directions, respectively. The normalized intensities resulting from the measured spectra

and simulated by SCIATRAN are shown in Fig. 23. The blue triangles show the measured data while the lines depict SCIATRAN modeling results from the uncoupled (green) and the coupled ocean–atmosphere radiative transfer models (red). The plot reveals that the absolute values and spectral behavior of the measured data is well reproduced by both models. As the normalized intensity depends only weakly on the atmospheric parameters, in the presented comparison they are set according to the climatological values. In particular, the vertical profiles of pressure, temperature, and trace gas number densities from the Bremen 2D chemical transport model (see Section 6.1) are used, and the aerosol optical thickness at 550 nm is set to 0.17 which corresponds to the maritime aerosol scenario at 50 km visibility from the LOWTRAN aerosol parameterization. In contrast, the concentrations of the chlorophyll and small particles are estimated by applying a fit procedure. When using the uncoupled model this results in 0.081 mg/m³ for the chlorophyll concentration and 0.1 cm³/m³ for the small particles. For the coupled model, concentrations of 0.087 mg/m³ and 0.07 cm³/m³ are obtained for chlorophyll and small particles, respectively. The co-located in situ measurements performed during the “TransBrom-Sonne” campaign report a chlorophyll concentration of 0.078 mg/m³ at 3 m depth (T. Dinter, private communication) which is in a good agreement with the values estimated from the fit procedure.

13.6. Underwater in situ measurements

Underwater distribution of the scattered solar radiation simulated with the coupled ocean–atmosphere model within SCIATRAN is compared to in situ measurements in the lake Pend Oreille (Idaho, USA: 48°N, 116°W)

described by Tyler [255]. The underwater measurements were made at depths from 4 to 61 m by a spectrophotometer equipped with a broadband spectral filter (430–546 nm) centered at 480 nm. The comparison is presented for selected measurements performed on April 28, 1957 at a solar zenith angle of 33.4° at clear-sky and flat-water conditions. A detailed discussion of the measurement data is presented by Duntley [256]. These measurements were also used by Helliwell [257] and Mobley [258] for comparisons with other radiative transfer models.

Angular distributions of the underwater radiance at four selected depths (4.24, 16.6, 41.3, and 66.1 m) measured by the in situ instrument and modeled by SCIATRAN are shown in Fig. 24. The plot reveals that the general behavior of the observed angular distributions of the underwater radiance is well reproduced by the SCIATRAN model for both upwelling and downwelling radiances. Due to a lack of the absolute calibration the measured data are presented in the detector count units and the model results are converted as follows:

$$N_I(z, \vartheta, \varphi) = I(z, \vartheta, \varphi) \frac{S(z_r)}{I(z_r)}, \quad (155)$$

where $I(z_r)$ and $I(z, \vartheta, \varphi)$ are the modeled radiances for the zenith and $\{\vartheta, \varphi\}$ directions, respectively, $S(z_r)$ is the measured signal from the zenith direction, and z_r is the depth at which the signal from the zenith direction is obtained (4.25 m in this comparison). The SCIATRAN simulations are performed at 480 nm accounting for the Rayleigh scattering and absorption by O₃ and NO₂ in the overlaying atmosphere. Vertical profiles of pressure, temperature, and trace gas concentrations from Bremen 2D chemical transport model (see Section 6.1) for April at

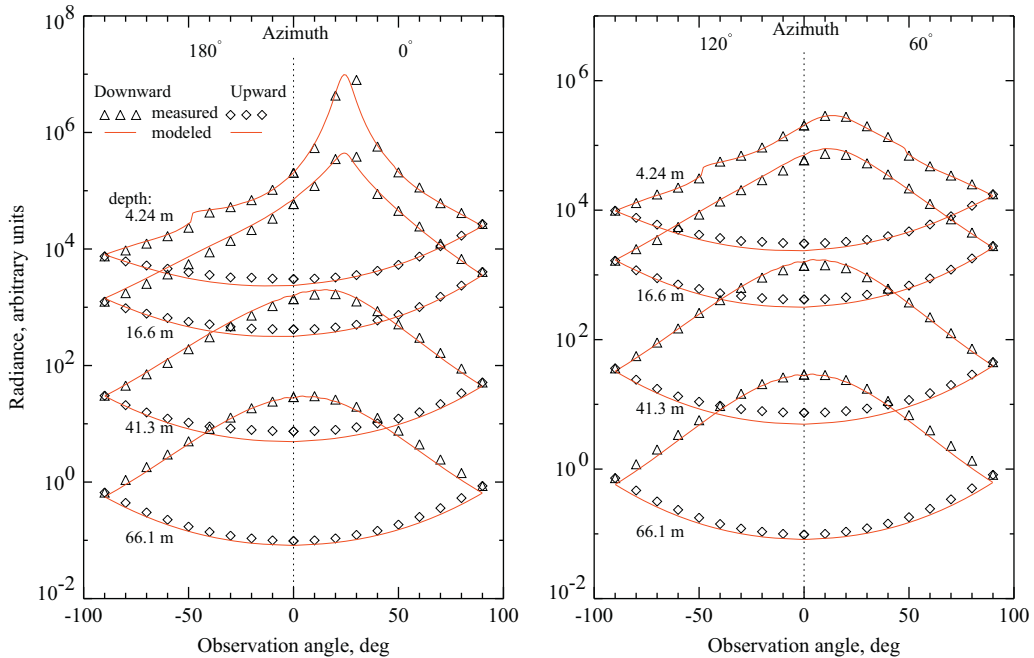


Fig. 24. Underwater radiance distributions measured by an in situ instrument in the Pend Oreille lake (Idaho, USA: 48°N, 116°W) on April 28, 1957 and simulated by SCIATRAN. The measured data is shown by symbols while the solid lines depict the SCIATRAN modeling results. Left panel: measurements in the principal plane. Right panel: measurements in the plane characterized by the relative azimuthal angles 60° and 120°.

45°N are used to initialize the SCIATRAN model. The water extinction coefficient is set in accordance with Tyler [255] to 0.4 m^{-1} just below the surface, to 0.38 m^{-1} at 61 m, and assumed to be constant below. The lake bottom is assumed to be at 225 m depth and to have an Lambertian albedo of 0.1. The single scattering albedo and asymmetry factor of the Henyey–Greenstein phase function describing the particulate scattering in the lake water are varied to obtain the best agreement between the measured and modeled intensities. This is achieved for a single scattering albedo of 0.68 and asymmetry factor of 0.92 independent of the depth.

It is obvious that the distribution of the underwater radiance depends not only on the inherent optical parameters of the water but also on the intensity and angular distribution of the illuminating light. Thus, it is determined by the extinction and scattering properties of the overlying atmosphere. To illustrate the effect of the atmospheric composition, the underwater radiance distribution is calculated for the same conditions as before but including the aerosol scattering in the overlying atmosphere. A background aerosol loading with an aerosol optical thickness of 0.245 at 480 nm according to the LOWTRAN [60] aerosol parameterization is assumed. This simulation results in systematically lower values as compared to the case of the aerosol-free atmosphere. A good agreement with the measured data can be achieved by enhancing the single scattering albedo of the water to 0.72, i.e. by decreasing the absorption by the water. This behavior can be explained considering the radiance distributions just above the water surface, just below the water surface, and at 4.24 m depth modeled with and without aerosols in the overlying atmosphere. These distributions simulated with SCIATRAN are presented in Fig. 25. The plot reveals that the increased scattering due to the presence of aerosols results in an increase of the diffuse radiance just

above and just below the water surface as shown in the left and middle panels of Fig. 25, respectively. At 4.24 m depth, however, a decrease in the downwelling radiance around the vertical direction is observed in the case of the aerosol scattering, see the right panel in Fig. 25. This can be explained by a decrease in the direct solar radiation caused by a stronger attenuation due to the aerosol scattering. Thus, to compensate for this effect the absorption coefficient of the water needs to be reduced.

The considered example demonstrates that an accurate estimation of the inherent optical parameters of the water requires a good knowledge about the scattering properties of the overlaying atmosphere.

14. Conclusions

This paper presents the radiative transfer model SCIATRAN developed to simulate the radiation traveling through the Earth's atmosphere and/or ocean and related radiometric quantities. The model is capable of simulating transmittance, scattering, and surface reflection processes as well as thermal emission and, thus, is suitable for a wide range of applications related to the remote sensing of the Earth's atmosphere. The presented study describes the main features of the model as well as basic principles of the radiative transfer problem and of the methodology how to solve the radiative transfer equation. Furthermore, we consider databases and approximations included in the model which are used to initialize atmospheric and surface parameters. Some selected comparisons with other radiative transfer models as well as with measured data are provided to illustrate the reliability of the SCIATRAN model.

Generally, the SCIATRAN model is targeted at users who do not have an extensive knowledge in the field of radiative transfer but need a model for their particular

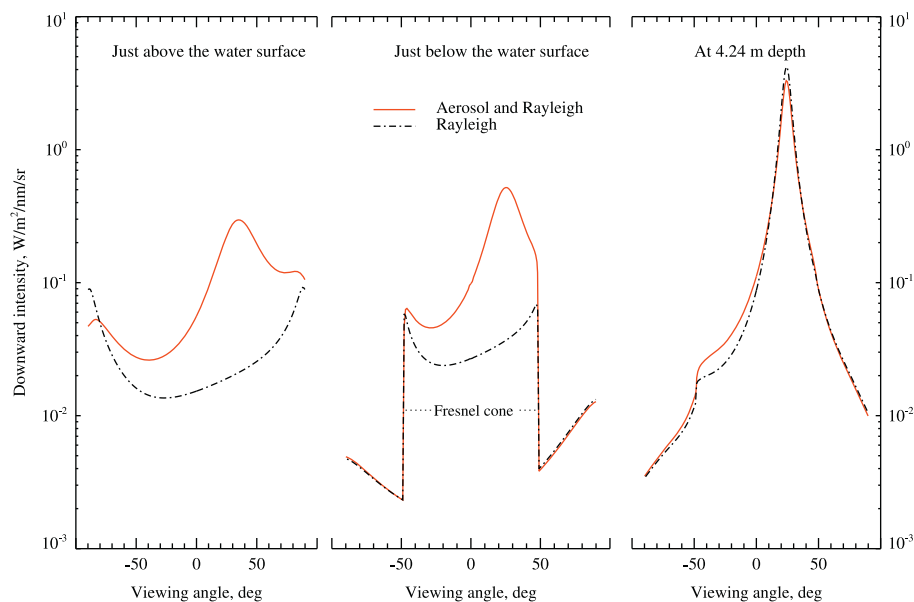


Fig. 25. Downwelling diffuse radiance just above the water surface (left), just below the water surface (middle), and at 4.24 m depth (right) modeled by SCIATRAN with and without aerosols in the overlaying atmosphere.

applications related to remote sensing of the Earth's atmosphere. Owing to the implemented interfaces, default modes, and included databases the SCIATRAN software is much easier to use for non-experts as compared to generic radiative transfer solvers like DISORT or LIDORT. Experienced users might be interested in some new features of the SCIATRAN model such as new approximations for the Planck function and spherical transmission used to obtain the particular solution of the RTE in an analytical form and the iterative technique to solve the boundary value problem for a coupled ocean–atmosphere system.

Although this study is focused on the forward modeling, owing to its linearization the SCIATRAN model also provides the weighting functions (Jacobians) for most atmospheric parameters facilitating its application for solving inverse problems, i.e. for developing retrieval algorithms. Furthermore, the retrieval module incorporated into the SCIATRAN software package provides several pre-configured retrieval schemes which can be applied for solving some common inverse problems. For example, one can retrieve vertical distributions of absorbing species, geometrical and optical parameters of clouds (top and bottom height, optical depth, and liquid/ice water content), aerosol characteristics, and surface reflection properties.

As before, the SCIATRAN software package is freely available for non-commercial usage requiring only a simple registration via the web page of the Institute of Environmental Physics, University of Bremen: <http://www.iup.physik.uni-bremen.de/sciattran>.

Acknowledgments

We are grateful to M.I. Mishchenko for permission to use his Mie code and to include in SCIATRAN the code for the calculation of the oceanic surface reflection matrix including polarization, A. Macke for the use of his ray tracing code, W. von Hoyningen-Huene for help in comparisons with MERIS and AATSR data, F. Zagolski for providing the data derived using the SO code, M. Reuter for providing examples of SCIATRAN and SCIAMACHY comparisons presented in Fig. 20, Y. Ota for the additional explanation of the separation of the specular reflection and transmission components, E.P. Zege, I.L. Katsev and A. S. Prikhach for the provision of results for underwater intensity distributions obtained by employing the RAY code [230], Y. You and G. Kattawar for providing Monte Carlo simulation results reproduced in Fig. 15, V. Kisselev for the helpful discussions of the reflection and transmission properties of a wind-roughened ocean surface, C. Emde, G. Franssens, and P. Liebing for the provision of MYSTIC, SIRO, and SCIATRAN results in limb-viewing geometry including polarization presented in Fig. 18, E. Peters and F. Wittrock for the provision and helpful discussions of seawater reflectance measurements as well as T. Dinter and the Phytooptics group AWI/IUP for providing chlorophyll concentrations measured during the “TransBrom-Sonne” expedition. We are also grateful to A. Schönhardt for helpful discussions. We thank all SCIATRAN users who have sent bug reports to us.

The development and maintenance of the radiative transfer model SCIATRAN since 2007 was in parts financially supported by the State of Bremen, the University of Bremen, the DLR grants for the SCIAMACHY Algorithm Development and Operations Support (FKZ 50 EE 0727, FKZ 50 EE1105) as well ESA SCIAMACHY Quality Working Group, Snow-radiance, and AMARSI projects.

Appendix A. General solution of VRTE

The main purpose of this appendix is to present analytical expressions for the particular solution of the inhomogeneous equation for a source term given in a form of an exponential series (see Eqs. (50) and (58)). To begin with, we briefly discuss how the discrete-ordinates solution is derived. This allows us to introduce all auxiliary vectors and matrices needed to obtain the particular solution in the case under consideration.

A.1. Elementary solutions and separation constants

Following Siewert [36] the Fourier expansion series for the phase matrix defined by Eq. (10) is written as

$$\mathbf{Z}(\mu, \mu', \varphi - \varphi') = \sum_{m=0}^K \sum_{k=1}^2 \mathcal{M}_k^m(\varphi - \varphi') \left[\sum_{l=m}^K \mathbf{P}_l^m(\mu) \mathbf{B}_l \mathbf{P}_l^m(\mu') \right] \mathbf{D}_k, \quad (\text{A.1})$$

where μ and μ' are cosines of polar angles, φ and φ' are azimuthal angles, K is the total number of the Fourier expansion terms, and matrices \mathcal{M}_k^m , \mathbf{P}_l^m , \mathbf{B}_l and \mathbf{D}_k are defined as

$$\mathcal{M}_1^m(\varphi) = (2 - \delta_{0,m}) \text{diag} \{ \cos m\varphi, \cos m\varphi, \sin m\varphi, \sin m\varphi \}, \quad (\text{A.2})$$

$$\mathcal{M}_2^m(\varphi) = (2 - \delta_{0,m}) \text{diag} \{ -\sin m\varphi, -\sin m\varphi, \cos m\varphi, \cos m\varphi \}, \quad (\text{A.3})$$

$$\mathbf{D}_1 = \text{diag} \{ 1, 1, 0, 0 \}, \quad \mathbf{D}_2 = \text{diag} \{ 0, 0, 1, 1 \}, \quad (\text{A.4})$$

$$\mathbf{B}_l = \begin{bmatrix} \alpha_{1,l} & -\beta_{1,l} & 0 & 0 \\ -\beta_{1,l} & \alpha_{2,l} & 0 & 0 \\ 0 & 0 & \alpha_{3,l} & -\beta_{2,l} \\ 0 & 0 & \beta_{2,l} & \alpha_{4,l} \end{bmatrix}, \quad (\text{A.5})$$

$$\mathbf{P}_l^m(\mu) = \begin{bmatrix} P_l^m(\mu) & 0 & 0 & 0 \\ 0 & R_l^m(\mu) & -T_l^m(\mu) & 0 \\ 0 & -T_l^m(\mu) & R_l^m(\mu) & 0 \\ 0 & 0 & 0 & P_l^m(\mu) \end{bmatrix}. \quad (\text{A.6})$$

Here, $\delta_{0,m}$ is the Kronecker delta, the matrix \mathbf{B}_l contains the so-called Greek constants which are the expansion coefficients of the scattering matrix elements (see Eq. (8)) in the generalized spherical functions (see e.g. [9,113] for details) and the elements of matrix $\mathbf{P}_l^m(\mu)$ are expressed in terms of the Wigner d-functions ($d_{l,0}^l(\vartheta)$, $d_{l,2}^l(\vartheta)$, and $d_{l,-2}^l(\vartheta)$) [91]

as follows:

$$P_l^m(\mu) = \sqrt{\frac{(l+m)!}{(l-m)!}} d_{m,0}^l(\vartheta), \quad (\text{A.7})$$

$$R_l^m(\mu) = -\frac{1}{2}(-1)^m [d_{m,2}^l(\vartheta) + d_{m,-2}^l(\vartheta)], \quad (\text{A.8})$$

$$T_l^m(\mu) = -\frac{1}{2}(-1)^m [d_{m,2}^l(\vartheta) - d_{m,-2}^l(\vartheta)]. \quad (\text{A.9})$$

Expanding the Stokes vector of the diffuse radiation field in the Fourier series similar to Eq. (A.1),

$$\mathbf{I}(\tau, \mu, \varphi) = \frac{1}{2} \sum_{m=0}^K \sum_{k=1}^2 \mathcal{M}_{(k-\varphi_0)}^m \mathbf{I}_k^m(\tau, \mu), \quad (\text{A.10})$$

where φ_0 is the solar azimuthal angle and $\mathbf{I}_k^m(\tau, \mu)$ is the m -th Fourier component of the Stokes vector, and substituting Eqs. (A.1) and (A.10) into the radiative transfer equation given by Eq. (17), the following equation of transfer for the m -th Fourier component [36] can be obtained (the derivation is skipped for simplicity reasons):

$$\begin{aligned} \mu \frac{\partial}{\partial \tau} \mathbf{I}_k^m(\tau, \mu) + \mathbf{I}_k^m(\tau, \mu) \\ = \frac{\omega}{2} \sum_{l=m}^K \mathbf{P}_l^m(\mu) \mathbf{B}_l \int_{-1}^1 \mathbf{P}_l^m(\mu') \mathbf{I}_k^m(\tau, \mu') d\mu' + \mathbf{Q}_k^m(\tau, \mu). \end{aligned} \quad (\text{A.11})$$

Taking into account Eqs. (7) and (20) the inhomogeneous source term is written as

$$\begin{aligned} \mathbf{Q}_k^m(\tau, \mu) = \frac{\omega}{2} \sum_{l=m}^K \mathbf{P}_l^m(\mu) \mathbf{B}_l \mathbf{P}_l^m(\mu_0) \mathbf{D}_k \mathbf{I}_1 e^{-\tau/\mu_0} \\ + \delta_{0,m} \delta_{1,k} p(\tau) B(\tau) \mathbf{I}_1, \end{aligned} \quad (\text{A.12})$$

where $p(\tau) = 1 - \omega(\tau)$ and $\delta_{1,k}$ is the Kronecker delta. In the case of the Fresnel reflection from the flat water surface this expression must be extended by an additional term in accordance with Eq. (21).

To obtain the solution of the VRTE formulated above the discrete-ordinates method is used. Omitting Fourier series indices m and k , unless they are explicitly needed, Eq. (A.11) is rewritten in the discrete-ordinates representation as follows:

$$\begin{aligned} \pm \mu_i \frac{d}{d\tau} \mathbf{I}(\tau, \pm \mu_i) + \mathbf{I}(\tau, \pm \mu_i) = \frac{\omega}{2} \sum_{l=m}^K \mathbf{P}_l^m(\pm \mu_i) \mathbf{B}_l \\ \times \sum_{\alpha=1}^N w_\alpha [\mathbf{P}_l^m(\mu_\alpha) \mathbf{I}(\tau, \mu_\alpha) + \mathbf{P}_l^m(-\mu_\alpha) \mathbf{I}(\tau, -\mu_\alpha)] + \mathbf{Q}(\tau, \pm \mu_i), \end{aligned} \quad (\text{A.13})$$

where N is the number of the Gaussian-quadrature points $\{\mu_\alpha\}$ and weights $\{w_\alpha\}$ within the interval $[0, 1]$ and $i = 1, 2, \dots, N$. The homogeneous VRTE is obtained setting $\mathbf{Q}(\tau, \pm \mu_i) = 0$ in Eq. (A.13). The solution of the homogeneous equation can be represented in the following form:

$$\mathbf{I}^h(\tau, \pm \mu_i) = \Phi(\nu, \pm \mu_i) e^{-\tau/\nu}, \quad (\text{A.14})$$

where $\Phi(\nu, \pm \mu_i)$ is $4N \times 1$ vector and ν is an arbitrary constant, which is usually referred to as a separation constant. For a given value of this constant, ν_j , the vector $\Phi(\nu_j, \mu_i) e^{-\tau/\nu_j}$ represents the so-called elementary solution of the homogeneous VRTE (see e.g. [259]). Substituting $\mathbf{I}^h(\tau, \pm \mu_i)$ given by Eq. (A.14) into the homogeneous VRTE

the following equations are obtained for positive and negative μ_i :

$$\left(1 - \frac{\mu_i}{\nu}\right) \Phi(\nu, +\mu_i) = \frac{\omega}{2} \sum_{l=m}^K \mathbf{P}_l^m(\mu_i) \mathbf{B}_l \sum_{\alpha=1}^N w_\alpha \mathcal{F}_{l,\alpha}(\nu), \quad (\text{A.15})$$

$$\left(1 + \frac{\mu_i}{\nu}\right) \mathbf{D} \Phi(\nu, -\mu_i) = \frac{\omega}{2} \sum_{l=m}^K (-1)^{l-m} \mathbf{P}_l^m(\mu_i) \mathbf{D} \mathbf{B}_l \sum_{\alpha=1}^N w_\alpha \mathcal{F}_{l,\alpha}(\nu), \quad (\text{A.16})$$

where both sides of Eq. (A.16) were multiplied by the matrix

$$\mathbf{D} = \text{diag}\{1, 1, -1, -1\} \quad (\text{A.17})$$

and

$$\begin{aligned} \mathcal{F}_{l,\alpha}(\nu) = \mathbf{P}_l^m(\mu_\alpha) \Phi(\nu, \mu_\alpha) \\ + (-1)^{l-m} \mathbf{D} \mathbf{P}_l^m(\mu_\alpha) \mathbf{D} \Phi(\nu, -\mu_\alpha). \end{aligned} \quad (\text{A.18})$$

We note that Eqs. (A.15) and (A.16) were obtained employing the following relationship [36]: $\mathbf{P}_l^m(-\mu_i) = (-1)^{l-m} \mathbf{D} \mathbf{P}_l^m(\mu_i) \mathbf{D}$.

Let us now introduce three auxiliary matrices needed to rewrite Eqs. (A.15) and (A.16) in the vector-matrix form:

$$\mathbf{W} = \text{diag}\{w_1 \mathbf{I}, w_2 \mathbf{I}, \dots, w_N \mathbf{I}\}, \quad \mathbf{M} = \text{diag}\{\mu_1 \mathbf{I}, \mu_2 \mathbf{I}, \dots, \mu_N \mathbf{I}\}, \quad (\text{A.19})$$

$$\mathbf{\Pi}(l, m) = [\mathbf{P}_l^m(\mu_1), \mathbf{P}_l^m(\mu_2), \dots, \mathbf{P}_l^m(\mu_N)]^T, \quad (\text{A.20})$$

where \mathbf{I} is the 4×4 identity matrix, \mathbf{M} and \mathbf{W} are $4N \times 4N$ matrices and $\mathbf{\Pi}(l, m)$ is the $4N \times 4$ matrix. Subsequently, Eqs. (A.15) and (A.16) can be rewritten as

$$\left(1 - \frac{1}{\nu} \mathbf{M}\right) \Phi_+(\nu) = \frac{\omega}{2} \sum_{l=m}^K \mathbf{\Pi}(l, m) \mathbf{B}_l \mathbf{G}_l^m(\nu), \quad (\text{A.21})$$

$$\left(1 + \frac{1}{\nu} \mathbf{M}\right) \Phi_-(\nu) = \frac{\omega}{2} \sum_{l=m}^K (-1)^{l-m} \mathbf{\Pi}(l, m) \mathbf{D} \mathbf{B}_l \mathbf{G}_l^m(\nu), \quad (\text{A.22})$$

where \mathbf{I} is the $4N \times 4N$ identity matrix, and

$$\begin{aligned} \mathbf{G}_l^m(\nu) = \mathbf{\Pi}^T(l, m) \mathbf{W} \Phi_+(\nu) + (-1)^{l-m} \mathbf{D} \mathbf{\Pi}^T(l, m) \mathbf{W} \Phi_-(\nu), \\ \Phi_+(\nu) = [\Phi^T(\nu, +\mu_1), \Phi^T(\nu, +\mu_2), \dots, \Phi^T(\nu, +\mu_N)]^T, \\ \Phi_-(\nu) = [\Phi^T(\nu, -\mu_1) \mathbf{D}, \Phi^T(\nu, -\mu_2) \mathbf{D}, \dots, \Phi^T(\nu, -\mu_N) \mathbf{D}]^T. \end{aligned}$$

To simplify Eqs. (A.21) and (A.22) we introduce

$$\mathbf{U} = \Phi_+(\nu) + \Phi_-(\nu) \quad \text{and} \quad \mathbf{V} = \Phi_+(\nu) - \Phi_-(\nu). \quad (\text{A.23})$$

By making a sum and a difference of Eqs. (A.21) and (A.22) the following relationships are obtained, respectively:

$$\mathbf{E} \mathbf{X} = \frac{1}{\nu} \mathbf{Y}, \quad \mathbf{F} \mathbf{Y} = \frac{1}{\nu} \mathbf{X}, \quad (\text{A.24})$$

where

$$\mathbf{E} = \left(1 - \frac{\omega}{2} \sum_{l=m}^K \mathbf{\Pi}(l, m) \mathbf{B}_l [\mathbf{I} + (-1)^{l-m} \mathbf{D}] \mathbf{\Pi}^T(l, m) \mathbf{W}\right) \mathbf{M}^{-1}, \quad (\text{A.25})$$

$$\mathbf{F} = \left(1 - \frac{\omega}{2} \sum_{l=m}^K \mathbf{\Pi}(l, m) \mathbf{B}_l [\mathbf{I} - (-1)^{l-m} \mathbf{D}] \mathbf{\Pi}^T(l, m) \mathbf{W}\right) \mathbf{M}^{-1}, \quad (\text{A.26})$$

$$\mathbf{X} = \mathbf{M} \mathbf{U}, \quad \mathbf{Y} = \mathbf{M} \mathbf{V}. \quad (\text{A.27})$$

In accordance with Siewert [36] we exclude \mathbf{Y} from Eq. (A.24) to obtain the following eigenvalue problem:

$$\mathbf{F}\mathbf{E}\mathbf{X} = \lambda\mathbf{X}, \quad (\text{A.28})$$

where $\lambda = 1/\nu^2$. The nontrivial solutions of this equation, $\mathbf{X}(\lambda_j)$, and the corresponding values of λ_j ($j = 1, 2, \dots, 4N$) are given by eigenvectors and eigenvalues of the matrix $\mathbf{F}\mathbf{E}$, respectively. The separation constants, $\nu_j = \pm 1/\sqrt{\lambda_j}$, occur in plus-minus pair. Taking into account Eqs. (A.23) and (A.27), we obtain

$$\Phi_{\pm}(\nu_j) = \frac{1}{2}\mathbf{M}^{-1}[\mathbf{X}(\lambda_j) \pm \mathbf{Y}(\lambda_j)]. \quad (\text{A.29})$$

Substituting $\mathbf{Y}(\lambda_j)$ according to Eq. (A.24) this equation results in

$$\Phi_{\pm}(\nu_j) = \frac{1}{2}\mathbf{M}^{-1}(\mathbf{1} \pm \nu_j\mathbf{E})\mathbf{X}(\lambda_j), \quad (\text{A.30})$$

where $j = 1, 2, \dots, 4N$. It follows that $\Phi_{+}(-\nu_j) = \Phi_{-}(\nu_j)$. Thus, the vector $\Phi_{-}(\nu_j)e^{\tau/\nu_j}$ represents yet another elementary solution of the homogeneous equation. It is worth noting that an elementary solution multiplied by an arbitrary constant is also a solution of the homogeneous equation.

A.2. General solution of the homogeneous equation

The general solution of the homogeneous differential equation can be obtained as a linear combination of all possible elementary solutions. Taking into account that separation constants might be complex solution is written as

$$\mathbf{I}_{\pm}^h(\tau) = [\mathcal{D}_{\pm} \mathbf{E}_r(\tau), \text{Re}\{\mathcal{C}_{\pm} \mathbf{E}_c(\tau)\}, \text{Im}\{\mathcal{C}_{\pm} \mathbf{E}_c(\tau)\}]\mathbf{C}, \quad (\text{A.31})$$

where \mathbf{C} is an $8N \times 1$ vector containing arbitrary constants, $\{\mathcal{C}_j\}$. The matrices \mathcal{D}_{\pm} and \mathcal{C}_{\pm} , having dimensions $4N \times 2J_r$ and $4N \times 2J_c$, respectively, are given by

$$\mathcal{D}_{\pm} = \Delta_{\pm}[\Phi_{\pm}(\nu_1), \dots, \Phi_{\pm}(\nu_{J_r}), \Phi_{\mp}(\nu_1), \dots, \Phi_{\mp}(\nu_{J_r})], \quad (\text{A.32})$$

$$\mathcal{C}_{\pm} = \Delta_{\pm}[\Phi_{\pm}(\nu_{J_r+1}), \dots, \Phi_{\pm}(\nu_{J_r+J_c}), \Phi_{\mp}(\nu_{J_r+1}), \dots, \Phi_{\mp}(\nu_{J_r+J_c})], \quad (\text{A.33})$$

where J_r and J_c are the numbers of the real and complex conjugate pairs of separation constants, respectively, $4N \times 1$ vectors $\Phi_{\pm}(\nu_j)$ are given by Eq. (A.30), $\Delta_{-} = \text{diag}\{\mathbf{D}, \mathbf{D}, \dots, \mathbf{D}\}$ is the $4N \times 4N$ matrix with \mathbf{D} defined by Eq. (A.17), and Δ_{+} is the $4N \times 4N$ identity matrix. The diagonal matrices $\mathbf{E}_r(\tau)$ and $\mathbf{E}_c(\tau)$ having dimensions $2J_r \times 2J_r$ and $2J_c \times 2J_c$, respectively, are defined by

$$\mathbf{E}_r(\tau) = \text{diag}\left\{e^{-(\tau-\tau_{l-1})/\nu_1}, \dots, e^{-(\tau-\tau_{l-1})/\nu_{J_r}}, e^{-(\tau_l-\tau)/\nu_1}, \dots, e^{-(\tau_l-\tau)/\nu_{J_r}}\right\}, \quad (\text{A.34})$$

$$\mathbf{E}_c(\tau) = \text{diag}\left\{e^{-(\tau-\tau_{l-1})/\nu_{J_r+1}}, \dots, e^{-(\tau-\tau_{l-1})/\nu_{J_r+J_c}}, e^{-(\tau_l-\tau)/\nu_{J_r+1}}, \dots, e^{-(\tau_l-\tau)/\nu_{J_r+J_c}}\right\}. \quad (\text{A.35})$$

Here, the optical depth, τ , is measured from the top of the medium and τ_{l-1} and τ_l refer to the top and the bottom of the l -th homogeneous layer, respectively.

If all separation constants are real, Eq. (A.31) for the general solution of the homogeneous differential equation

simplifies to

$$\begin{aligned} \mathbf{I}_{\pm}^h(\tau) &= [\mathcal{D}_{\pm} \mathbf{E}_r(\tau)]\mathbf{C} \\ &= \Delta_{\pm} \sum_{j=1}^{4N} [C_j \Phi_{\pm}(\nu_j) e^{-(\tau-\tau_{l-1})/\nu_j} + C_{4N+j} \Phi_{\mp}(\nu_j) e^{-(\tau_l-\tau)/\nu_j}]. \end{aligned} \quad (\text{A.36})$$

In the scalar case it results in

$$\mathbf{I}_{\pm}^h(\tau) = \sum_{j=1}^N [C_j \Phi_{\pm}(\nu_j) e^{-(\tau-\tau_{l-1})/\nu_j} + C_{N+j} \Phi_{\mp}(\nu_j) e^{-(\tau_l-\tau)/\nu_j}]. \quad (\text{A.37})$$

A.3. Particular solution of the inhomogeneous equation

A brief review of various approaches to obtain particular solution of the plane-parallel VRTE has been presented among others by Qin et al. [260]. In the SCIATRAN model the most general technique based on the infinite-medium Green's function [259] is employed (see below for details). Because of the symmetry of the double-Gauss schema adopted in SCIATRAN, a specific version of the particular solution derived by Siewert [35,36] has been preferred.

To obtain a particular solution of the inhomogeneous equation following the infinite-medium Green's functions technique one needs first to obtain expressions for the so-called adjoint vectors $\Psi_{\pm}(\nu_j)$ [36]. This is done by solving the eigenvalue problem given by Eq. (A.28) where the matrix \mathbf{B}_l in \mathbf{E} and \mathbf{F} matrices is replaced by \mathbf{B}_l^T . The solution of this problem is obtained as (derivation details are skipped for simplicity reason)

$$\Psi_{\pm}(\nu_j) = \frac{1}{2}\mathbf{W}^{-1}(\nu_j \mathbf{F}^T \pm \mathbf{1})\mathcal{X}(\lambda_j), \quad (\text{A.38})$$

where $\mathcal{X}(\lambda_j)$ is the left eigenvector of the matrix $\mathbf{F}\mathbf{E}$ corresponding to the eigenvalue λ_j .

Following Siewert [35,36], the particular solution of the inhomogeneous equation, $\mathbf{I}_{\pm}^p(\tau)$, can be written in the general case of complex separation constants as follows:

$$\mathbf{I}_{\pm}^p(\tau) = \Delta_{\pm} \left\{ \sum_{j=1}^{J_r} \mathbf{A}_{\pm}^r(\tau, \nu_j) + 2 \sum_{j=1}^{J_c} [\mathbf{A}_{\pm}^r(\tau, \nu_j) - \mathbf{A}_{\pm}^i(\tau, \nu_j)] \right\}, \quad (\text{A.39})$$

$$\begin{aligned} \mathbf{A}_{\pm}^r(\tau, \nu_j) &= \text{Re} \mathbf{A}_j(\tau_{l-1}, \tau) \text{Re} \Phi_{\pm}(\nu_j) \\ &\quad + \text{Re} \mathbf{B}_j(\tau, \tau_l) \text{Re} \Phi_{\mp}(\nu_j), \end{aligned} \quad (\text{A.40})$$

$$\begin{aligned} \mathbf{A}_{\pm}^i(\tau, \nu_j) &= \text{Im} \mathbf{A}_j(\tau_{l-1}, \tau) \text{Im} \Phi_{\pm}(\nu_j) \\ &\quad + \text{Im} \mathbf{B}_j(\tau, \tau_l) \text{Im} \Phi_{\mp}(\nu_j), \end{aligned} \quad (\text{A.41})$$

where complex coefficients $\mathbf{A}_j(\tau_{l-1}, \tau)$ and $\mathbf{B}_j(\tau, \tau_l)$ are determined by the inhomogeneous source term given by Eq. (A.12). If all separation constants are real (e.g. for pure Rayleigh scattering) the expression for the particular solution can be written in a more simple form:

$$\mathbf{I}_{\pm}^p(\tau) = \Delta_{\pm} \sum_{j=1}^{4N} \mathbf{A}_{\pm}(\tau, \nu_j), \quad (\text{A.42})$$

$$\mathbf{A}_{\pm}(\tau, \nu_j) = \mathbf{A}_j(\tau_{l-1}, \tau) \Phi_{\pm}(\nu_j) + \mathbf{B}_j(\tau, \tau_l) \Phi_{\mp}(\nu_j). \quad (\text{A.43})$$

In the scalar case it simplifies to

$$\mathbf{I}_{\pm}^p(\tau) = \sum_{j=1}^N \mathbf{A}_{\pm}(\tau, \nu_j), \quad (\text{A.44})$$

where $\mathbf{A}_{\pm}(\tau, \nu_j)$ is given by Eq. (A.43) with vectors $\Phi_{\pm}(\nu_j)$ having dimension $N \times 1$ rather than $4N \times 1$ as in the vector case.

The τ -dependent coefficients $\mathbf{A}_j(\tau_{l-1}, \tau)$ and $\mathbf{B}_j(\tau, \tau_l)$ can be obtained by integrating the inhomogeneous source term (see Eq. (A.12)) with the infinite-medium Green's functions. Assuming the inhomogeneous source term can be represented as a product of an optical depth independent $4N \times 1$ vector \mathbf{Q}_{\pm} and a function, $q(\tau)$, of the optical depth, i.e.

$$\mathbf{Q}(\tau, \pm \mu) = \mathbf{Q}_{\pm} q(\tau), \quad \mathbf{Q}_{\pm} = [Q(\pm \mu_1), Q(\pm \mu_2), \dots, Q(\pm \mu_N)]^T, \quad (\text{A.45})$$

the analytical expressions for the coefficients $\mathbf{A}_j(\tau_{l-1}, \tau)$ and $\mathbf{B}_j(\tau, \tau_l)$ are given by the following integrals [36]:

$$\mathbf{A}_j(\tau_{l-1}, \tau) = a_j \int_{\tau_{l-1}}^{\tau} q(x) e^{-(\tau-x)/\nu_j} dx, \quad (\text{A.46})$$

$$\mathbf{B}_j(\tau, \tau_l) = b_j \int_{\tau}^{\tau_l} q(x) e^{-(x-\tau)/\nu_j} dx. \quad (\text{A.47})$$

Here, index j runs from 1 to $4N$,

$$a_j = \frac{1}{N(\nu_j)} [\Psi_+^T(\nu_j) \mathbf{W} \mathbf{Q}_+ + \Psi_-^T(\nu_j) \mathbf{W} \Delta_- \mathbf{Q}_-], \quad (\text{A.48})$$

$$b_j = \frac{1}{N(\nu_j)} [\Psi_-^T(\nu_j) \mathbf{W} \mathbf{Q}_+ + \Psi_+^T(\nu_j) \mathbf{W} \Delta_- \mathbf{Q}_-], \quad (\text{A.49})$$

the normalization factor, $N(\nu_j)$, is given by

$$N(\nu_j) = \Psi_+^T(\nu_j) \mathbf{W} \mathbf{M} \Phi_+(\nu_j) - \Psi_-^T(\nu_j) \mathbf{W} \mathbf{M} \Phi_-(\nu_j), \quad (\text{A.50})$$

\mathbf{W} and \mathbf{M} are $4N \times 4N$ diagonal matrices given by Eq. (A.19) and $\Psi_{\pm}(\nu_j)$ are adjoint vectors defined by Eq. (A.38).

Analytical expressions for integrals in Eqs. (A.46) and (A.47) can be obtained for a given $q(\tau)$ function. In particular, Siewert [36] has presented results for the solar source term in a plane-parallel medium, where $q(\tau) = e^{-\tau/\mu_0}$. In the following subsections we derive analytical expressions for $\mathbf{A}_j(\tau_{l-1}, \tau)$ and $\mathbf{B}_j(\tau, \tau_l)$ coefficients for the solar source term in a spherical atmosphere as defined by Eq. (58) and for the thermal emission source term given by Eq. (50).

A.4. Analytical expressions for the particular solution coefficients

In this subsection we derive analytical expressions for $\mathbf{A}_j(\tau_{l-1}, \tau)$ and $\mathbf{B}_j(\tau, \tau_l)$ coefficients as given by Eqs. (A.46) and (A.47), respectively, assuming the following general dependence of the inhomogeneous source function on the optical depth:

$$q(\tau) = \text{Im} \left\{ \sum_{k=0}^{N_k} q_k e^{-d_k(\tau-\tau_{l-1})} \right\}, \quad (\text{A.51})$$

where N_k is the number of terms needed to approximate the function $q(\tau)$. In particular, this expression provides approximations for the Planck function and for the

spherical transmission function (see Eqs. (50) and (58), respectively) by setting

$$q_k = B_{l-1} a_k, \quad d_k = b_k = b_0 - \frac{ik\pi}{\Delta\tau_l} \quad (\text{A.52})$$

and

$$q_k = T_s(\tau_{l-1}) a_k, \quad d_k = 1/\mu_k = \frac{1}{\mu_e} + \frac{ik\pi}{\Delta\tau_l}, \quad (\text{A.53})$$

respectively.

Real separation constants: Substituting Eq. (A.51) into Eqs. (A.46) and (A.47) and assuming at this point that all separation constants are real, the following expressions for the coefficients are obtained:

$$\mathbf{A}_j(\tau_{l-1}, \tau) = a_j \text{Im} \left\{ \sum_{k=0}^{N_k} q_k \int_{\tau_{l-1}}^{\tau} e^{-d_k(x-\tau_{l-1})} e^{-(\tau-x)/\nu_j} dx \right\}, \quad (\text{A.54})$$

$$\mathbf{B}_j(\tau, \tau_l) = b_j \text{Im} \left\{ \sum_{k=0}^{N_k} q_k \int_{\tau}^{\tau_l} e^{-d_k(x-\tau_{l-1})} e^{-(x-\tau)/\nu_j} dx \right\}, \quad (\text{A.55})$$

where a_j and b_j are defined by Eqs. (A.48) and (A.49), respectively. Performing the integration, Eqs. (A.54) and (A.55) result in

$$\mathbf{A}_j(\tau_{l-1}, \tau) = a_j \text{Im} \left\{ \sum_{k=0}^{N_k} q_k C(\tau-\tau_{l-1}; \nu_j, d_k) \right\}, \quad (\text{A.56})$$

$$\mathbf{B}_j(\tau, \tau_l) = b_j \text{Im} \left\{ \sum_{k=0}^{N_k} q_k e^{-d_k(\tau-\tau_{l-1})} S(\tau_l-\tau; \nu_j, d_k) \right\}, \quad (\text{A.57})$$

where

$$C(\tau-\tau_{l-1}; \nu_j, d_k) = \frac{\nu_j}{\nu_j d_k - 1} [e^{-(\tau-\tau_{l-1})/\nu_j} - e^{-d_k(\tau-\tau_{l-1})}], \quad (\text{A.58})$$

$$S(\tau_l-\tau; \nu_j, d_k) = \frac{\nu_j}{\nu_j d_k + 1} [1 - e^{-(\tau_l-\tau)/\nu_j} e^{-d_k(\tau_l-\tau)}]. \quad (\text{A.59})$$

In the case of the solar source term in a plane-parallel medium, where $d_0 = 1/\mu_0$ and $d_k = 0$ for $k > 0$, expressions (A.58) and (A.59) simplify to those presented by Siewert [36].

Although general expressions for $\mathbf{A}_j(\tau_{l-1}, \tau)$ and $\mathbf{B}_j(\tau, \tau_l)$ contain complex exponents for $k \neq 0$ (see Eqs. (A.52) and (A.53)), their calculation can be avoided if the particular solution of RTE is needed only on the boundaries of the homogeneous layers. Indeed, setting τ either to τ_{l-1} or to τ_l , Eqs. (A.56) and (A.57) result in

$$\mathbf{A}_j(\tau_{l-1}, \tau_{l-1}) = 0, \quad \mathbf{B}_j(\tau_{l-1}, \tau_l) = b_j \text{Im} \left\{ \sum_{k=0}^{N_k} q_k S(\Delta\tau_l; \nu_j, d_k) \right\}, \quad (\text{A.60})$$

$$\mathbf{B}_j(\tau_l, \tau_l) = 0, \quad \mathbf{A}_j(\tau_{l-1}, \tau_l) = a_j \text{Im} \left\{ \sum_{k=0}^{N_k} q_k C(\Delta\tau_l; \nu_j, d_k) \right\}. \quad (\text{A.61})$$

The expressions for $\mathbf{A}_j(\tau_{l-1}, \tau_l)$ and $\mathbf{B}_j(\tau_{l-1}, \tau_l)$ coefficients can now be rewritten to contain only real exponents $e^{-\Delta\tau_l/\nu_j}$ and $e^{-d_0 \Delta\tau_l}$. This is done taking into account the

following relationship:

$$e^{d_k \Delta \tau_l} = e^{d_0 \Delta \tau_l - i k \pi} = e^{d_0 \Delta \tau_l} [\cos(k\pi) - i \sin(k\pi)] = e^{d_0 \Delta \tau_l} (-1)^k. \quad (\text{A.62})$$

It follows that

$$\mathbf{A}_j(\tau_{l-1}, \tau_l) = a_j \sum_{k=0}^{N_k} \text{Im}\{\mathbf{C}_k\} [e^{-\Delta \tau_l / \nu_j} - (-1)^k e^{-d_0 \Delta \tau_l}], \quad (\text{A.63})$$

$$\mathbf{B}_j(\tau_{l-1}, \tau_l) = b_j \sum_{k=0}^{N_k} \text{Im}\{\mathbf{S}_k\} [1 - (-1)^k e^{-\Delta \tau_l / \nu_j} e^{-d_0 \Delta \tau_l}], \quad (\text{A.64})$$

$$\mathbf{C}_k = q_k \nu_j / (\nu_j d_k - 1), \quad \mathbf{S}_k = q_k \nu_j / (\nu_j d_k + 1), \quad (\text{A.65})$$

where only coefficients d_k for $k > 0$ are complex. Introducing generalized real C and S functions as

$$C_k(\Delta \tau_l; \nu_j, d_0) = e^{-\Delta \tau_l / \nu_j} - (-1)^k e^{-d_0 \Delta \tau_l}, \quad (\text{A.66})$$

$$S_k(\Delta \tau_l; \nu_j, d_0) = 1 - (-1)^k e^{-\Delta \tau_l / \nu_j} e^{-d_0 \Delta \tau_l}, \quad (\text{A.67})$$

the final expressions for \mathbf{A}_j and \mathbf{B}_j coefficients are obtained:

$$\mathbf{A}_j(\tau_{l-1}, \tau_l) = a_j \sum_{k=0}^{N_k} \text{Im}\{\mathbf{C}_k\} C_k(\Delta \tau_l; \nu_j, d_0), \quad (\text{A.68})$$

$$\mathbf{B}_j(\tau_{l-1}, \tau_l) = b_j \sum_{k=0}^{N_k} \text{Im}\{\mathbf{S}_k\} S_k(\Delta \tau_l; \nu_j, d_0). \quad (\text{A.69})$$

Complex separation constants: If any separation constants are complex, Eqs. (A.46) and (A.47) for these constants need first to be rewritten for the boundaries of the homogeneous layers. Taking into account Eq. (A.51) this results in

$$\mathbf{A}_j(\tau_{l-1}, \tau_l) = a_j \sum_{k=0}^{N_k} \mathbf{I}_A(k), \quad \mathbf{B}_j(\tau_{l-1}, \tau_l) = b_j \sum_{k=0}^{N_k} \mathbf{I}_B(k), \quad (\text{A.70})$$

where

$$\mathbf{I}_A(k) = \int_{\tau_{l-1}}^{\tau_l} \text{Im}\{q_k e^{-d_k(\tau - \tau_{l-1})}\} e^{-(\tau_l - \tau) / \nu_j} d\tau, \quad (\text{A.71})$$

$$\mathbf{I}_B(k) = \int_{\tau_{l-1}}^{\tau_l} \text{Im}\{q_k e^{-d_k(\tau - \tau_{l-1})}\} e^{-(\tau - \tau_{l-1}) / \nu_j} d\tau. \quad (\text{A.72})$$

Here, d_k for $k \neq 0$, a_j , b_j , and ν_j are complex variables.

The integrals in Eqs. (A.71) and (A.72) can easily be calculated if the imaginary part of the complex exponent is represented as

$$\text{Im}\{q_k e^{-d_k(\tau - \tau_{l-1})}\} = \frac{i}{2} \{q_k^* e^{-d_k^*(\tau - \tau_{l-1})} - q_k e^{-d_k(\tau - \tau_{l-1})}\}, \quad (\text{A.73})$$

where q_k^* and d_k^* are conjugated complex numbers of q_k and d_k , respectively. Substituting (A.73) into Eqs. (A.71) and (A.72) and performing integration the following analytical expressions for $\mathbf{I}_A(k)$ and $\mathbf{I}_B(k)$ are obtained:

$$\mathbf{I}_A(k) = \frac{i}{2} [q_k^* C(\Delta \tau_l; \nu_j, d_k^*) - q_k C(\Delta \tau_l; \nu_j, d_k)], \quad (\text{A.74})$$

$$\mathbf{I}_B(k) = \frac{i}{2} [q_k^* S(\Delta \tau_l; \nu_j, d_k^*) - q_k S(\Delta \tau_l; \nu_j, d_k)], \quad (\text{A.75})$$

where $C(\Delta \tau_l; \nu_j, d_k)$ and $S(\Delta \tau_l; \nu_j, d_k)$ are defined by Eqs. (A.58) and (A.59), respectively.

To obtain the particular solution of the inhomogeneous equation according to Eqs. (A.40) and (A.41), the real and imaginary parts of $\mathbf{I}_A(k)$ and $\mathbf{I}_B(k)$ need to be calculated. This results, e.g. for $\mathbf{I}_A(k)$, in

$$\text{Re}\{\mathbf{I}_A(k)\} = -\frac{1}{2} \text{Im}\{q_k^* C(\Delta \tau_l; \nu_j, d_k^*) - q_k C(\Delta \tau_l; \nu_j, d_k)\}, \quad (\text{A.76})$$

$$\text{Im}\{\mathbf{I}_A(k)\} = \frac{1}{2} \text{Re}\{q_k^* C(\Delta \tau_l; \nu_j, d_k^*) - q_k C(\Delta \tau_l; \nu_j, d_k)\}. \quad (\text{A.77})$$

Substituting $C(\Delta \tau_l; \nu_j, d_k)$ according to Eq. (A.58) and taking into account that (see Eqs. (A.52) and (A.53))

$$\text{Re}\{e^{d_k \Delta \tau_l}\} = \text{Re}\{e^{d_k^* \Delta \tau_l}\} = (-1)^k e^{d_0 \Delta \tau_l}, \quad (\text{A.78})$$

$$\text{Im}\{e^{d_k \Delta \tau_l}\} = \text{Im}\{e^{d_k^* \Delta \tau_l}\} = 0, \quad (\text{A.79})$$

the following relationships are obtained:

$$\text{Re}\{\mathbf{I}_A(k)\} = -\frac{1}{2} \text{Im}\left\{\left[\frac{q_k^* \nu_j}{\nu_j d_k^* - 1} - \frac{q_k \nu_j}{\nu_j d_k - 1}\right] C_k(\Delta \tau_l; \nu_j, d_0)\right\}, \quad (\text{A.80})$$

$$\text{Im}\{\mathbf{I}_A(k)\} = \frac{1}{2} \text{Re}\left\{\left[\frac{q_k^* \nu_j}{\nu_j d_k^* - 1} - \frac{q_k \nu_j}{\nu_j d_k - 1}\right] C_k(\Delta \tau_l; \nu_j, d_0)\right\}, \quad (\text{A.81})$$

where $C_k(\Delta \tau_l; \nu_j, d_k)$ is defined by Eq. (A.66).

The real and imaginary parts of $\mathbf{I}_B(k)$ (see Eq. (A.75)) are obtained in a similar manner resulting in

$$\text{Re}\{\mathbf{I}_B(k)\} = -\frac{1}{2} \text{Im}\left\{\left[\frac{q_k^* \nu_j}{\nu_j d_k^* + 1} - \frac{q_k \nu_j}{\nu_j d_k + 1}\right] S_k(\Delta \tau_l; \nu_j, d_0)\right\}, \quad (\text{A.82})$$

$$\text{Im}\{\mathbf{I}_B(k)\} = \frac{1}{2} \text{Re}\left\{\left[\frac{q_k^* \nu_j}{\nu_j d_k^* + 1} - \frac{q_k \nu_j}{\nu_j d_k + 1}\right] S_k(\Delta \tau_l; \nu_j, d_0)\right\}, \quad (\text{A.83})$$

where $S_k(\Delta \tau_l; \nu_j, d_k)$ is defined by Eq. (A.67).

Summing up all obtained results the real and imaginary parts of the coefficient $\mathbf{A}_j(\tau_{l-1}, \tau_l)$ are written as

$$\text{Re}\{\mathbf{A}_j(\tau_{l-1}, \tau_l)\} = \sum_{k=0}^{N_k} [\text{Re } a_j \text{Re } \mathbf{I}_A(k) - \text{Im } a_j \text{Im } \mathbf{I}_A(k)], \quad (\text{A.84})$$

$$\text{Im}\{\mathbf{A}_j(\tau_{l-1}, \tau_l)\} = \sum_{k=0}^{N_k} [\text{Re } a_j \text{Im } \mathbf{I}_A(k) + \text{Im } a_j \text{Re } \mathbf{I}_A(k)], \quad (\text{A.85})$$

and those of the coefficient $\mathbf{B}_j(\tau_{l-1}, \tau_l)$ as

$$\text{Re}\{\mathbf{B}_j(\tau_{l-1}, \tau_l)\} = \sum_{k=0}^{N_k} [\text{Re } b_j \text{Re } \mathbf{I}_B(k) - \text{Im } b_j \text{Im } \mathbf{I}_B(k)], \quad (\text{A.86})$$

$$\text{Im}\{\mathbf{B}_j(\tau_{l-1}, \tau_l)\} = \sum_{k=0}^{N_k} [\text{Re } b_j \text{Im } \mathbf{I}_B(k) + \text{Im } b_j \text{Re } \mathbf{I}_B(k)]. \quad (\text{A.87})$$

These expressions allow us to calculate the particular solution of the inhomogeneous equation at the top and bottom of a homogeneous layer in accordance with Eqs. (A.39)–(A.41).

Appendix B. Multilayered medium

To obtain the complete discrete-ordinates solution all arbitrary constants in the general solution of the homogeneous VRTE have to be determined. This is usually done by requiring continuity of the solution across boundaries of all homogeneous layers and satisfying boundary conditions. This appendix provides mathematical details on how to formulate the linear algebraic system for a vertically inhomogeneous medium.

Let us assume that a vertically inhomogeneous medium consists of L homogeneous layers. The vertical coordinate is represented by the optical depth and counted from the top to the bottom of the medium. Top boundaries of the homogeneous layers are defined by the following coordinates: $0, \tau_1, \dots, \tau_{L-1}$. The Stokes vector describing the radiation field within the layer “ l ” is represented according to Eq. (39) in the following form:

$$\mathbf{I}_l(\tau) = \mathbf{I}_l^h(\tau) + \mathbf{I}_l^p(\tau), \quad (\text{B.1})$$

where $\mathbf{I}_l^h(\tau)$ is the general solution of the homogeneous equation, $\mathbf{I}_l^p(\tau)$ is a particular solution of the inhomogeneous equation, and $\tau \in [\tau_{l-1}, \tau_l]$. All three vectors in Eq. (B.1) have dimensions of $8N \times 1$, where N is the number of Gaussian-quadrature nodes. The components of the vectors referring to the downward traveling radiation are marked further by “+” while those referring to the upward traveling radiation with “−”:

$$\mathbf{I}_l(\tau) = \begin{bmatrix} \mathbf{I}_l^+(\tau) \\ \mathbf{I}_l^-(\tau) \end{bmatrix}, \quad \mathbf{I}_l^h(\tau) = \begin{bmatrix} \mathbf{I}_l^{h+}(\tau) \\ \mathbf{I}_l^{h-}(\tau) \end{bmatrix}, \quad \mathbf{I}_l^p(\tau) = \begin{bmatrix} \mathbf{I}_l^{p+}(\tau) \\ \mathbf{I}_l^{p-}(\tau) \end{bmatrix}. \quad (\text{B.2})$$

The first term in Eq. (B.1) represents the general solution of the homogeneous equation (see Eq. (A.31)) and is rewritten here in the following form:

$$\mathbf{I}_l^h(\tau) = \begin{bmatrix} \mathbf{I}_l^{h+}(\tau) \\ \mathbf{I}_l^{h-}(\tau) \end{bmatrix} = \begin{bmatrix} \mathcal{H}_l^+(\tau) \\ \mathcal{H}_l^-(\tau) \end{bmatrix} \mathbf{C}_l = \mathcal{H}_l(\tau) \mathbf{C}_l, \quad (\text{B.3})$$

where $8N \times 1$ vector \mathbf{C}_l contains arbitrary constants for the l -th layer and the $8N \times 8N$ matrix $\mathbf{H}_l(\tau)$ is given in accordance to Eq. (A.31) by

$$\mathcal{H}_l(\tau) = \begin{bmatrix} \mathcal{H}_l^+(\tau) \\ \mathcal{H}_l^-(\tau) \end{bmatrix} = \begin{bmatrix} \mathcal{D}_+ \mathbf{E}_r(\tau), \text{Re}\{\mathcal{C}_+ \mathbf{E}_c(\tau)\}, \text{Im}\{\mathcal{C}_+ \mathbf{E}_c(\tau)\} \\ \mathcal{D}_- \mathbf{E}_r(\tau), \text{Re}\{\mathcal{C}_- \mathbf{E}_c(\tau)\}, \text{Im}\{\mathcal{C}_- \mathbf{E}_c(\tau)\} \end{bmatrix}. \quad (\text{B.4})$$

The Stokes vector for the downward radiation in the first homogeneous layer is written then as

$$\mathbf{I}_1^+(\tau) = \mathcal{H}_1^+(\tau) \mathbf{C}_1 + \mathbf{I}_1^{p+}(\tau). \quad (\text{B.5})$$

The upper boundary condition requires the Stokes vector of the incident diffuse radiation to be zero at the top of the medium ($\tau = 0$), i.e. $\mathbf{I}_1^+(0) = 0$. This results in the following algebraic equation for the first layer:

$$\mathcal{H}_1^+(0) \mathbf{C}_1 = -\mathbf{I}_1^{p+}(0). \quad (\text{B.6})$$

Let us now write the Stokes vector for the bottom of the first and the top of the second layer ($\tau = \tau_1$) as

$$\mathbf{I}_1(\tau_1) = \mathcal{H}_1(\tau_1) \mathbf{C}_1 + \mathbf{I}_1^p(\tau_1), \quad (\text{B.7})$$

$$\mathbf{I}_2(\tau_1) = \mathcal{H}_2(\tau_1) \mathbf{C}_2 + \mathbf{I}_2^p(\tau_1). \quad (\text{B.8})$$

Requiring continuity of the Stokes vector across the interface between the first and the second layers, we obtain

$$[\mathcal{H}_1(\tau_1), -\mathcal{H}_2(\tau_1)] \begin{bmatrix} \mathbf{C}_1 \\ \mathbf{C}_2 \end{bmatrix} = \mathbf{I}_2^p(\tau_1) - \mathbf{I}_1^p(\tau_1). \quad (\text{B.9})$$

Similar expressions are to be written for other $L-2$ layer interfaces. In particular, at the interface between the layers l and $l+1$ we have

$$[\mathcal{H}_l(\tau_l), -\mathcal{H}_{l+1}(\tau_l)] \begin{bmatrix} \mathbf{C}_l \\ \mathbf{C}_{l+1} \end{bmatrix} = \mathbf{I}_{l+1}^p(\tau_l) - \mathbf{I}_l^p(\tau_l). \quad (\text{B.10})$$

It follows that the upper boundary condition along with the continuity requirements results in $4N + (L-1) \cdot 8N$ algebraic equations while $L \cdot 8N$ arbitrary constants need to be determined. The remaining $4N$ equations are to be obtained by satisfying the lower boundary condition. To complete the formulation of the linear algebraic system let us write the lower boundary condition in the following general form:

$$\mathcal{B}_d(\tau_L) \mathbf{C}_L = \mathcal{P}_d(\tau_L), \quad (\text{B.11})$$

where contents of the matrix $\mathcal{B}_d(\tau_L)$ and vector $\mathcal{P}_d(\tau_L)$ are determined by the surface reflection properties and will be defined later.

Now the linear algebraic system to determine all $L \cdot 8N$ arbitrary constants can be formulated as follows:

$$\mathcal{N} \mathcal{C} = \mathcal{P}, \quad (\text{B.12})$$

where the $L \cdot 8N \times L \cdot 8N$ block-diagonal matrix \mathcal{N} is given by

$$\begin{bmatrix} \mathcal{N}_u & & & & \\ \mathcal{N}_1 & & \mathbf{0} & & \\ & \mathcal{N}_2 & & & \\ & & \ddots & & \\ & & & \mathcal{N}_{L-2} & \\ & \mathbf{0} & & & \mathcal{N}_{L-1} \\ & & & & \mathcal{N}_d \end{bmatrix}. \quad (\text{B.13})$$

The elements of this matrix are $8N \times 16N$ block-matrices written as

$$\mathcal{N}_u = [\mathcal{H}_1^+(0), \mathbf{0}], \quad (\text{B.14})$$

$$\mathcal{N}_l = [\mathcal{H}_l(\tau_l), -\mathcal{H}_{l+1}(\tau_l)], \quad l = 1, 2, \dots, L-1, \quad (\text{B.15})$$

$$\mathcal{N}_d = [\mathbf{0}, \mathcal{B}_d(\tau_L)]. \quad (\text{B.16})$$

Vector \mathbf{C} contains arbitrary constants for all layers and vector \mathbf{P} represents the right-hand side of the linear algebraic system:

$$\mathbf{C} = \begin{bmatrix} \mathbf{C}_1 \\ \mathbf{C}_2 \\ \mathbf{C}_3 \\ \vdots \\ \mathbf{C}_{L-1} \\ \mathbf{C}_L \end{bmatrix}, \quad \mathbf{P} = \begin{bmatrix} -\mathbf{I}_+^p(0) \\ \mathbf{I}_2^p(\tau_1) - \mathbf{I}_1^p(\tau_1) \\ \mathbf{I}_3^p(\tau_2) - \mathbf{I}_2^p(\tau_2) \\ \vdots \\ \mathbf{I}_L^p(\tau_{L-1}) - \mathbf{I}_{L-1}^p(\tau_{L-1}) \\ \mathbf{P}_d(\tau_L) \end{bmatrix}. \quad (\text{B.17})$$

Both vectors have dimension of $L \cdot 8N \times 1$.

In the following subsections we determine the matrix $\mathbf{B}_d(\tau_L)$ and vector $\mathbf{P}_d(\tau_L)$ for various types of reflecting surfaces.

B.1. Bidirectional reflection

The most general case is represented by a bidirectional surface reflection accounting for the polarization. Here, the appropriate lower boundary condition (see Eq. (93)) is written as follows:

$$\begin{aligned} \mathbf{I}(\tau_0, -\mu, \varphi) &= \mu_0 e^{-\tau_0/\mu_0} \mathbf{R}(-\mu, \mu_0, \varphi - \varphi_0) \mathbf{I}_1 \\ &+ \frac{1}{\pi} \int_0^{2\pi} \int_0^1 \mathbf{R}(-\mu, \mu', \varphi - \varphi') \mathbf{I}(\tau_0, \mu', \varphi') \mu' d\mu' d\varphi', \end{aligned} \quad (\text{B.18})$$

where

$$\mathbf{I}_1 = [1, 0, 0, 0]^T, \quad (\text{B.19})$$

$\mu \in (0, 1]$ is the cosine of the zenith angle, μ_0 is the solar zenith angle, and \mathbf{R} is the surface BRDF including polarization effects. The terms in the right hand side of Eq. (B.18) describe the reflection of the direct solar beam and of the diffuse radiation, respectively.

Applying the separation technique, BRDF is expanded in the Fourier series in the same manner as the phase matrix (see Eq. (A.1)):

$$\mathbf{R}(\mu, \mu', \varphi - \varphi') = \sum_{m=0}^K \sum_{k=1}^2 \mathcal{M}_k^m(\varphi - \varphi') \mathcal{W}^m(\mu, \mu') \mathbf{D}_k, \quad (\text{B.20})$$

where $\mathcal{W}^m(\mu, \mu')$ is the 4×4 expansion coefficient matrix. Substituting BRDF given by (B.20) and the Fourier series expansion for the Stokes vector given by Eq. (A.10) into Eq. (B.18) the lower boundary condition is rewritten as follows:

$$\begin{aligned} \frac{1}{2} \sum_{m=0}^K \sum_{k=1}^2 \mathcal{M}_k^m(\varphi - \varphi_0) \mathbf{I}_k^m(\tau_0, -\mu) \\ = \mu_0 e^{-\tau_0/\mu_0} \sum_{m=0}^K \sum_{k=1}^2 \mathcal{M}_k^m(\varphi - \varphi_0) \mathcal{W}^m(-\mu, \mu_0) \mathbf{D}_k \mathbf{I}_1 \\ + \sum_{m=0}^K \sum_{k=1}^2 \mathcal{M}_k^m(\varphi - \varphi_0) \int_0^1 \mathcal{W}^m(-\mu, \mu') \mathbf{I}_k^m(\tau_0, \mu') \mu' d\mu'. \end{aligned} \quad (\text{B.21})$$

Thus, for each particular Fourier term the lower boundary condition is written as

$$\begin{aligned} \mathbf{I}_k^m(\tau_0, -\mu) &= 2\mu_0 e^{-\tau_0/\mu_0} \mathcal{W}^m(-\mu, \mu_0) \mathbf{D}_k \mathbf{I}_1 \\ &+ 2 \int_0^1 \mathcal{W}^m(-\mu, \mu') \mathbf{I}_k^m(\tau_0, \mu') \mu' d\mu'. \end{aligned} \quad (\text{B.22})$$

As the Earth's atmosphere is illuminated by unpolarized solar radiation, \mathbf{I}_2^m have to be zero for all m and, thus, index k can be omitted. For simplicity reasons, also the Fourier term index m will not be indicated below. Introducing the vector-matrix representation and taking into account that: $\mathbf{D}_1 \mathbf{I}_1 = \mathbf{I}_1$ (see Eqs. (A.4) and (B.19)) we rewrite Eq. (B.22) as follows:

$$\mathbf{I}_-(\tau_0) = 2[\mu_0 e^{-\tau_0/\mu_0} \mathcal{W}_- \mathbf{E}_1 + \mathcal{W}_\pm \mathbf{W} \mathbf{M} \mathbf{I}_+(\tau_0)]. \quad (\text{B.23})$$

Here, the $4N \times 1$ vector \mathbf{E}_1 and $4N \times 4$ matrix \mathbf{W}_- are given by

$$\mathbf{E}_1 = \begin{bmatrix} \mathbf{I}_1 \\ \mathbf{I}_1 \\ \vdots \\ \mathbf{I}_1 \end{bmatrix}, \quad \mathcal{W}_- = \begin{bmatrix} \mathcal{W}(-\mu_1, \mu_0) \\ \mathcal{W}(-\mu_2, \mu_0) \\ \vdots \\ \mathcal{W}(-\mu_N, \mu_0) \end{bmatrix}, \quad (\text{B.24})$$

\mathbf{W} and \mathbf{M} are $4N \times 4N$ matrices defined by Eq. (A.19) containing the Gaussian-quadrature weights and nodes, respectively, and the $4N \times 4N$ matrix \mathcal{W}_\pm is written as

$$\mathcal{W}_\pm = \begin{bmatrix} \mathcal{W}(-\mu_1, \mu_1) & \mathcal{W}(-\mu_1, \mu_2) & \cdots & \mathcal{W}(-\mu_1, \mu_N) \\ \mathcal{W}(-\mu_2, \mu_1) & \mathcal{W}(-\mu_2, \mu_2) & \cdots & \mathcal{W}(-\mu_2, \mu_N) \\ \vdots & \vdots & \cdots & \vdots \\ \mathcal{W}(-\mu_N, \mu_1) & \mathcal{W}(-\mu_N, \mu_2) & \cdots & \mathcal{W}(-\mu_N, \mu_N) \end{bmatrix}. \quad (\text{B.25})$$

Now, both matrix $\mathbf{B}_d(\tau_L)$ and vector $\mathbf{P}_d(\tau_L)$ in the algebraic equation for the lower boundary condition (see Eq. (B.11)) can be easily obtained. Indeed, substituting $\mathbf{I}_-(\tau_0)$ and $\mathbf{I}_+(\tau_0)$ according to Eq. (B.1) into Eq. (B.23), we have

$$\begin{aligned} \mathbf{I}_L^{h-}(\tau_0) - 2\mathcal{W}_\pm \mathbf{W} \mathbf{M} \mathbf{I}_L^{h+}(\tau_0) &= 2\mu_0 e^{-\tau_0/\mu_0} \mathcal{W}_- \mathbf{E}_1 \\ &+ 2\mathcal{W}_\pm \mathbf{W} \mathbf{M} \mathbf{I}_L^{p+}(\tau_0) - \mathbf{I}_L^{p-}(\tau_0). \end{aligned} \quad (\text{B.26})$$

Substituting further vectors $\mathbf{I}_L^{h-}(\tau_0)$ and $\mathbf{I}_L^{h+}(\tau_0)$ according to Eqs. (B.3) and (B.26) is rewritten as

$$\begin{aligned} [\mathcal{H}_L^-(\tau_0) - 2\mathcal{W}_\pm \mathbf{W} \mathbf{M} \mathcal{H}_L^+(\tau_0)] \mathbf{C}_L \\ = 2\mu_0 e^{-\tau_0/\mu_0} \mathcal{W}_- \mathbf{E}_1 + 2\mathcal{W}_\pm \mathbf{W} \mathbf{M} \mathbf{I}_L^{p+}(\tau_0) - \mathbf{I}_L^{p-}(\tau_0). \end{aligned} \quad (\text{B.27})$$

Comparing then this equation to Eq. (B.11) the following relationships for the matrix $\mathbf{B}_d(\tau_L)$ and vector $\mathbf{P}_d(\tau_L)$ are obtained:

$$\mathbf{B}_d(\tau_L) = \mathcal{H}_L^-(\tau_0) - 2\mathcal{W}_\pm \mathbf{W} \mathbf{M} \mathcal{H}_L^+(\tau_0), \quad (\text{B.28})$$

$$\mathbf{P}_d(\tau_L) = 2\mu_0 e^{-\tau_0/\mu_0} \mathcal{W}_- \mathbf{E}_1 + 2\mathcal{W}_\pm \mathbf{W} \mathbf{M} \mathbf{I}_L^{p+}(\tau_0) - \mathbf{I}_L^{p-}(\tau_0). \quad (\text{B.29})$$

B.2. Lambertian surface

In the case of the Lambertian reflection the lower boundary condition is obtained setting the 4×4 matrix $\mathcal{W}(-\mu_i, \mu_j)$ in Eq. (B.25) to

$$\mathcal{W}(-\mu_i, \mu_j) = A \begin{bmatrix} 1 & 0 & 0 & 0 \\ 0 & 0 & 0 & 0 \\ 0 & 0 & 0 & 0 \\ 0 & 0 & 0 & 0 \end{bmatrix}, \quad (\text{B.30})$$

where A is the spherical albedo. Owing to its specific form, the matrix \mathcal{W}_\pm can be represented in the considered case as follows:

$$\mathcal{W}_\pm = A \mathbf{E}_1 \mathbf{E}_1^T. \quad (\text{B.31})$$

Substituting \mathcal{W}_{\pm} given by this equation and $\mathbf{I}_{\pm}(\tau)$ according to Eq. (B.1), the second term in the right-hand side of Eq. (B.23) can be rewritten as follows:

$$\mathcal{W}_{\pm} \mathbf{WMI}_{\pm}(\tau_0) = \mathbf{A} \mathbf{E}_1 \mathbf{E}_1^T \mathbf{WMI}_{\pm}^{h+}(\tau_0) + \mathbf{A} \mathbf{E} \mathbf{E}_1, \quad (\text{B.32})$$

where \mathbf{E} is a scalar given by

$$\mathbf{E} = \mathbf{E}_1^T \mathbf{WMI}_{\pm}^{p+}(\tau_0). \quad (\text{B.33})$$

Now, substituting Eq. (B.32) and $\mathbf{I}_{\pm}(\tau)$ according to Eq. (B.1) into Eq. (B.23), the following equation for the boundary condition is written as

$$\mathbf{I}_L^{h-}(\tau_0) - 2\mathbf{A} \mathbf{E}_1 \mathbf{E}_1^T \mathbf{WMI}_L^{h+}(\tau_0) = 2\mathbf{A}[\mu_0 e^{-\tau_0/\mu_0} + \mathbf{E}] \mathbf{E}_1 - \mathbf{I}_L^{p-}(\tau_0). \quad (\text{B.34})$$

Similar to Eqs. (B.28) and (B.29) the following expressions for the matrix $\mathcal{B}_d(\tau_L)$ and vector $\mathcal{P}_d(\tau_L)$ are obtained then:

$$\mathcal{B}_d^m(\tau_L) = \mathcal{H}_L^-(\tau_0) - 2\mathbf{A} \delta_{0,m} \mathbf{E}_1 \mathbf{E}_1^T \mathbf{WMI}_L^{h+}(\tau_0), \quad (\text{B.35})$$

$$\mathcal{P}_d^m(\tau_L) = 2\mathbf{A} \delta_{0,m} [\mu_0 e^{-\tau_0/\mu_0} + \mathbf{E}] \mathbf{E}_1 - \mathbf{I}_L^{p-}(\tau_0). \quad (\text{B.36})$$

Here, Kronecker's delta, $\delta_{0,m}$, highlights the fact that in the case of the Lambertian reflection only the zeroth term in the Fourier expansion of the reflected Stokes vector is non-zero. It is worth noting that the boundary condition given by Eqs. (B.35) and (B.36) are in line with those derived by Siewert [36].

B.3. Black surface

For a non-reflecting underlying surface the Stokes vector describing the reflected radiation is written as

$$\mathbf{I}_L^-(\tau_L) = \mathbf{I}_L^{h-}(\tau_L) + \mathbf{I}_L^{p-}(\tau_L) = \mathbf{0}. \quad (\text{B.37})$$

Substituting $\mathbf{I}_L^{h-}(\tau_L)$ according to Eq. (B.3) into this equation we obtain

$$\mathcal{H}_L^-(\tau_L) \mathbf{C}_L = -\mathbf{I}_L^{p-}(\tau_L). \quad (\text{B.38})$$

It follows that

$$\mathcal{B}_d(\tau_L) = \mathcal{H}_L^-(\tau_L), \quad \mathcal{P}_d(\tau_L) = -\mathbf{I}_L^{p-}(\tau_L). \quad (\text{B.39})$$

Clearly, these expressions follow also from Eqs. (B.35) and (B.36) if the surface albedo, A , is set to zero.

References

- [1] Lommel E. Die Photometrie der diffusen Zurückwerfung. Sitzber Akad Wissensch München 1887;17:95–132.
- [2] Chwolson OD. Grundzuge einer mathematischen Theorie der inneren Diffusion des Lichtes. Bull Acad Imp Sci St-Petersbourg 1898;33:83–90.
- [3] Rutten RJ. Radiative transfer in stellar atmospheres. Utrecht University lecture notes, 2003.
- [4] Rybicki GB, Lightman AP. Radiative processes in astrophysics. New York: John Wiley and Sons Inc.; 1979.
- [5] Ambartsumian VA. Scientific papers. Erevan: Armenian Academy of Sciences; 1960.
- [6] Chandrasekhar S. Radiative transfer. London: Oxford University Press; 1950.
- [7] Sobolev VV. Light scattering in planetary atmospheres. Oxford: Pergamon Press; 1975.
- [8] van de Hulst HC. Multiple light scattering, vols. 1–2. New York: Academic Press; 1980.
- [9] Hovenier JW, van der Mee C, Domke H. Transfer of polarized light in planetary atmospheres. Basic concepts and practical methods. Dordrecht, Boston, London: Kluwer Academic Publisher; 2004.
- [10] Bell GI, Glasstone S. Nuclear reactor theory. New York: Van Nostrand Reinhold; 1970.
- [11] Case KM, Zweifel PF. Linear transport theory. Addison-Wesley; 1967.
- [12] Howell JR, Siegel R, Menguc MP. Thermal radiation heat transfer. 5th ed Taylor and Francis; 2010.
- [13] Modest MF. Radiative heat transfer. 2nd ed. Academic Press; 2003.
- [14] Hansen JE, Travis LD. Light scattering in planetary atmosphere. Space Sci Rev 1974;16:527–610.
- [15] Uesugi A, Irvine WM. Computation of synthetic spectra for a semi-infinite atmosphere. J Atmos Sci 1969;26:973–8.
- [16] Uesugi A, Irvine WM, Kawata Y. Formation of absorption spectra by diffuse reflection from a semi-infinite planetary atmosphere. J Quant Spectrosc Radiat Transfer 1971;11:797–808.
- [17] Busbridge IW. The mathematics of radiative transfer. Cambridge University Press; 1960.
- [18] Kotchenova SY, Vermote EF, Matarrese R, Klemm FJ. Validation of a vector version of the 6S radiative transfer code for atmospheric correction of satellite data. Part i. Path radiance. Appl Opt 2006;45: 6762–74.
- [19] Kotchenova SY, Vermote EF. Validation of a vector version of the 6S radiative transfer code for atmospheric correction of satellite data. Part II. Homogeneous Lambertian and anisotropic surfaces. Appl Opt 2007;46:4455–64.
- [20] Lenoble J, Herman M, Deuz JL, Lafrance B, Santer R, Tanr D. A successive order of scattering code for solving the vector equation of transfer in the Earth's atmosphere with aerosols. J Quant Spectrosc Radiat Transfer 2007;107:479–507.
- [21] Hansen JE, Hovenier JW. The doubling method applied to multiple scattering of polarized light. J Quant Spectrosc Radiat Transfer 1971;11:809–12.
- [22] Evans KF, Stephens GL. A new polarized atmospheric radiative transfer model. J Quant Spectrosc Radiat Transfer 1991;46:413–23.
- [23] de Haan JF, Bosma PB, Hovenier JW. The adding method for multiple scattering calculations of polarized light. Astron Astrophys 1987;183:371–91.
- [24] Nakajima T, Tanaka M. Matrix formulations for the transfer of solar radiation in a plane-parallel scattering atmosphere. J Quant Spectrosc Radiat Transfer 1986;35:13–21.
- [25] Plass GN, Kattawar GW, Catchings FE. Matrix operator theory of radiative transfer 1: Rayleigh scattering. Appl Opt 1973;12:314–29.
- [26] Fell F, Fischer J. Numerical simulation of the light field in the atmosphere-ocean system using the matrix-operator method. J Quant Spectrosc Radiat Transfer 2001;69:351–88.
- [27] Govaerts Y. RTMOM V0B.11 Users manual. EUMETSAT Report No. EUM/MET/DOC/06/0503, Darmstadt, Germany; 2008.
- [28] Ota Y, Higurashi A, Nakajima T, Yokota T. Matrix formulations of radiative transfer including the polarization effect in a coupled atmosphere-ocean system. J Quant Spectrosc Radiat Transfer 2010;111:878–94.
- [29] Dave JV. A direct solution of the spherical harmonics approximation to the radiative transfer equation for an arbitrary solar elevation. Part I: theory. J Atmos Sci 1975;32:790–8.
- [30] Karp AH, Greenstadt J, Fillmore JA. Radiative transfer through an arbitrarily thick, scattering atmosphere. J Quant Spectrosc Radiat Transfer 1980;24:391–406.
- [31] Lyapustin AI, Muldashev TZ. Method of spherical harmonics in the radiative transfer problem with non-Lambertian surface. J Quant Spectrosc Radiat Transfer 1999;61:545–55.
- [32] Lyapustin A. Radiative transfer code SHARM-3D for radiance simulations over a non-Lambertian nonhomogeneous surface: intercomparison study. Appl Opt 2002;41:5607–15.
- [33] Lyapustin AI. Radiative transfer code SHARM for atmospheric and terrestrial applications. Appl Opt 2005;44:7764–72.
- [34] Stamnes K, Tsay SC, Wiscombe W, Jayaweera K. Numerically stable algorithm for discrete-ordinate-method radiative transfer in multiple scattering and emitting layered media. Appl Opt 1988;27: 2502–9.
- [35] Siewert CE. A concise and accurate solution to Chandrasekhar's basic problem in radiative transfer. J Quant Spectrosc Radiat Transfer 2000;64:109–30.
- [36] Siewert CE. A discrete-ordinates solution for radiative-transfer models that include polarization effects. J Quant Spectrosc Radiat Transfer 2000;64:227–54.
- [37] Schulz FM, Stamnes K. Angular distribution of the Stokes vector in a plane-parallel, vertically inhomogeneous medium in the vector discrete ordinate radiative transfer (VDISORT) model. J Quant Spectrosc Radiat Transfer 2000;65(4):609–20.
- [38] Schulz FM, Stamnes K, Weng F. VDISORT: an improved and generalized discrete ordinate method for polarized (vector) radiative transfer. J Quant Spectrosc Radiat Transfer 1999;61(1):105–22.

- [39] Jin Z, Charlock TP, Rutledge K, Stamnes K, Wang Y. Analytical solution of radiative transfer in the coupled atmosphere–ocean system with a rough surface. *Appl Opt* 2006;45(28):7443–55.
- [40] Ricchiazzi P, Yang S, Gautier C, Sowle D. SBDART: a research and teaching software tool for plane-parallel radiative transfer in the Earth's atmosphere. *Bull Am Meteorol Soc* 1998;79:2101–14.
- [41] Spurr R. LIDORT and VLIDORT: linearized pseudo-spherical scalar and vector discrete ordinate radiative transfer models for use in remote sensing retrieval problems. In: *Light scattering reviews*, vol. 3. Berlin: Springer; 2008. p. 229–75.
- [42] Rozanov VV, Kokhanovsky AA. The solution of the vector radiative transfer equation using the discrete ordinates technique: selected applications. *Atmos Res* 2006;79:241–65.
- [43] Zienkiewicz OC, Taylor RL. *The finite element method*. London: McGraw-Hill; 1989.
- [44] Bulgarelli B, Kisselev V, Roberti L. Radiative transfer in the atmosphere–ocean system: the finite-element method. *Appl Opt* 1999;38(9):1530–42.
- [45] Kisselev V, Roberti L, Perona G. Finite-element algorithm for radiative transfer in vertically inhomogeneous media: numerical schema and applications. *Appl Opt* 1995;34(36):8460–71.
- [46] Barkstrom BR. A finite differencing method of solving anisotropic scattering problems. *J Quant Spectrosc Radiat Transfer* 1976;16:725–39.
- [47] Rozanov VV, Diebel D, Spurr RJD, Burrows JP. GOMETRAN: a radiative transfer model for the satellite project GOME, the plane-parallel version. *J Geophys Res* 1997;102(D14):16683–95.
- [48] Rozanov A, Rozanov V, Burrows JP. A numerical radiative transfer model for a spherical planetary atmosphere: combined differential–integral approach involving the Picard iterative approximation. *J Quant Spectrosc Radiat Transfer* 2001;69(4):491–512. [http://dx.doi.org/10.1016/S0022-4073\(00\)00100-X](http://dx.doi.org/10.1016/S0022-4073(00)00100-X).
- [49] Marchuk GI, Mikhailov GA, Nazaraiev MN. *The Monte Carlo method in atmospheric optics*. Springer; 1980.
- [50] Mikhailov GA. *Optimization of the Monte Carlo weight methods*. Springer; 1992.
- [51] Emde C, Mayer B. Simulation of solar radiation during a total solar eclipse: A challenge for radiative transfer. *Atmos Chem Phys* 2007;7:2259–70.
- [52] Emde C, Buras R, Mayer B, Blumthaler M. The impact of aerosols on polarized sky radiance: model development, validation, and applications. *Atmos Chem Phys* 2010;10:383–96.
- [53] Cornet C, Labonnote LC, Szczap F. Three-dimensional polarized Monte Carlo atmospheric radiative transfer model (3DMCPOL): 3D effects on polarized visible reflectances of a cirrus cloud. *J Quant Spectrosc Radiat Transfer* 2010;111:174–86.
- [54] Postlyakov OP. Linearized vector radiative transfer model MCC++ for a spherical atmosphere. *J Quant Spectrosc Radiat Transfer* 2004;88:297–317.
- [55] Oikarinen L, Sihvola E, Kyrölä E. Multiple scattering radiance in limb-viewing geometry. *J Geophys Res* 1999;104:31261–74.
- [56] Lenoble J, editor. *Radiative transfer in scattering and absorbing atmospheres*. Hampton, VA, USA: A. Deepak Publishing; 1985.
- [57] Emde C, Bil R, Buras R, Faure F, Hamann U, Kylling A, et al. Towards a generic radiative transfer model for the Earth's surface–atmosphere system: Esas-light. Technical Report, ESTEC Contract No AO/1-5433/07/NL/HE; 2008.
- [58] ESAS light, ESTEC Contract No AO/1-5433/07/NL/HE; 2008. URL (<http://esaslight.libradtran.org/internal/Wiki/doku.php?id=rtmodlestable>).
- [59] Rozanov A. Sciattran 3.x: Radiative transfer model and retrieval software package; 2011. URL (<http://www.iup.physik.uni-bremen.de/sciattran>).
- [60] Kneizys FX, Shettle EP, Abreu LW, Chetwynd JH, Anderson GP, Gallery WO, et al. Users Guide to LOWTRAN 7. Technical Report. Environmental research papers, No. 1010, Air Force Geophysics Laboratory; 1986.
- [61] Rahman H, Pinty B, Verstraete MM. Coupled surface–atmosphere reflectance (CSAR) model. 2. Semiempirical surface model usable with NOAA advanced very high resolution radiometer data. *J Geophys Res* 1993;98(D11):20791–801.
- [62] Maignan F, Bréon FM, Lacaze R. Bidirectional reflectance of Earth targets: evaluation of analytical models using a large set of spaceborne measurements with emphasis on the Hot Spot. *Remote Sensing Environ* 2004;90:210–20.
- [63] Roujean JL, Leroy M, Deschamps PY. A bidirectional reflectance model of the Earth's surface for the correction of the remote sensing data. *J Geophys Res* 1992;97(18):20455–68.
- [64] Bréon FM, Vermote E. Correction of MODIS surface reflectance time series for BRDF effects. *Remote Sensing Environ* 2012;125:1–9.
- [65] Vermote E, Justice CO, Breón FM. Towards a generalized approach for correction of the BRDF effect in MODIS directional reflectances. *IEEE Trans Geosci Remote Sensing* 2009;47:898–908.
- [66] He X, Bai Y, Zhu Q, Gong F. A vector radiative transfer model of coupled ocean–atmosphere system using matrix-operator method for rough sea-surface. *J Quant Spectrosc Radiat Transfer* 2010;111:1426–48. <http://dx.doi.org/10.1016/j.jqsrt.2010.02.014>.
- [67] Zhai P-W, Hu Y, Chowdhary J, Trepte CR, Lucker PL, Josset DB. A vector radiative transfer model for coupled atmosphere and ocean systems with a rough interface. *J Quant Spectrosc Radiat Transfer* 2010;111:1025–40.
- [68] Rozanov VV. Adjoint radiative transfer equation and inverse problems. *Light scattering reviews*, vol. 1. Berlin: Springer; 2006. p. 339–92.
- [69] Rozanov VV, Rozanov AV, Kokhanovsky AA. Derivatives of the radiation field and their application to the solution of inverse problems. *Light scattering reviews*, vol. 2. Berlin: Springer; 2007. p. 205–65.
- [70] Box MA, Gerstl SAW, Simmer C. Application of the adjoint formulation to the calculation of atmospheric radiative effects. *Beitr Phys Atmos* 1988;61:303–11.
- [71] Marchuk GI. *Adjoint equations and analysis of complex systems*. Amsterdam: Kluwer Academic Publisher; 1995.
- [72] Ustinov EA. Adjoint sensitivity analysis of radiative transfer equation: temperature and gas mixing ratio weighting functions for remote sensing of scattering atmospheres in thermal IR. *J Quant Spectrosc Radiat Transfer* 2001;68:195–211.
- [73] Landgraf J, Hasekamp O, Box M, Trautmann T. A linearized radiative transfer model for ozone profile retrieval using the analytical forward–adjoint perturbation theory approach. *J Geophys Res* 2001;106(D21):27291–306.
- [74] Hasekamp OP, Landgraf J. A linearized vector radiative transfer model for atmospheric trace gas retrieval. *J Quant Spectrosc Radiat Transfer* 2002;75:221–38.
- [75] Joiner J, Bhartia PK, Cebula RP, Hilsenrath E, McPeters RD, Park H. Rotational Raman scattering (Ring effect) in satellite backscatter ultraviolet measurements. *Appl Opt* 1995;21:4513–25.
- [76] Landgraf J, Hasekamp O, van Deelen R, Aben I. Rotational Raman scattering of polarized light in the earth atmosphere: a vector radiative transfer model using the radiative transfer perturbation theory approach. *J Quant Spectrosc Radiat Transfer* 2004;87:399–433.
- [77] van Deelen R, Landgraf J, Aben I. Multiple elastic and inelastic light scattering in the Earth's atmosphere: a doubling-adding method to include rotational Raman scattering by air. *J Quant Spectrosc Radiat Transfer* 2005;95:309–30.
- [78] Vountas M, Rozanov VV, Burrows JP. Ring effect: impact of rotational Raman scattering on radiative transfer in Earth's atmosphere. *J Quant Spectrosc Radiat Transfer* 1998;60:943–61.
- [79] Wagner T, Beirle S, Deutschmann T. Three-dimensional simulation of the Ring effect in observations of scattered sun light using Monte Carlo radiative transfer models. *Atmos Meas Tech* 2009;2:113–24.
- [80] Mayer B, Kylling A. Technical note: the libRadtran software package for radiative transfer calculations—description and examples of use. *Atmos Chem Phys* 2005;5:1855–77.
- [81] Burrows JP, Weber M, Buchwitz M, Rozanov V, Enmayer AL-W, Richter A, et al. The global ozone monitoring experiment (GOME): mission concept and first scientific results. *J Atmos Sci* 1999;56:151–75.
- [82] Blindauer C, Rozanov V, Burrows JP. Actinic flux and photolysis frequency comparison computations using the model PHOTOGT. *J Atmos Chem* 1996;24(1):1–21.
- [83] Bovensmann H, Burrows JP, Buchwitz M, Frerick J, Noël S, Rozanov VV, et al. SCIAMACHY: mission objectives and measurement modes. *J Atmos Sci* 1999;56(2):127–49.
- [84] Gottwald M, editor. *SCIAMACHY, monitoring the changing Earth's atmosphere*. DLR, Institute für Methodik der Fernerkundung; 2006.
- [85] Rozanov VV, Buchwitz M, Eichmann K-U, de Beek R, Burrows JP. SCIATRAN—a new radiative transfer model for geophysical applications in the 240–2400 nm spectral region: the pseudo-spherical version. *Adv Space Res* 2002;29:1831–5.
- [86] Rozanov A, Rozanov V, Buchwitz M, Kokhanovsky A, Burrows JP. SCIATRAN 2.0—a new radiative transfer model for geophysical applications in the 175–2400 nm spectral region. *Adv Space Res* 2005;36:1015–9. <http://dx.doi.org/10.1016/j.asr.2005.03.012>.
- [87] Rodgers CD. *Inverse methods for atmospheric sounding: theory and practice*. World Scientific; 2000.
- [88] Doicu A, Hilgers S, von Barmen A, Rozanov A, Eichmann K-U, von Savigny C, et al. Information operator approach and iterative

- regularization methods for atmospheric remote sensing. *J Quant Spectrosc Radiat Transfer* 2007;103(2):340–50.
- [89] Hoogen R, Rozanov VV, Burrows JP. Ozone profiles from GOME satellite data: algorithm description and first validation. *J Geophys Res* 1999;104:8263–80. <http://dx.doi.org/10.1029/1998JD100093>.
- [90] Mishchenko MI, Travis LD, Lacis AA. Scattering, absorption, and emission of light by small particles. Cambridge University Press; 2002.
- [91] Mishchenko MI, Travis LD, Lacis AA. Multiple scattering of light by particles. Cambridge: University Press; 2006.
- [92] van de Hulst HC. Light scattering by small particles. NY: John Wiley and Sons, Inc.; 1957.
- [93] Hovenier JW, van der Mee CVM. Fundamental relationships relevant to the transfer of polarized light in a scattering atmosphere. *Astron Astrophys* 1983;25:1–16.
- [94] Lenoble J. Atmospheric radiative transfer. Hampton, VA, USA: A. Deepak Publishing; 1993.
- [95] Pomraning GC. Linear kinetic theory and particle transport in stochastic mixtures. Singapore, New Jersey, London, Hong Kong: World Scientific Publishing; 1991.
- [96] Liou KN. An introduction to atmospheric radiation. 2nd ed. San Diego: Academic Press; 2002.
- [97] Deirmendjian D. Electromagnetic light scattering on spherical polydispersions. Amsterdam: Elsevier; 1969.
- [98] Korn GA, Korn TM. Mathematical handbook for scientists and engineers. New York, San Francisco, Toronto, London, Sydney: McGraw-Hill Book Company; 1968.
- [99] Born M, Wolf E. Principles of optics. 2nd ed. Oxford, London, Edinburgh, New York, Paris, Frankfurt: Pergamon Press; 1964.
- [100] Dave JV, Armstrong BH. Smoothing of the intensity curve obtained from a solution of the spherical harmonics approximation to the transfer equation. *J Atmos Sci* 1974;13(7):1934–7.
- [101] Kourganoff V. In: Basic methods in transfer problems. Oxford: Clarendon Press; 1952.
- [102] Ishimaru A. Wave propagation and scattering in random media. Single scattering and transport theory, vol. 1. Academic Press; 1978.
- [103] Thomas GE, Stamnes K. Radiative transfer in the atmosphere and ocean. Cambridge University Press; 1999.
- [104] Current R, Hilbert D. Methods of mathematical physics, vol. 2. New York: Interscience; 1962.
- [105] Muldashev TZ, Lyapustin AI, Sultangazin UM. Spherical harmonics method in the problem of radiative transfer in the atmosphere–surface system. *J Quant Spectrosc Radiat Transfer* 1999;60:393–404.
- [106] Nakajima T, Tanaka M. Algorithms for radiative intensity calculations in moderately thick atmospheres using a truncation approximation. *J Quant Spectrosc Radiat Transfer* 1988;51–69.
- [107] Rozanov VV, Lyapustin AI. Similarity of radiative transfer equation: error analysis of phase function truncation techniques. *J Quant Spectrosc Radiat Transfer* 2010;111:1964–79.
- [108] Rozanov A. Modeling of radiative transfer through a spherical planetary atmosphere: application to atmospheric trace gases retrieval from occultation- and limb-measurements in UV–Vis–NIR. Germany: Logos Verlag Berlin; 2001.
- [109] Rozanov A, Rozanov V, Burrows JP. Combined differential–integral approach for the radiation field computation in a spherical shell atmosphere: nonlimb geometry. *J Geophys Res* 2000;102:22937–42.
- [110] Siewert CE. On the equation of transfer relevant to the scattering of polarized light. *Astrophys J* 1981;245:1080–6.
- [111] Siewert CE. On the phase matrix basic to the scattering of polarized light. *Astron Astrophys* 1982;109:195–200.
- [112] de Rooij WA. Reflection and transmission of polarized light by planetary atmospheres. PhD thesis. Amsterdam: Free University; 1985.
- [113] de Rooij WA, van der Stap CCAH. Expansion of Mie scattering matrices in generalized spherical functions. *Astron Astrophys* 1984;131:237–48.
- [114] Wauben WMF. Multiple scattering of polarized radiation in planetary atmospheres. Ph.D. thesis. Amsterdam: Free University; 1992.
- [115] Mitrescu C, Stephens GL. On similarity and scaling of the radiative transfer equation. *J Quant Spectrosc Radiat Transfer* 2004;387–94.
- [116] Hu Y-X, Wielicki B, Lin B, Gibson G, Tsay S-C, Stamnes K, et al. δ -Fit: a fast and accurate treatment of particle scattering phase functions with weighted singular-value decomposition least-squares fitting. *J Quant Spectrosc Radiat Transfer* 2000;65:681–90.
- [117] Wiscombe WJ. The Delta-M method: rapid yet accurate radiative flux calculations for strongly asymmetric phase functions. *J Atmos Sci* 1977;34:1408–22.
- [118] Chami M, Santer R, Dilligeard E. Radiative transfer model for the computation of radiance and polarization in an ocean–atmosphere system: polarization properties of suspended matter for remote sensing. *Appl Opt* 2001;40:2398–416.
- [119] Min Q, Duan M. A successive order of scattering model for solving vector radiative transfer in the atmosphere. *J Quant Spectrosc Radiat Transfer* 2004;87:243–59.
- [120] Fu Q, Liou KN. Parameterization of the radiative properties of cirrus clouds. *J Atmos Sci* 1993;50:2008–25.
- [121] Fu Q, Liou KN, Cribb MC, Charlack TP, Grossman A. Multiple scattering parameterization in thermal infrared radiative transfer. *J Atmos Sci* 1997;54:2799–812.
- [122] Kylling A, Stamnes K. Efficient yet accurate solution of the linear transport equation in the presence of internal sources: the exponential-linear-in-depth approximation. *J Comput Phys* 1992;102:265–76.
- [123] Rathke C, Fischer J. Evaluation of four approximate methods for calculating infrared radiances in cloudy atmospheres. *J Quant Spectrosc Radiat Transfer* 2002;75:297–321.
- [124] Wiscombe WJ. Extension of the doubling method to inhomogeneous sources. *J Quant Spectrosc Radiat Transfer* 1976;16:477–89.
- [125] Deluisi JJ, Mateer CL. On the application of optimum statistical inversion technique to the evaluation of Umkehr observations. *J Appl Meteorol* 1971;10:328–34.
- [126] Caudill TR, Flittner DE, Herman BM, Torres O, McPeters RD. Evaluation of the pseudo-spherical approximation for backscattered ultraviolet radiances and ozone retrieval. *J Geophys Res* 1997;102:3881–90.
- [127] Dahlback A, Stamnes K. A new spherical model for computing the radiation field available for photolysis and heating at twilight. *Planet Space Sci* 1991;39:671–83.
- [128] Spurr RJD. Simultaneous derivation of intensities and weighting functions in a general pseudo-spherical discrete ordinate radiative transfer treatment. *J Quant Spectrosc Radiat Transfer* 2002;75:129–75.
- [129] Griffioen E, Oikarinen L. LIMBTRAN: a pseudo three-dimensional radiative transfer model for the limb-viewing imager OSIRIS on the ODIN satellite. *J Geophys Res* 2000;105:29717–30.
- [130] Mueller RW, Bovensmann H, Kaiser JW, Richter A, Rozanov A, Wittrock F, et al. Consistent interpretation of ground based and GOME BrO slant column data. *Adv Space Res* 2002;29:1655–60.
- [131] Gordon HR. Simple calculation of the diffuse reflectance of ocean. *Appl Opt* 1973;12:2803–4.
- [132] Sinnhuber B-M, Sheode N, Sinnhuber M, Chipperfield MP, Feng W. The contribution of anthropogenic bromine emissions to past stratospheric ozone trends: a modelling study. *Atmos Chem Phys* 2009;9:2863–71.
- [133] Chipperfield MP. Multiannual simulations with a three-dimensional chemical transport model. *J Geophys Res* 1999;104:1781–805.
- [134] Bruhl C, Crutzen PJ. MPIC two-dimensional model. In: The atmospheric effects of stratospheric aircraft. NASA Ref Publ 1993;1292:103–4.
- [135] Committee on Extension to the Standard Atmosphere. Washington, DC: U.S. Standard Atmosphere, 1976, Government Printing Office; 1976.
- [136] Lamsal LN, Weber M, Tellmann S, Burrows JP. Ozone column classified climatology of ozone and temperature profiles based on ozonesonde and satellite data. *J Geophys Res* 2004;109 (D20304).
- [137] Wellenmeyer CG, Taylor SL, Seftor CJ, McPeters RD, Bhartia PK. A correction for total ozone mapping spectrometer profile shape errors at high latitude. *J Geophys Res* 1997;102(D7):9029–38.
- [138] Fortuin JPF, Kelder H. An ozone climatology based on ozonesonde and satellite measurements. *J Geophys Res* 1998;103(D24):31709–34.
- [139] Bogumil K, Orphal J, Homann T, Voigt S, Spietz P, Fleischmann OC, et al. Measurements of molecular absorption spectra with the SCIAMACHY pre-flight model: instrument characterization and reference data for atmospheric remote sensing in the 230–2380 nm region. *J Photochem Photobiol A* 2003;157:167–84. [http://dx.doi.org/10.1016/S0010-4655\(02\)00555-6](http://dx.doi.org/10.1016/S0010-4655(02)00555-6).
- [140] Burrows JP, Dehn A, Deters B, Himmelmann S, Richter A, Voigt S, et al. Atmospheric remote-sensing reference data from GOME: 1 temperature-dependent absorption cross sections of NO₂ in the 231–794 nm range. *J Quant Spectrosc Radiat Transfer* 1998;60:1025–31.
- [141] Burrows JP, Richter A, Dehn A, Deters B, Himmelmann S, Voigt S, et al. Atmospheric remote-sensing reference data from GOME: 2. temperature-dependent absorption cross sections of O₃ in the 231–794 nm range. *J Quant Spectrosc Radiat Transfer* 1998;61:509–17.
- [142] Fleischmann OC, Hartmann M, Burrows JP, Orphal J. New ultraviolet absorption cross-sections of BrO at atmospheric temperatures

- measured by time-windowing Fourier transform spectroscopy. *J Photochem Photobiol A* 2004;168:117–32.
- [143] Bass AM, Paur RJ. The ultraviolet cross-section of ozone. I. The measurements. In: Zerefos CS, editor. *Atmospheric ozone: proceedings of the quadrennial ozone symposium*. p. 601–6.
- [144] Minschwaner K, Anderson G, Hall L, Yoshino K. Polynomial coefficients for calculating O_2 Schumann–Runge cross sections at 0.5 cm resolution. *J Geophys Res* 1992;97(D9):10103–8. <http://dx.doi.org/10.1029/92JD00661>.
- [145] Molina LT, Molina MJ. Absolute absorption cross sections of ozone in the 185– to 350-nm wavelength range. *J Geophys Res* 1986;91:14501–8.
- [146] Hearn C, Joens JA. The near UV absorption of CS_2 and SO_2 at 300 K. *J Quant Spectrosc Radiat Transfer* 1991;45:69–75.
- [147] Simon FG, Schneider W, Moortgat GK, Burrows JP. A study of the clo absorption cross-section between 240 and 310 nm and the kinetics of the self-reaction at 300 K. *J Photochem Photobiol A: Chem* 1990;55:1–23.
- [148] Meller R, Moortgat GK. Temperature dependence of the absorption cross sections of formaldehyde between 223 and 323 K in the wavelength range 225–375 nm. *J Geophys Res* 2000;201:7089–101.
- [149] Wahner A, Ravishankara AR, Sander SP, Friedl RR. Absorption cross section of BrO between 312 and 385 nm at 298 and 223 K. *Chem Phys Lett* 1988;152(6):507–12.
- [150] Wilmouth D, Hanisco T, Donahue N, Anderson J. Fourier transform ultraviolet spectroscopy of the $A^2\Pi_{3/2} \leftarrow X^2\Pi_{3/2}$ transition of BrO. *J Phys Chem A* 1999;103:8935–45.
- [151] DeMore WB, Golden DM, Hampson RF, Howard CJ, Kurylo MJ, Molina MJ, et al. Chemical kinetics and photochemical data for use in stratospheric modeling, evaluation number 8, Jpl Publication 87-41. Pasadena, CA: Jet Propulsion Laboratory, California Institute of Technology; 1987.
- [152] Wahner A, Tyndall GS, Ravishankara AR. Absorption cross sections for OClO as a function of temperature in the wavelength range 240–480 nm. *J Phys Chem* 1987;91:2734–8.
- [153] Greenblatt G, Orlando J, Burkholder J, Ravishankara A. Absorption measurements of oxygen between 330 and 1140 nm. *J Geophys Res* 1990;95:18577–82. <http://dx.doi.org/10.1029/JD095iD11p18577>.
- [154] Yoshino K, Cheung AS-C, Esmond JR, Parkinson WH, Freeman DE, Guberman SL, et al. Improved absorption cross sections of oxygen in the wavelength region 205–240 nm of the Herzberg continuum. *Planet Space Sci* 1988;36:1469–75.
- [155] Yoshino K, Esmond JR, Cheung AS-C, Freeman DE, Parkinson WH. High resolution absorption cross sections in the transmission window region of the Schumann–Runge bands and Herzberg continuum of O_2 . *Planet Space Sci* 1992;40:185–92.
- [156] Rothman LS, Gordon IE, Barbe A, ChrisBenner D, Bernath PF, Birk M, et al. The HITRAN 2008 molecular spectroscopic database. *J Quant Spectrosc Radiat Transfer* 2009;110:533–72.
- [157] Buchwitz M, Rozanov V, Burrows J. A correlated-distribution scheme for overlapping gases suitable for retrieval of atmospheric constituents from moderate resolution radiance measurements in the visible/near-infrared spectral region. *J Geophys Res* 2000;105(D12):15247–61. <http://dx.doi.org/10.1029/2000JD900171>.
- [158] Burrows JP, Hölzle E, Goede APH, Visser H, Fricke W. SCIAMACHY—Scanning Imaging Absorption Spectrometer for Atmospheric Characterography. *Acta Astronaut* 1995;35(7):445–51.
- [159] Gottwald M, Bovensmann H, editors. SCIAMACHY, exploring the changing Earth's atmosphere. Springer; 2011.
- [160] Bates DR. Rayleigh scattering by air. *Planet Space Sci* 1984;32(6):785–90.
- [161] Bucholtz A. Rayleigh-scattering calculations for the terrestrial atmosphere. *Appl Opt* 1995;34(15):2765–73.
- [162] Bodhaine BA, Wood NB, Dutton EG, Slusser JR. On Rayleigh optical depth calculations. *J Atmos Ocean Tech* 1999;16:1854–61.
- [163] Dalgarno A, Kingston A. Refractive indices and Verdet constants of the inert gases. *Proc R Soc A* 1960;259:424–9.
- [164] Owens JC. Optical refractive index of air: dependence on pressure, temperature and composition. *Appl Opt* 1967;6:51–9.
- [165] Birch KP, Downs MJ. Correction to the updated Edlen equation for the refractive index of air. *Metrologia* 1994;31:315–6.
- [166] Edlen B. The dispersion of standard air. *J Opt Soc Am* 1953;43:339–44.
- [167] Edlen B. The refractive index of air. *Meteorology* 1966;2:71–80.
- [168] Peck ER, Reeder K. Dispersion of air. *J Opt Soc Am* 1972;62:958–62.
- [169] Bohren CF, Huffman DR. Absorption and scattering of light by small particles. New York: Wiley; 1983.
- [170] Kerker M. The scattering of light and other electromagnetic radiation. San Diego, CA: Academic Press Inc.; 1969.
- [171] Mishchenko MI, Dlugach JM, Yanovitskij EG, Zakharova NT. Bidirectional reflectance of flat, optically thick particulate layers: an efficient radiative transfer solution and applications to snow and soil surfaces. *J Quant Spectrosc Radiat Transfer* 1999;63:409–32.
- [172] Bolle HJ, editor. A preliminary cloudless standard atmosphere for radiation computation, WCP-112. Geneva: World Meteorological Organization; 1986.
- [173] Davies CN. Size distribution of atmospheric particles. *Aerosol Sci* 1974;5:293–300.
- [174] Kauss J. Aerosol-Parametrisierung für Strahlungstransport Simulationen im ultravioleten bis nahinfraroten Spektralbereich. Master's thesis. Institut für Umweltphysik Universität Bremen; 1999.
- [175] Köpke P, Hess M. Manual for database OPAC, Optical properties of aerosols and clouds. Meteorologisches Institute der Universität München; 1994.
- [176] Fussen D, Bingen C. A volcanism dependent model for the extinction profile of stratospheric aerosols in the UV–visible range. *Geophys Res Lett* 1999;26(6):703–6.
- [177] Segelstein D. The complex refractive index of water. Master's thesis. University of Missouri, Kansas City; 1981.
- [178] Kokhanovsky AA. Cloud optics. Dordrecht: Springer; 2006.
- [179] Macke A, Mueller J, Raschke E. Scattering properties of atmospheric ice crystals. *J Atmos Sci* 1996;53:2813–25.
- [180] Warren SG, Brandt RE. Optical constants of ice from the ultraviolet to the microwave: a revised compilation. *J Geophys Res* 2008;113:1–10. <http://dx.doi.org/10.1029/2007JD009744>.
- [181] Feigelson EM (Ed.). Radiation in cloudy atmosphere. Leningrad: Gidrometeoizdat; 1981 [in Russian].
- [182] Kokhanovsky AA. Local optical properties of mixed clouds: simple parameterizations. *Atmos Res* 2007;84:42–8.
- [183] Key JR, Wang X, Stoeve JC, Fowler C. Estimating the cloudy-sky albedo of sea ice and snow from space. *J Geophys Res* 2001;106(D12):12489–97.
- [184] Matthews E. Global vegetation and land use: new high resolution data bases for climate studies. *J Clim Appl Meteorol* 1983;22:474–87.
- [185] Hautecoeur O, Leroy MM. Surface bidirectional reflectance distribution function observed at global scale by POLDER/ADEOS. *Geophys Res Lett* 1998;25(22):4197–200.
- [186] Pinty B, Roveda F, Verstraete MM, Gobron N, Govaerst Y, Martonchik JV, et al. Surface albedo retrieval from Meteosat 1. Theory. *J Geophys Res* 2000;105(D14):18099–112.
- [187] Cabot F, Dedieu G. Surface albedo from space: coupling bidirectional models and remotely sensed measurements. *J Geophys Res* 1997;102(D16):19645–63.
- [188] Lyapustin AI. Atmospheric and geometrical effects on land surface albedo. *J Geophys Res* 1999;104(D4):4127–43.
- [189] Degünther M, Meerkötter R. Influence of inhomogeneous surface albedo on UV irradiance: effect of a stratus cloud. *J Geophys Res* 2000;105(D18):22755–61.
- [190] Warren SG, Brandt RE, Hinton PO. Effect of surface roughness on bidirectional reflectance of Antarctic snow. *J Geophys Res* 1998;103:25789–807.
- [191] Kokhanovsky AA, Zege EP. Scattering optics of snow. *Appl Opt* 2004;43:1589–602.
- [192] Kokhanovsky AA. Reflection of light from particulate media with irregularly shaped particles. *J Quant Spectrosc Radiat Transfer* 2005;96:1–10.
- [193] Monahan EC, Muirchearthaigh IO. Optimal power-law description of oceanic whitecap coverage dependence on wind speed. *J Phys Oceanogr* 1981;10:2094–9.
- [194] Cox C, Munk W. Statistics of the sea surface derived from sun glitter. *J Mar Res* 1954;13(2):198–227.
- [195] Cox C, Munk W. Measurement of the roughness of the sea surface from photographs of the Sun's glitter. *J Opt Soc Am* 1954;44(11):838–50.
- [196] Nakajima T, Tanaka M. Effect of wind generated waves on the transfer of solar radiation in the atmosphere–ocean system. *J Quant Spectrosc Radiat Transfer* 1983;29:521–37.
- [197] Mishchenko MI, Travis LD. Satellite retrieval of aerosol properties over the ocean using polarization as well as intensity of reflected sunlight. *J Geophys Res* 1997;102:16989–7013.
- [198] Tsang L, Kong JA, Shin RT. Theory of microwave remote sensing. New York, Chichester, Brisbane, Toronto, Singapore: John Wiley and Sons; 1985.
- [199] Breón FM, Henriot N. Spaceborne observations of ocean glint reflectance and modeling of wave slope distributions. *J Geophys Res* 111 2006;C06005:1–10. <http://dx.doi.org/10.1029/2005JC003343>.

- [200] Ebuchi N, Kizu S. Probability distribution of surface wave slope derived using Sun glitter images from geostationary meteorological satellite and surface vector winds from scatterometers. *J Oceanogr* 2002;58:477–86.
- [201] Anikonov AS, Ermolaev SY. On diffuse light reflection from a semiinfinite atmosphere with a highly extended phase function. *Vestn LGU (in Russian)* 1977;7:132–7.
- [202] Kokhanovsky AA, Sokoletsky LG. Reflection of light from semi-infinite absorbing turbid media. Part 2: plane albedo and reflection function. *Color Res Appl* 2006;31:498–509.
- [203] Austin RW. The remote sensing of spectral radiance from below the ocean surface. In: Jerlov NG, Nielsen ES, editors. *Optical aspects of oceanography*. London, New York: Academic Press; 1974. p. 317–44 [Chapter 14].
- [204] Kokhanovsky AA. Spectral reflectance of whitecaps. *J Geophys Res* 2004;109:C05021. <http://dx.doi.org/10.1029/2003JC002177>.
- [205] Moore KD, Voss AKV, Gordon HR. Spectral reflectance of whitecaps: instrumentation, calibration and performance in coastal waters. *J Atmos Oceanic Technol* 1998;15:496–509.
- [206] Pop RM, Fry ES. Absorption spectrum (380–700 nm) of pure water: II. Integrating cavity measurements. *Appl Opt* 1997;36:8710–23.
- [207] Morel A, Maritorena S. Bio-optical properties of oceanic waters: a reappraisal. *J Geophys Res* 2001;106(C4):7163–80.
- [208] Prieur L, Sathyendranath S. An optical classification of coastal and oceanic waters based on the specific absorption curves of phytoplankton pigments, dissolved organic matter, and other particulate materials. *Limnol Oceanogr* 1981;26:671–89.
- [209] Mobley CD. Light and water. Radiative transfer in natural waters. Academic Press Inc.; 1994.
- [210] Morel A. Optical properties of pure water and pure seawater. In: *Optical aspects of oceanography*. New York: Academic Press; 1974. p. 1–24.
- [211] Shifrin KS. Physical optics of ocean water. AIP translation series. American Institute of Physics, New York, 1988.
- [212] Buiteveld H, Hakvoort JHM, Donze M. The optical properties of pure water. In: *SPIE ocean optics*, XII, 1994. p. 174–83.
- [213] Twardowski MS, Claustre H, Freeman SA, Stramski D, Huot Y. Optical backscattering properties of the “clearest” natural waters. *Biogeosciences* 2007;4:1041–58.
- [214] Farinato RS, Roswell RL. New values of the light scattering depolarization and anisotropy of water. *J Chem Phys* 1976;65:593–5.
- [215] Petzold TJ. Volume scattering functions for selected ocean waters. San Diego, CA: Scripps Institute of Oceanography, Institute of Oceanography, Visibility Laboratory; 1972. p. 72–8.
- [216] Haltrin VI. Absorption and scattering of light in natural waters. In: *Light scattering reviews*. Chichester, UK: Springer, Praxis Publishing; 2006. p. 445–86.
- [217] Kopelevich OV. Small-parameter model of optical properties of seawater. In: *Physical ocean optics*, vol. 1. Moscow: Nauka; 1983. p. 208–34 [in Russian].
- [218] Mobley C, Gentili B, Gordon H, Jin Z, Kattawar G, Morel A, et al. Comparison of numerical models for computing underwater light fields. *Appl Opt* 1993;32(36):7484–504.
- [219] Kurucz HL. The solar spectrum: atlases and line identifications. In: Sauval AJ, Blomme R, Grevesse N, editors. *Laboratory and astronomical high resolution spectra*. ASP Conference Series, vol. 81; 1995. p. 17–31.
- [220] Rozanov VV, Rozanov AV. Relationship between different approaches to derive weighting functions related to atmospheric remote sensing problems. *J Quant Spectrosc Radiat Transfer* 2007;105:217–42.
- [221] Platt U. Differential optical absorption spectroscopy (DOAS). In: *Air monitoring by spectroscopic techniques*. New York: John Wiley; 1994.
- [222] Platt U, Stutz J. Differential optical absorption spectroscopy. Principles and applications. Berlin, Heidelberg: Springer-Verlag; 2008.
- [223] Rozanov VV, Rozanov AV. Differential optical absorption spectroscopy DOAS and air mass factor concept for a multiply scattering vertically inhomogeneous medium: theoretical consideration. *Atmos Meas Tech* 2010;3:751–80. <http://dx.doi.org/10.5194/amt-3-751-2010>.
- [224] Deuzé JL, Herman M, Santer R. Fourier series expansion of the transfer equation in the atmosphere–ocean system. *J Quant Spectrosc Radiat Transfer* 1989;41:483–94.
- [225] Herman BM, Ben-David A, Thome KJ. Numerical techniques for solving the radiative transfer equation for a spherical shell atmosphere. *Appl Opt* 1994;33:1760–70.
- [226] Loughman RP, Griffioen E, Oikarinen L, Postlyakov OV, Rozanov A, Flittner DE, et al. Comparison of radiative transfer models for limb-viewing scattered sunlight measurements. *J Geophys Res* 2004;109 (D06303):1–16. <http://dx.doi.org/10.1029/2003JD003854>.
- [227] Blum M, Rozanov VV, Burrows JP, Bracher A. Coupled ocean–atmosphere radiative transfer model in framework of software package SCIATRAN: selected comparisons to model and satellite data. *Adv Space Res* 2012;49(12):1728–42.
- [228] Mobley CD, Sundman LK. *Hydrolight 5.0 users’ guide*. Technical Report. Bellevue, WA: Sequoia Scientific, Inc.; 2008.
- [229] You Y, Zhai P-W, Kattawar GW, Yang P. Polarized radiance fields under a dynamic ocean surface: a three-dimensional radiative transfer solution. *Appl Opt* 2009;48(16):3019–29.
- [230] Zege EP, Chaikovskaya LI. New approach to the polarized radiative transfer problem. *J Quant Spectrosc Radiat Transfer* 1996;55:19–31.
- [231] Coulson K, Dave J, Sekera Z. Tables related to radiation emerging from a planetary atmosphere with Rayleigh scattering. Berkeley, Los Angeles: University of California Press; 1960.
- [232] Natraj V, Li K-F, Yung YL. Rayleigh scattering in planetary atmospheres: corrected tables through accurate computation of x and y functions. *Astrophys J* 2009;691:1909–20.
- [233] Coulson K. Polarization and intensity of light in the atmosphere. A. Deepak Publishing; 1988.
- [234] Garcia RDM, Siewert CE. The FN method for radiative transfer models that include polarization effects. *J Quant Spectrosc Radiat Transfer* 1989;41:117–45.
- [235] Vestrucci P, Siewert CE. A numerical evaluation of an analytical representation of the components in a Fourier decomposition of the phase matrix for the scattering of polarized light. *J Quant Spectrosc Radiat Transfer* 1984;31:177–83.
- [236] Duan M, Min Q, Lu D. A polarized radiative transfer model based on successive order of scattering. *Adv Atmos Sci* 2010;27: 891–900. <http://dx.doi.org/10.1007/s00376-009-9049-8>.
- [237] Astakhov IE, Budak VP, Lisitsin DV, Selivanov VA. Solution of the vector radiative transfer equation in the small angle approximation of the spherical harmonics method. *Atmos Oceanic Opt* 1994;7:398–403.
- [238] Budak VP, Korin SV. On the solution of a vectorial radiative transfer equation in an arbitrary three-dimensional turbid medium with anisotropic scattering. *J Quant Spectrosc Radiat Transfer* 2008;109:220–34.
- [239] Kokhanovsky AA, Budak VP, Cornet C, Duan M, Emde C, Katsev IL, et al. Benchmark results in vector atmospheric radiative transfer. *J Quant Spectrosc Radiat Transfer* 2010;111:1931–46.
- [240] Mishchenko MI. The fast invariant imbedding method for polarized light: computational aspects and numerical results for Rayleigh scattering. *J Quant Spectrosc Radiat Transfer* 1990;43:163–71.
- [241] Bézy J-L, Delwart S, Rast M. MERIS—a new generation of ocean-colour sensor onboard Envisat. *ESA Bull* (103);2000:48–56.
- [242] Llewellyn-Jones D, Edwards MC, Mutlow CT, Birks AR, Barton JJ, Tait H. AATSR: global-change and surface-temperature measurements from Envisat. *ESA Bull* (105);2001:10–21.
- [243] Buchwitz M, Rozanov VV, Burrows JP. A near-infrared optimized DOAS method for the fast global retrieval of atmospheric CH₄, CO, CO₂, H₂O, and N₂O total column amounts from SCIAMACHY ENVISAT-1 nadir radiances. *J Geophys Res* 2000;105:15231–45.
- [244] Reuter M, Bovensmann H, Buchwitz M, Burrows JP, Connor BJ, Deutscher NM, et al. Retrieval of atmospheric CO₂ with enhanced accuracy and precision from SCIAMACHY: validation with FTS measurements and comparison with model results. *J Geophys Res* A 2011;116(D04301):1–13. <http://dx.doi.org/10.1029/2010JD015047>.
- [245] Reuter M, Buchwitz M, Schneising O, Heymann J, Bovensmann H, Burrows JP. A method for improved SCIAMACHY CO₂ retrieval in the presence of optically thin clouds. *Atmos Meas Tech* 2010;3: 209–32.
- [246] Kokhanovsky AA, Aoki T, Hachikubo A, Hori M, Zege EP. Reflective properties of natural snow: approximate asymptotic theory versus in situ measurements. *IEEE Trans Geosci Remote Sensing* 2005;43 (7):1529–35.
- [247] Kokhanovsky A, Rozanov VV, Aoki T, Odermatt D, Brockmann C, Krüger O, et al. Sizing snow grains using backscattered solar light. *Int J Remote Sensing* 2011;32:6975–7008.
- [248] Bauer R, Rozanov A, McLinden CA, Gordley LL, Lotz W, R. III JM, et al. Validation of SCIAMACHY limb NO₂ profiles using solar occultation measurements. *Atmos Meas Tech* 2012;3(5):1059–84.
- [249] Ernst F, von Savigny C, Rozanov A, Rozanov V, Eichmann K-U, Brinkhoff LA, et al. Global stratospheric aerosol extinction profile retrievals from SCIAMACHY limb-scatter observations. *Atmos Meas Tech Discuss* 2012;5:5993–6035.
- [250] Mieruch S, Weber M, von Savigny C, Rozanov A, Bovensmann H, Burrows JP, et al. Global and long-term comparison of SCIAMACHY

- limb ozone profiles with correlative satellite data (2002–2008). *Atmos Meas Tech* 2012;5:771–88.
- [251] Rozanov A, Bovensmann H, Bracher A, Hrechanyy S, Rozanov V, Sinnhuber M, et al. NO₂ and BrO vertical profile retrieval from SCIAMACHY limb measurements: sensitivity studies. *Adv Space Res* 2005;36(5):846–54. <http://dx.doi.org/10.1016/j.asr.2005.03.013>.
- [252] Rozanov A, Eichmann K-U, von Savigny C, Bovensmann H, Burrows JP, von Bagen A, et al. Comparison of the inversion algorithms applied to the ozone vertical profile retrieval from SCIAMACHY limb measurements. *Atmos Chem Phys* 2007;7:4763–79.
- [253] Rozanov A, Kühl S, Doicu A, McLinden C, Pukite J, Bovensmann H, et al. BrO vertical distributions from SCIAMACHY limb measurements: comparison of algorithms and retrieval results. *Atmos Meas Tech Discuss* 2010;3:5079–178. <http://dx.doi.org/10.5194/amtd-3-5079-2010>.
- [254] Rozanov A, Weigel K, Bovensmann H, Dhomse S, Eichmann K-U, Kivi R, et al. Retrieval of water vapor vertical distributions in the upper troposphere and the lower stratosphere from SCIAMACHY limb measurements. *Atmos Meas Tech Discuss* 2010;3:4009–57. <http://dx.doi.org/10.5194/amtd-3-4009-2010>.
- [255] Tyler JE. Radiance distribution as a function of depth in an under-water environment. *Bulletin of the Scripps Institution of Oceanography of the University of California*, vol. 7(5), 1960. p. 363–412.
- [256] Duntley SQ. Light in the sea. *J Opt Soc Am* 1963;53(2):214–33.
- [257] Helliwell WS. Finite-difference solution to the radiative-transfer equation for in-water radiance. *J Opt Soc Am A* 1985;2(8):1325–30.
- [258] Mobley CD. A numerical model for the computation of radiance distributions in natural waters with wind-roughened surfaces. *Limnol Oceanogr* 1989;34(8):1473–83.
- [259] Barichello LB, Garcia RDM, Siewert CE. Particular solutions for the discrete-ordinates method. *J Quant Spectrosc Radiat Transfer* 2000;64:219–26.
- [260] Qin Y, Box MA, Jupp DLB. Particular solution of the discrete-ordinate method. *Appl Opt* 2004;43:3717–25.